JAERI 1304

JAERI 1304

Studies on Surface Chemical States of Some Metals and Ceramics Bombarded with Energetic Light-ions

February 1987

日 本 原 子 力 研 究 所

Japan Atomic Energy Research Institute

JAERIレポートは，日本原子力研究所が研究成果編集委員会の審査を経て不定期に公刊している研究報告書です。

入手の問合わせは，日本原子力研究所技術情報部情報資料課（〒319-11茨城県那珂郡東海村）あて，お申しこしください。なお，このほかに財団法人原子力弘済会資料センター（〒319-11 茨城県那珂郡東海村日本原子力研究所内）で複写による実費頒布をおこなっております。

JAERI reports are reviewed by the Board of Editors and issued irregularly.

Inquiries about availability of the reports should be addressed to Information Division Department of Technical Information, Japan Atomic Energy Research Institute, Tokai-mura, Naka-gun, Ibaraki-ken 319-11, Japan.

編集兼発行　日本原子力研究所
印　　刷　いばらき印刷㈱

Studies on Surface Chemical States of Some Metals and Ceramics Bombarded with Energetic Light-ions

Yuji BABA

Department of Chemistry
Tokai Research Establishment
Japan Atomic Energy Research Institute
Tokai-mura, Naka-gun, Ibaraki-ken

(Received August 11, 1986)

Abstract

An electron spectroscopy was applied to the investigation of surface chemical state of some metals and ceramics bombarded with energetic light ions. Bombardments of keV-order hydrogen ions on scandium, titanium, vanadium, yttrium, zirconium and niobium induced the XPS core-line chemical shifts to higher binding-energies by 0.2-1.4 eV. In the valence-band (VB) regions, the bombardments also brought about the appearence of new photopeaks at 3.0-5.0 eV below the Fermi level. Although the peak energies are lower by 1-3 eV than those calculated for MeH_2 (Me=metal) by molecular-orbital theory, the peaks are assigned to the metal-H bonds. The chemical shifts induced by bombarding hydrogen-ions were also observed in the X-ray-induced Auger electron spectra (XAES) for yttrium, zirconium and niobium. The hydride layers produced by the ion-implantation are more stable at high temperature than those obtained by thermal synthesis. The phenomena were interpreted by the surface damages which prevent thermal diffusion of hydrogen.

In the case of hydrogen-ion bombarded SiC, carbon enriched layer was observed in the near surface region, while the surfaces of Si_3N_4 and SiO_2 became silicon-rich after the bombardments. On the other hand, the bombardments of H_2^+, D_2^+ and He^+-ions on TiC, TiN and TiO_2 made their surfaces titanium-rich. At high fluences, the X/Ti (X=C, N, O) become constant. The energy dependences of the steady state values of the C/Ti ratios have maximum at 2-4 keV/atom of incident ion, while those of the N/Ti and O/Ti ratios decreased with the increase in the ion energies. Incident-energy dependences of the Ti^+/X^+ ratios determined by SIMS substantiate that the sputtering is responsible for the surface compositional change of the binary compounds. The appreciable changes in the surface chemical state of TiC and TiN could not be observed after the bombardments, whereas the surface of TiO_2 was easily reduced to Ti_2O_3 by the H_2^+ and D_2^+, or to TiO by the He^+ and Ar^+-ion bombardments, respectively. The difference in the reduced species is correlated with the thermodynamical parameters of the corresponding reduction reactions.

Keywords: Surface Chemical State, Transition metal, Ceramics, Light-ion Bombardment, X-ray Photoelectron Spectroscopy, Auger Electron Spectroscopy, Secondary Ion Mass Spectrometry, First Wall Material, Plasma-wall Interaction, SiC, Si_3N_4, SiO_2, TiC, TiN, TiO_2

軽イオン衝撃した金属およびセラミックスの表面化学状態に関する研究

日本原子力研究所東海研究所化学部

馬 場 祐 治

（1986年8月11日受理）

要　　旨

軽イオン衝撃した金属及びセラミックの表面化学状態を，電子分光法により解析した．金属スカンジウム，チタン，バナジウム，イットリウム，ジルコニウム及びニオブにkeVオーダーの水素イオンを照射すると，XPSスペクトルの内殻ピークは0.2−1.4eV高エネルギー側に化学シフトする．また，価電子帯領域には，フェルミレベルより3.0−5.0eV深い位置に新たなピークが出現する．このピーク位置は，分子軌道理論による計算値に比べ1−3eV低いが，金属−水素結合による電子ピークと考えられる．水素イオン衝撃に伴う化学シフトは，金属イットリウム，ジルコニウム及びニオブのX線励起オージェ電子スペクトルでも観測された．一方，金属中にイオン注入された水素は，熱化学的に吸蔵された水素に比べ加熱放出温度が高い．この理由は，イオン衝撃による損傷表面層が水素の熱拡散を阻止するためである．

水素イオン衝撃したSiCターゲットでは，表面に炭素過剰層が形成されるが，Si_3N_4及びSiO_2ターゲットでは，水素イオン衝撃に伴ないケイ素過剰層が形成される．また，TiC，TiN及びTiO_2ターゲットにH_2^+，D_2^+及びHe^+イオン衝撃を行うと，チタン過剰層が形成される．表面のX/Ti比(X=C，N，O)が一定となる重照射下において，TiC表面のC/Ti比は，入射イオンエネルギーが2−4keV/atomの時最大となる．一方，TiN及びTiO_2表面のX/Ti比は，入射イオンエネルギーの増加に伴い，単調に減少する．SIMSスペクトルにおけるTi^+/X^+比の入射イオンエネルギー依存性から，これら二成分系化合物の表面組成変化は，構成成分元素のスパッタリングによることがわかった．また，TiC及びTiNの表面化学状態は，イオン衝撃によっても変化しないが，TiO_2表面は，H_2^+，D_2^+イオン衝撃でTi_2O_3に，He^+，Ar^+イオン衝撃でTiOに還元される．衝撃イオンによる生成化学種の差異は，還元反応の熱力学的パラメーターと密接に関連することを明らかにした．

CONTENTS

目　　次

List of Tables and Figures

List of Tables

List of Figures

1. Introduction

1.1 Chemical effect of energetic particle on solid surface

Bombardment of energetic ions or neutral particles on solid surface gives rise to various changes in mechanical, physical and chemical properties of the target material. Energetic particle with relatively high energy ($>$ keV) implanted in solid loses its kinetic energy in elastic collision leading to electronic excitation of target atoms or molecules. While low-energy particle ($<$ keV) interacts with solid predominantly by elastic nuclear collision cascade resulting in the formation of large amount of ion-induced alterations such as vacancy and interstitial atoms.

The preliminary physical process of such ion-induced alteration of target material has recently been intensively investigated in relation to the radiation damage studies. At high fluence, on the other hand, these preliminary processes being accumulated inevitably induce the changes in the chemical bond-structure of the target as well as changes in the mechanical and physical properties. If the incident ion is chemically reactive such as hydrogen ion, there may also develope the formation of the chemical bond between implanted ions and the target. Thus the chemical state of the ion-implanted layer may become different from that of the bulk. Such changes in the chemical state of the ion-bombarded solid, that is, chemical effect of energetic particles on solid surface have recently attracted much attention in both scientific and technological aspects from the following viewpoints.

First, ion-induced chemical reaction is highly specific because the reaction takes place through non-equilibrium process in contrast to thermal reaction, considering that the activation energy of the reaction is supplied by the kinetic energy of the implanted ion itself. Thus, highly non-equilibrium state is produced in the course of the trajectory of the incident ions. In this aspect, the process of the ion-induced chemical reaction is rather similar to that of hot-chemical reaction induced by a recoil atom of nuclear transformation. Hence the experimental technique using ion-implantation has been applied as substitutional method to the investigation of hot-chemical reaction by recoil-implanted atom[1-5]. Compared with the hot-chemical method using recoil atom by nuclear decay, the ion-implantation method is more comprehensive because the species and energies of the incident ions can be arbitrarily selected.

Secondly, the chemical state of the ion-implanted solid surface has become significant in technological aspect. Using an ion-induced chemical reaction, we can obtain, at room temperature, unexpected compounds which cannot be synthesized by thermal process even at high temperature. In addition, the reaction can be arbitrarily induced in the specified area of the target material using controlled ion-beams. In practice, ion-implantation doping in semiconductor materials is now widely used for the production of various electronic devices[6-10].

Thirdly, the chemical effects of energetic particles on solid surfaces have become important in the field of vacuum technology and plasma science. Especially in fusion research, the chemical state of the ion-bombarded refractory materials are one of current problems to be solved in relation to the investigation of plasma-wall interaction. A plasma first-wall of fusion reactor is expected to be exposed to various kinds of energetic particles such as deuterium, tritium, helium, oxygen and so on at high fluence, and heavy particles produced

by the light-ion bombardment prevent the plasma ignition[11,12]. In this aspect, low-Z (Z: atomic number) refractory materials of low sputtering yield such as graphite, silicon carbide and titanium carbide are proposed as candidates of plasma first wall. As the particle emission from such first-wall materials strongly depends on the surface chemical state, the chemical effect of the ion-bombardment on the material surface must be elucidated in view of lowering of plasma impurity.

In these scientific and technological aspects, the accumulation of the information on the chemical state of ion-bombarded solid surface is required. For this purpose, the development in the analytical method for the ion-bombarded surface is also indispensable.

1.2 Overview of chemical state studies of ion-bombarded solid

In early stage, the chemical effect of ion bombardment on solid has been investigated in the field of radiation chemistry using isotope separators. First experiment about chemical state studies for the ion-bombarded solid has been carried out by Croatto et al. in 1954[13]. In this work, they have elucidated the chemical effect of energetic $^{14}C^{+}$-ion bombardment on organic compounds in order to compare with that induced by a recoil atom produced by the $^{14}N(n,p)^{14}C$ reaction. Since then, extensive work about the chemical state analysis of ion-bombarded organic and inorganic compounds has been carried out mainly with the intention of comparison with hot-chemical reaction induced by nuclear transformation[14–22]. Andersen et al.[16] have investigated the chemical state of ion-implanted $^{32}P^{+}$ in NaCl single crystal. In order to determine the valence state of the ion-implanted phosphorus, they have adopted a chemical method after dissolving the ion-bombarded sample from surface to bulk. Ascoli et al.[18] have bombarded solid organic target with tritium ions and compared the chemical effect of ion-bombardment with that of recoil tritons from $^{6}Li(n,\alpha)^{3}H$ process. They have also elucidated that molecular ions such as T_2^{+} and T_3^{+} dissociate into the constituent atoms in their initial collisions with the target molecules and the dissociated species have the same chemical effect as that of T^{+} ion with corresponding energy. Kasrai et al.[21] have bombarded NaCl with $^{35}S^{+}$ ions, and revealed that there exist several products by ion-induced chemical reaction.

Throughout these works in early stage, chemical state of ion-bombarded some compounds has been sufficiently elucidated, and it has been revealed that no significant difference exists between the chemical reactivity of a recoil atom produced by nuclear transformation and the electrically accelerated ions with corresponding energy. However, the uncertainty still remained whether the chemical state of ion-bombarded surface is the same as the analyzed chemical species or not, because the products of the ion-induced reaction were analyzed by a chemical method after dissolving the irradiated samples. The lack of non-destructive analytical method to determine the chemical state of the ion-bombarded solid surfaces in those days therefore limited the application of the ion-implantation method to simulate the chemical effect of energetic particles on solid surface.

1.3 Non-destructive methods for analysis of ion-bombarded solid

In order to dissolve the disadvantage mentioned above, several non-destructive analytical methods have recently been applied to the investigation of surface damages produced by the ion-bombardment. An Auger electron spectroscopy (AES)[23–26], secondary ion mass spectrometry (SIMS)[27,28] and Ratherford backscattering spectroscopy (RBS)[29–31] have revealed the surface chemical composition and its depth profiles for the ion-bombarded

solid. The molecular structure of the ion-bombarded surface has also been elucidated by infrared spectra (IR)[32-34] and Raman spectroscopy[24,35,36] and microscopic structure by scanning electron microscopy (SEM)[37-41].

Among these non-destructive analytical methods, an electron spin resonance (ESR) is considered to be the most effective to analyze the chemical species in the ion-bombarded layers[42-45] because the radical species often produced in the damage layer can be easily detected by this method. However, as long as the analysis of molecular species which are predominantly produced at high fluence, an X-ray photoelectron spectroscopy (XPS) as well as ultraviolet photoelectron spectroscopy (UPS) seems to be more effective.

1.4 Application of XPS to chemical state analysis of ion-bombarded solid surface

An XPS, developed mainly by Siegbahn and his co-workers in 1960th[46,47], is based on photoelectric effect of solid. This gives information on the bonding charactor of the solid surface at about 2 nm. The process of the photoelectric effect and the principle of XPS are shown in **Fig. 1.1**. The main advantages for applying XPS to the chemical state studies of ion-bombarded surface are summarized as follows: (1) The method is highly non-destructive because soft X-rays such as Mg Kα (1253.6 eV) or Al Kα (1486.6 eV) are used as primary excitation sources. Thus the surface chemical state hardly changes during the spectral measurement. (2) The XPS measurement is carried out under a high vacuum so that the sample surface is scarcely affected by the contamination of oxygen, carbon and so on. This advantage is strengthened if the ion bombardment is carried out in the same chamber as the XPS measurement. (3) The method is highly comprehensive, since the chemical states of all elements except for hydrogen and helium can be directly detected.

Taking the above advantages, XPS has already been applied to the chemical state studies of solid surfaces irradiated with various kinds of radiations. Rabalais et al.[48] have reported the decomposition of UV-irradiated MoO_3 by XPS, and found a radiation-induced new

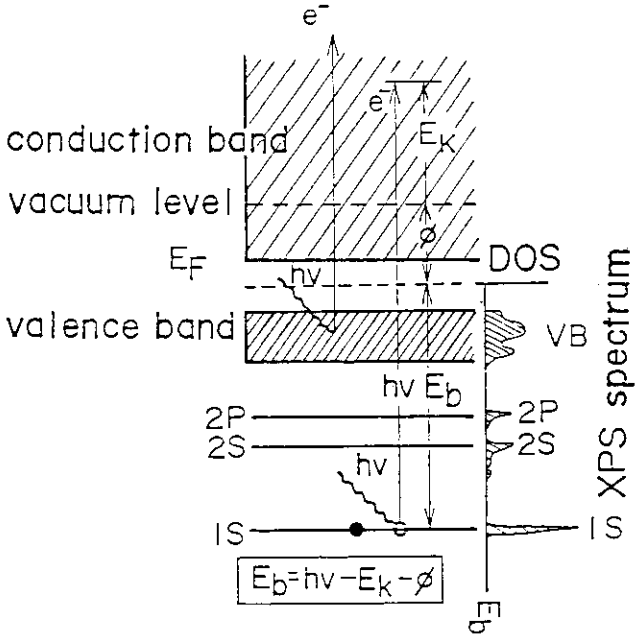

Fig. 1.1 Emission process of photoelectrons and principle of XPS.

photopeak just below the Fermi level. Angelis[49] has observed a reduction of CrO_3 to Cr(III) by X-ray irradiation. Regarding the bombardment by electron beams, Sasaki et al.[50] have irradiated some inorganic compounds such as alkali-metal halates and perhalates. Measuring the surface chemical state by XPS, they have elucidated the mechanism of the radiation decomposition process.

In contrast to these experiments, only a few works have been made for the ion-bombarded solid surfaces. Most of these works concerning the surface chemical state of ion-bombarded solids have been carried out mainly for the investigation of sputtering of surface oxygen from metal oxides by rare-earth ion bombardments. These works were intended to reply the practical requirements to obtain pure metallic surface. Kim et al.[51,52] have measured the XPS spectra of various metal oxides bombarded with 0.4-1.0 keV of rare-earth ions, and discussed the reduction mechanism by the ion-bombardments. Since that time, some investigators have reported the surface chemical changes by rare-earth ion bombardments for some inorganic compounds using XPS[53-60].

In cases of chemically reactive ions, on the other hand, the contribution of the chemical effect of the incident ions must be taken into account. However, there exist few available data about the changes in the surface chemical state induced by such reactive ions. Especially the effect of the bombardment of hydrogen and its isotope ions on the surface chemical state, which is now of importance in relation to the plasma-wall interaction as descrived above, has scarcely been investigated. The present report deals with the surface chemical state of some metals and ceramics bombarded with hydrogen and related light ions with energy of keV order. A mechanism of surface chemical changes will be discussed in relation to the sputtering phenomenon.

1.5 General description of the following chapters

In the present report, hydrogen-ions and the related light ions with energies of keV order are bombarded on some metals and ceramics which are considered to be candidate materials as first-wall of fusion device. After the bombardments, the changes in the surface chemical state are analyzed by an electron spectroscopic method in the same chamber as the ion-bombardments.

In chapter 2, information on the chemical states obtained from the core-line XPS spectra are described for the bombarded surfaces of several transition metals such as scandium, titanium, vanadium, chromium, nickel, yttrium, zirconium, niobium and molybdenum. The chemical shifts accompanied by the ion-bombardments are compared with those of the corresponding hydrides synthesized by thermal reaction.

Chapter 3 deals with the XPS spectra in valence-band regions for the same metals as those in chapter 2 together with those of the thermally synthesized hydrides. The level structures near the Fermi level are discussed in connection with the calculated results for the stoichiometric hydrides using molecular-orbital theory.

In chapter 4, thermal release of the hydrogen implanted in the metals is investigated. The behaviors of the thermal release are compared with those of the thermally synthesized hydrides, which are measured by a thermogravimetrical (TG) analysis.

A promising analytical method for the chemical state of hydrogen implanted in metals is proposed in chapter 5. This is based on X-ray-induced Auger electron emission whose signal appears together with the usual XPS spectra. The magnitudes of the Auger-line shifts for the metal-H bonds are discussed in connection with the polarizabilities of the metal-H bonds.

The following two chapters deal with the surface chemical changes for low-Z (Z : atomic number) binary compounds which are candidate materials of the first-wall of fusion reactor. In chapter 6, the surface chemical changes induced by hydrogen-ion bombardments are presented for silicon-containing materials such as SiC, Si_3N_4 and SiO_2. The changes are investigated for both the bond-structures and surface compositions. An Auger electron spectroscopy is also employed to elucidate the surface compositional changes.

In chapter 7, the surface compositional and chemical-state changes by light-ion bombardments are presented for titanium-containing materials such as TiC, TiN and TiO_2, one of which is now tentatively used as the first-wall material of a fusion research reactor. In order to elucidate the mechanism of the surface compositional changes, secondary ions emitted from the target surfaces are analyzed by the use of a quadrupole mass-analyzer. The compositional changes are discussed in relation to the sputtering of the constituent elements.

The results of the present work are summarized in chapter 8.

2. Core-line XPS spectra of transition metals bombarded with energetic hydrogen ions

2.1 Introduction

A number of transition metals belonging to groups IIIA (Sc,Y), IVA (Ti,Zr) and VA (V,Nb) easily absorb hydrogen through exothermic reaction to form stable mono-, di-, or trihydrides[61-65]. Due to the chemical properties, considerable amount of hydrogen is trapped, when these metals are exposed to hydrogen beams[66-68]. The other transition metals, on the other hand, hardly react with hydrogen, and absorption of hydrogen in these metals can take place through endothermic reaction without forming stable hydride phases at ambient temperature[62]. Even in these metals, however, hydrogen atoms are compulsorily implanted by means of an ion-implantation. Thus the electronic structure of the hydrogen-implanted layer in these metals is of interest, since such products cannot be obtained by thermal reaction.

The interaction between energetic hydrogen-ions and transition-metals has also technologically become of importance in the field of fusion research, since some transition metals are considered to be candidate of first-wall materials. The formation of hydrides at the surface of a first-wall material causes the brittleness resulting in the increase in the plasma impurity[69-72].

In these aspects, extensive data concerning hydrogen-ion implantation in transition metals have recently been accumulated. These are the depth profilings of trapped hydrogen[73-75], crystal structure of implanted layer[76,77], electron microscopic observations of ion-bombarded surfaces[40,78], and so on. With respect to the chemical state of the implanted hydrogen, however, few experiments have been so far carried out, because the experimental methods for the state analysis of hydrogen in metal have not been established yet.

Regarding the chemical state of hydrogen in a stoichiometric hydrides, the metal-H bonds have been theoretically investigated based on band-theory or molecular-orbital (MO) calculations, and it has been revealed that hydrogen atoms are negatively charged in metal hydride[79-81].

Experimentally, it is presumed that the charge transfer from metal to hydrogen induces increase in the core-line energy of the metal. In fact, the core-line XPS spectra for thermally synthesized hydrides have showed the energy shifts of photopeaks to higher energy side from their metallic states[82-85]. However the trapping state of ion-implanted hydrogen in these metals still remains unclear.

In this chapter, the chemical states of some 3d and 4d transition metals bombarded with energetic hydrogens are investigated for the first time by measuring the XPS spectra in core-line region. The chemical shifts induced by the hydrogen-ion bombardments are also compared with those of the thermally synthesized hydrides.

2.2 Experimental

2.2.1 Materials

All metals used were high purity foils (99.9%) from Furuuchi Chemicals Co. Ltd. The surfaces of the foils were polished with an emery paper before introduction into a spectrometer chamber, and they were mechanically scraped with a steel file at a pressure of

1.5×10^{-8} Pa before the XPS measurements in order to remove surface oxides.

The hydrides of scandium, titanium, vanadium and yttrium as reference materials were thermally synthesized by a following procedure. Metallic foils in a molybdenum boat were degassed at respective temperatures shown in **Table 2.1** for 3 hours in an electric furnace at a pressure of 1.5×10^{-4} Pa. Then, purified hydrogen gas was introduced into the furnace up to 1.8 atm. After keeping at the temperature for 30 min, the furnace was cooled to room temperature at a rate of 50 °C/hr. In the case of scandium hydride, introduction of hydrogen more than H/Sc=0.7 provided a pulverized hydride which was unmeasurable in the spectrometer due to the oxide overlayer. Thus the scandium hydride obtained was a non-stoichiometric one.

Table 2.1 Conditions of thermal synthesis and compositions for the metal hydrides used as references. Detailed procedures of the thermal synthesis are described in section 2.2.1

Metal	Temperature (°C)	Pressure of H_2	Composition *
Sc	200	1.5	$ScH_{0.68}$
Ti	700	1.5	$TiH_{1.98}$
V	500	1.5	$VH_{0.55}$
Y	150	1.8	$YH_{2.98}$
Zr	570	1.2	$ZrH_{1.64}$
Nb	570	1.2	$NbH_{0.86}$

* : Chemical compositions of hydrides were determined by a gravimetrical analysis.

The procedures of the thermal synthesis of zirconium and niobium hydrides are essentially the same as those described by Veal et al.[86] and Wainwright et al.[87]. Briefly, metallic foils in a molybdenum boat were degassed at 650°C for 15 hours in an electric furnace at a pressure of 1.5×10^{-4} Pa. Keeping the furnace at 570°C, purified hydrogen gas was introduced to a pressure of 1.2 atm. Then, the furnace was cooled over a period of 30 min to 350°C and evacuated to a pressure of 10^{-4} Pa. Subsequently, the furnace was again heated to 570°C. By repeating this procedure three times, the metallic foils were extremely activated for the hydrogenation. The chemical compositions of the hydrides determined by a gravimetrical analysis are summarized in **Table 2.1**.

Before introduction into the spectrometer chamber, the surfaces of the thermally synthesized hydrides were polished with emery papers in dry nitrogen atmosphere. Prior to the XPS measurements, the surfaces of the hydrides were scraped with a tungsten brush in the preparation chamber at a pressure of 1.5×10^{-8} Pa.

Reference oxides such as Sc_2O_3, TiO_2, V_2O_5, Cr_2O_3, NiO and Y_2O_3 were prepared by oxidizing the metallic foils at 300-500°C for 3 hours in oxygen atmosphere. Zirconium and niobium oxides were synthesized by oxidizing zirconium hydroxide and niobium foil, respectively, at 1000°C. Niobium dioxide, which was also used as reference material, was obtained by reducing Nb_2O_5 with hydrogen at 1000°C.

2.2.2 Ion-implantation method

Before the ion implantation, the metallic foils were annealed at 450°C at a pressure of 3×10^{-7} Pa. In order to remove surface oxides, they were then mechanically scraped with a steel file in the preparation chamber at a pressure of 1.5×10^{-8} Pa.

The ion implantation was performed in the same chamber as the XPS analysis. The schematic diagram of the experimental apparatus is displayed in **Fig. 2.1**. The ion gun used for both ion implantation and Ar^+-ion etching was a Penning-ion-gauge type into which hydrogen or argon gas continuously flowed. The metallic foils were vertically exposed to 8-keV hydrogen molecular-ions at a pressure of 5×10^{-4} Pa. At this energy, more than 90% of total ions was composed of H_2^+, which was confirmed by the magnetical separation of the ion beam. Hydrogen gas supplied into the ion-source was purified by an apparatus shown in **Fig. 2.2**. After all lines were evacuated, hydrogen gas was introduced through an Ag-Pd membrane of 30 μm thickness. **Figs. 2.3** and **2.4** show an effect of the gas purification on

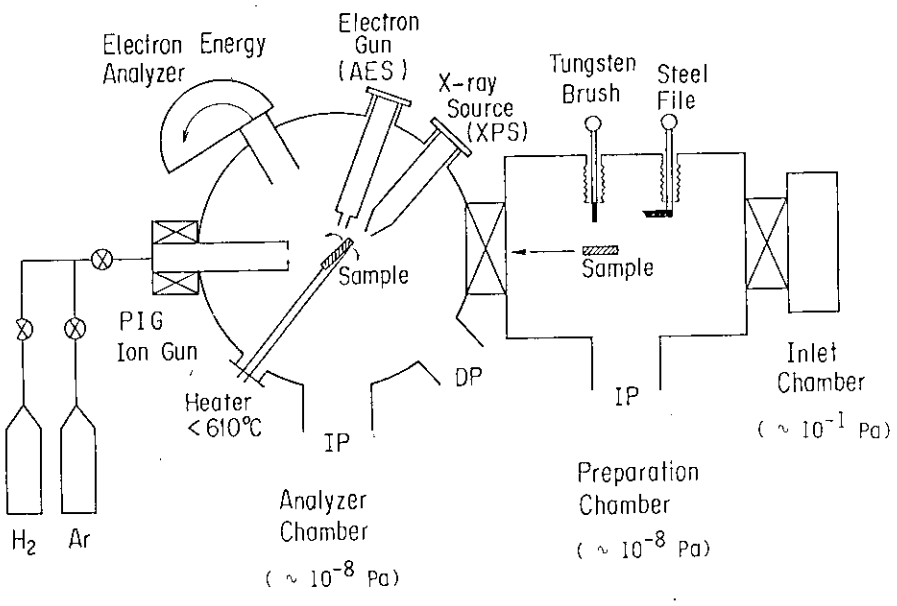

Fig. 2.1 Schematic diagram of the experimental apparatus. Bombardments of ions are carried out in the same chamber as the XPS and AES measurements.

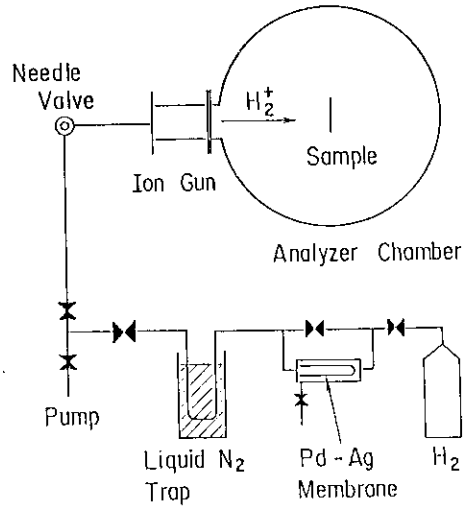

Fig. 2.2 Schematic diagram of gas purification system for hydrogen-ion implantation.

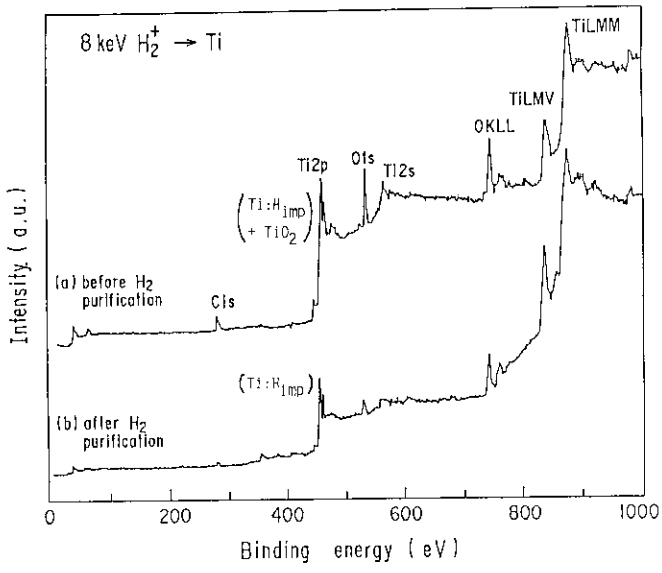

Fig. 2.3 XPS wide scans of hydrogen-ion bombarded titanium before (a) and after (b) the hydrogen-gas purification.

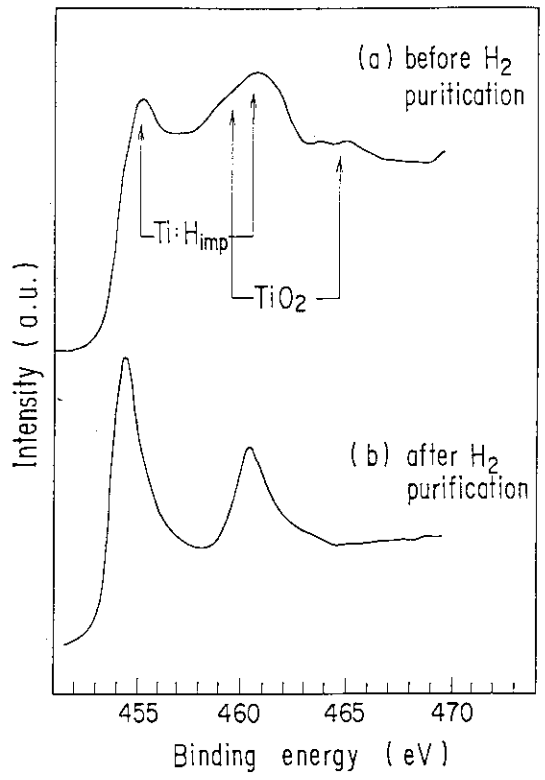

Fig. 2.4 Ti2p XPS spectra of hydrogen-ion bombarded titanium before (a) and after (b) the hydrogen-gas purification.

the XPS wide scan and the Ti2p spectrum, respectively. In these figures, H_{imp} indicates the implanted hydrogen. After the purification, the intensities of the O1s line and O(KLL) Auger peak in the wide scan were reduced as seen in **Fig. 2.3**, and the Ti2p line of the oxide also disappeared as seen in **Fig. 2.4**.

The current density monitored by the use of a small Faraday cup was 80-150 $\mu A/cm^2$, i.e., $(5\text{-}9)\times10^{14}$ ions/cm^{2}sec, and the total fluence was up to 1×10^{18} ions/cm^2.

2.2.3 XPS measurements

XPS measurements were carried out with an ESCALAB-5 spectrometer (V.G. Scientific Co. Ltd.) employing Mg Kα X-rays (1253.6 eV). The base pressure of the analyzer chamber was less than 1.5×10^{-8} Pa.

Energies were calibrated using the $4f_{7/2}$ line of metallic gold, assumed to have a binding energy of 84.0 eV. The reproducibility of the measured energies was within ±0.1 eV. Deconvolution of the core-line spectra was essential in the chemical state analysis of the samples covered with the oxide overlayer. This was done by means of a Gaussian curve-fitting program.

2.3 Results and discussion

2.3.1 General remarks

General method to obtain a pure metallic surface is an Ar^+-ion sputtering. However, it is reported that there exist some metals which cannot be reduced from oxide to pure metallic phase by this method[51,52,88]. Another problem in the Ar^+-ion sputtering is the radiation damage produced on the metallic surface.

Fig. 2.5 shows the Nb3d XPS spectra of pure niobium surfaces obtained by two different

methods, i.e., mechanical scraping by a steel file and Ar^+-ion sputtering. Apparently, the binding energies of the $Nb3d_{5/2}$ lines are different in these two spectra. To investigate this phenomenon, the Ar^+-ion bombardments were also carried out on the mechanically scraped surface at various fluences. **Fig. 2.6** shows the energy shifts of the $Nb3d_{5/2}$ line for the Ar^+-ion bombarded niobium metal as a function of the ion fluence. The separation energy is almost proportional to the ion fluence up to 4×10^{17} ions/cm^2, whereas it saturates at the fluence over 6×10^{17} ions/cm^2.

One of the plausible reasons of the energy shifts is the radiation damage induced by the Ar^+-ion bombardment. In fact, it has been observed that the bombardment of heavy ions causes the surface roughness such as cone formation[38,41,89,90]. Although a quantitative explanation of the ion-induced damages has not been given, an importance of the nucleation

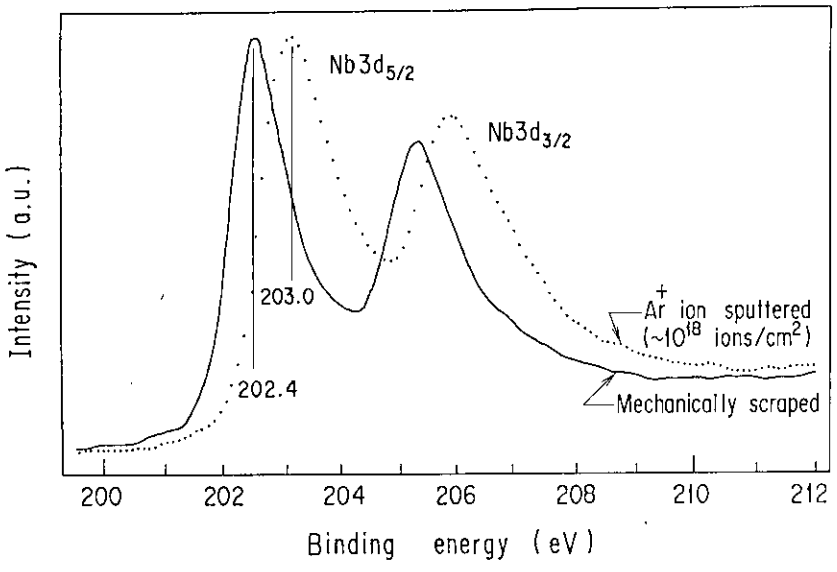

Fig. 2.5 Nb3d XPS spectra of pure niobium surfaces obtained by mechanical scraping and Ar^+-ion sputtering.

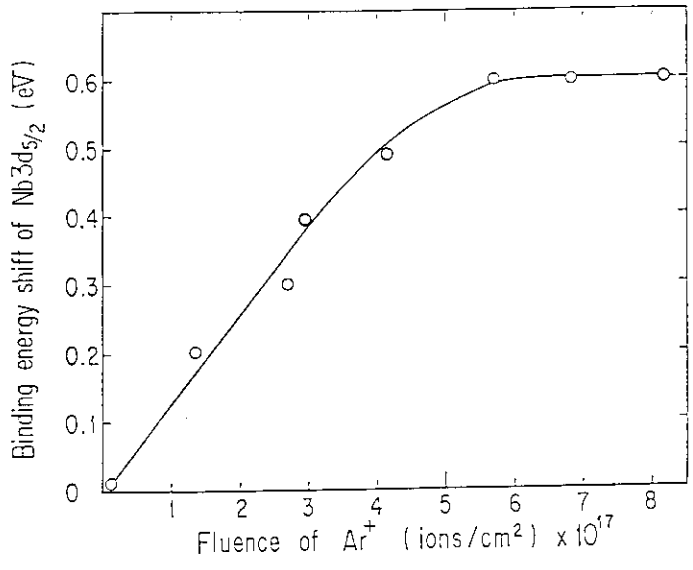

Fig. 2.6 Binding-energy shifts of $Nb3d_{5/2}$ line for Ar^+-ion bombarded niobium metal as a function of ion fluence.

and growth of the vacancy clusters in the surface layer was pointed out[91,92]. In this model, the ion-induced vacancies in the surface layer agglomerate by diffusion resulting in the formation of the porous metal surfaces.

On the other hand, the core-line energies are related to the atomic density of the sample. In fact, the binding energies of the gaseous phase of the transition metals shift to the higher energy side by 2-4 eV from those of the solid phase[93,94]. Thus, the core-line shift to the higher energy side for the ion-bombarded metal is presumably associated with the formation of the porous surfaces whose atomic density is relatively small compared with original metals. To confirm this assumption, the XPS spectra were measured for the porous niobium metal obtained by the following procedure.

First, the niobium hydride $NbH_{0.86}$ was thermally synthesized in the electric furnace by the direct reaction of niobium metal with hydrogen at 570°C. The hybride was then dehydrogenated at 1100°C under a high vacuum. By this treatment, the $Nb3d_{5/2}$ line was moved to 202.6 eV, which is higher by 0.2 eV than that of the mechanically scraped niobium surface. Since there exists no phase transition of niobium metal below its melting point, i.e., 2400°C[95], the dehydrogenated niobium metal preserves the crystal structure of hydride. The phenomenon is similar to the result of the Ar^+-ion bombarded surfaces, though the energy shift is smaller compared with that of the Ar^+-ion bombarded surface. Such an energy discrepancy between dehydrogenated and scraped metals was also observed for vanadium system. The $V2p_{3/2}$ line for dehydrogenated vanadium appears at 512.4 eV, which is higher by 0.3 eV from that of the mechanically scraped vanadium surface.

Considering the results mentioned above, it should be careful to use the data for the sputtered surface as an energy reference of chemical shifts in such metals as titanium, vanadium, yttrium, zirconium and niobium. On the other hand, the energy shifts were not observed in scandium, chromium, nickel and molybdenum, up to the total fluence of 1×10^{18} ions/cm^2. On the basis of the result, the mechanical scraping with a steel file was adopted for the acquisition of the pure metallic surfaces in the following data.

2.3.2 Core-line XPS spectra of scandium

Fig. 2.7 shows the Sc2p XPS spectrum of the hydrogen-ion implanted scandium $Sc:H_{imp}$. For comparison, the spectra of scandium metal, Sc_2O_3 and the thermally synthesized hydride $ScH_{0.68}$ are also presented. The energy shift of the $Sc2p_{3/2}$ line between scandium metal and Sc_2O_3 is 4.2 eV, which is almost equal to that previously reported[96,97]. Although the surface of the $ScH_{0.68}$ sample was covered with a great amount of the oxide, a small peak was observed at 399.1 eV, which shifts by 0.3 eV from that of the $2p_{3/2}$ line for scandium metal. The energy shift is close to that previously reported for the hydrogen-adsorbed scandium metal[97].

On the other hand, the surface of $Sc:H_{imp}$ is also covered with a small amount of oxide. To separate the oxide contributions, the deconvolution of the spectrum was carried out using Gaussian distribution, which is seen in **Fig. 2.8**. As a result, 23.6% of the total area is attributed to the peak corresponding to the surface oxides. The intensity ratios of O1s/Sc2p for Sc_2O_3 and $Sc:H_{imp}$ are 1.47 and 0.335, respectively. The product of the O1s/Sc2p ratio of Sc_2O_3 and 0.236 is 0.346, which is nearly equal to the O1s/Sc2p ratio of $Sc:H_{imp}$. Thus, the O1s peak observed in the spectrum for $Sc:H_{imp}$ results from the oxide overlayer. This implies that the main peak at 399.7 eV does not contain any component corresponding to the Sc-O bond, and is attributable to the Sc-H bond. The peak energies of the $Sc:H_{imp}$ are summarized in **Table 2.2**. As a result, the chemical shift of the $Sc2p_{3/2}$ line for $Sc:H_{imp}$ is 0.9 eV, which is larger than that for $ScH_{0.68}$, i.e., 0.3 eV. Although the core-line XPS spectra

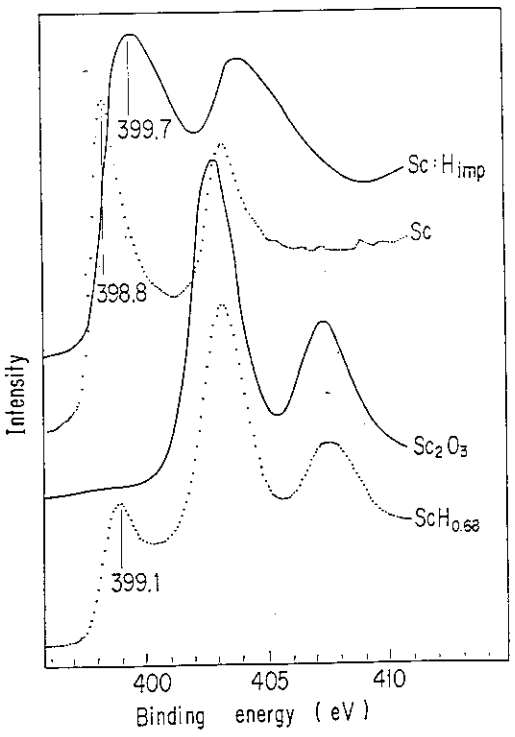

Fig. 2.7 Sc2p XPS spectra of Sc:H_{imp}, Sc, Sc_2O_3 and $ScH_{0.68}$.

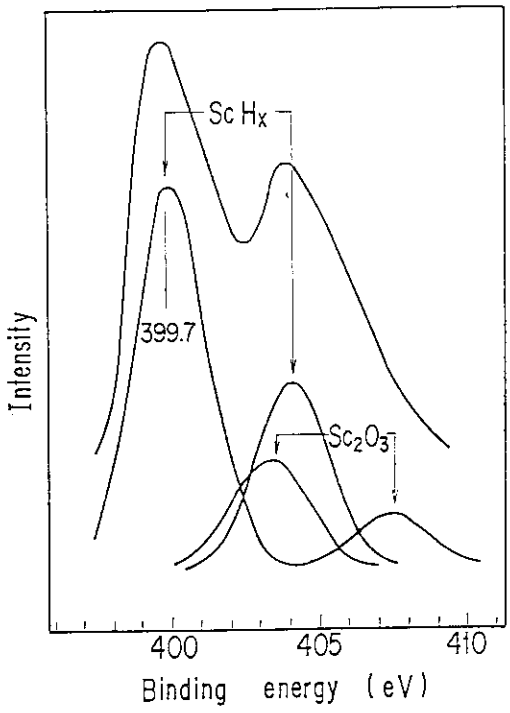

Fig. 2.8 Deconvolution profile of the Sc2p region for Sc:H_{imp} using Gaussian distribution. About 23.6% of the total area is attributed to the oxide-peak.

Table 2.2 Photopeak positions and chemical shifts for Sc metal and hydrogen-implanted scandium Sc:H_{imp}

Line	Position (eV)		Chemical Shift (eV)
	Sc	Sc:H_{imp}	
Sc2s	498.5	499.5	1.0
$Sc2p_{1/2}$	403.5	404.0	0.4
$Sc2p_{3/2}$	398.8	399.7	0.9
Sc3s	51.3	52.0	0.7
Sc3p	28.5	30.3	1.8
Sc3d-H1s	–	~3.0	–

for the stoichiometric hydride ScH_2 could not be obtained because of its fragility, the above result suggests that the hydrogen bombardment brings about the formation of the hydride layer whose composition is close to that of ScH_2 considering that the chemical shift of hydride linearly changes accomanied by the increase in the hydrogen content[83]. Another evidence of hydride formation is obtained by measuring the VB spectra, which will be given in chapter 3.

2.3.3 Core-line XPS spectra of titanium

The Ti2p region of the hydrogen-implanted titanium is displayed in **Fig. 2.9** together with titanium metal, TiO_2 and the thermally synthesized hydride $TiH_{1.97}$. The energy shift of the $Ti2p_{3/2}$ line between titanium metal and TiO_2 is 4.8 eV, which is almost equal to those previously reported[82,83]. The binding energy of the $Ti2p_{3/2}$ line for Ti:H_{imp} shifts

to the higher energy side by 0.3 eV from that for titanium metal. The energy shift is in good agreement with that for the $TiH_{1.97}$ sample, and is almost equal to that previously presented for the thermally synthesized hydride[82].

Fig. 2.10 indicates the deconvolution profile of the spectrum for the $TiH_{1.97}$ sample, which was obtained by the use of Gaussian distribution for a single peak. The profile shows an evidence for the presence of TiO_2 and hydride. In order to check whether the most prominent peak at 454.6 eV contains oxide or not, the intensity ratio of O1s/Ti2p was compared with that of the spectrum for TiO_2. As a result, the obtained O1s/Ti2p ratio for the $TiH_{1.97}$ sample, i.e., 0.47 was much smaller than that for TiO_2, i.e., 1.63. The fact shows

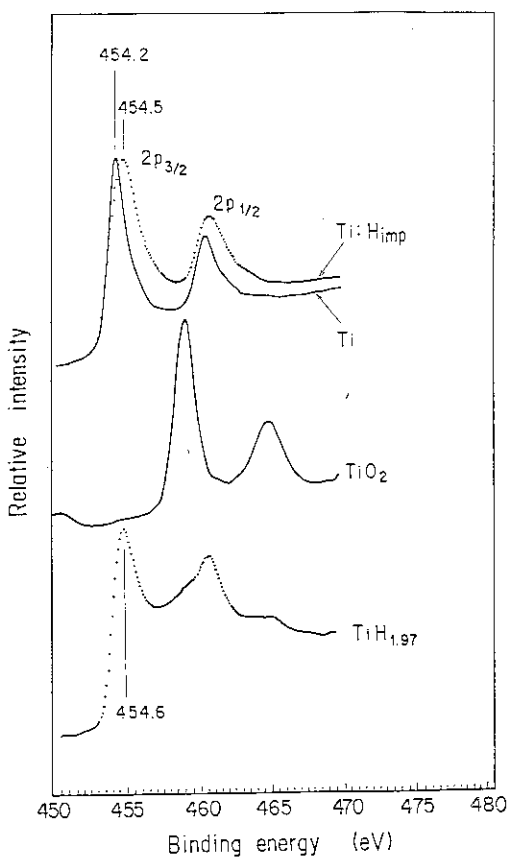

Fig. 2.9 Ti2p XPS spectra of $Ti:H_{imp}$, Ti, TiO_2 and $TiH_{1.97}$.

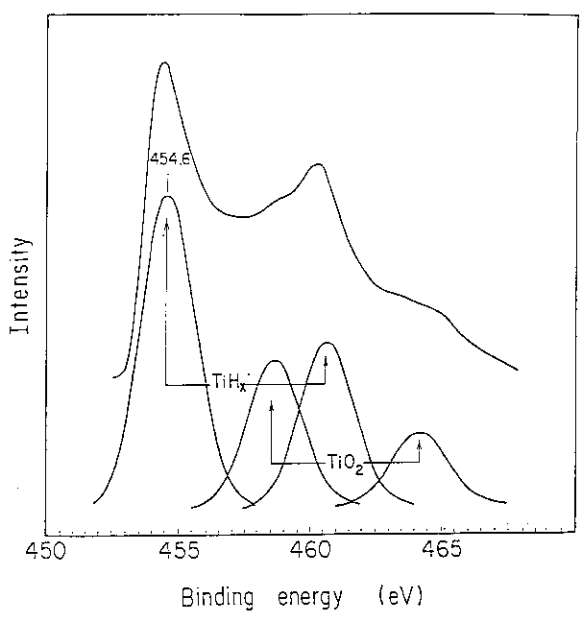

Fig. 2.10 Deconvolution profile of the Ti2p region for $TiH_{1.97}$ using Gaussian distribution. About 30% of the total area consists of the peak corresponding to TiO_2.

Table 2.3 Photopeak positions and chemical shifts for hydrogen-implanted titanium $Ti:H_{imp}$ and thermally synthesized hydride $TiH_{1.97}$

Line	Position (eV)		Chemical Shift (eV)	Position (eV)	Chemical Shift (eV)
	Ti	$Ti:H_{imp}$		$TiH_{1.97}$	
$Ti2p_{1/2}$	460.3	460.5	0.2	460.6	0.3
$Ti2p_{3/2}$	454.2	454.5	0.3	454.6	0.4 (0.4 for $TiH_{2.00}$)[82]
Ti3s	58.9	59.1	0.2	59.3	0.4
Ti3p	33.0	33.4	0.4	33.6	0.6
Ti3d-H1s	–	3.5	–	?	–

that about 30% (0.47/1.63) of the total area of the Ti2p spectrum observed for the $TiH_{1.97}$ sample results from the oxygen of TiO_2. This means that the peak at 454.6 eV does not contain any components attributed to oxide. Another evidence for the presence of the surface hydride was obtained, when the $TiH_{1.97}$ sample was heated at 1100°C in an electric furnace under the vacuum. After this treatment, main peak appeared at 454.2 eV, which is attributable to the position of the metallic state. The core-line energies for $Ti:H_{imp}$, $TiH_{1.97}$, and their chemical shifts from those of the metallic states are summarized in **Table 2.3**.

2.3.4 Core-line XPS spectra of vanadium

Fig. 2.11 indicates the XPS spectra in the V2p region for $V:H_{imp}$, vanadium metal, V_2O_5 and thermally synthesized hydride $VH_{0.55}$. The core-line energies and the chemical shifts are listed in **Table 2.4**. Characteristics observed for the vanadium compounds are similar to those observed for the titanium system. The energy shift of the $V2p_{3/2}$ line between vanadium metal and V_2O_5, i.e., 4.9 eV is almost equal to that previously reported[98-100].

The energy shift of the $V2p_{3/2}$ line for $V:H_{imp}$ from the metallic state, i.e., 0.3 eV is equal to that for the $VH_{0.55}$ sample. The result also suggests a formation of hydride layer by the ion-implantation. The energy shifts of hydrides are smaller than that obtained by Nafedov et al.[82], i.e., 0.8 eV for $VH_{1.93}$, suggesting the low hydrogen-content for $V:H_{imp}$. Since vanadium at ambient temperature has three stable phases of hydride such as V_2H, VH and VH_2[62], the present result suggests that the ion-implanted hydrogen forms the hydride layer whose stoichiometry is close to $VH_{0.5}$.

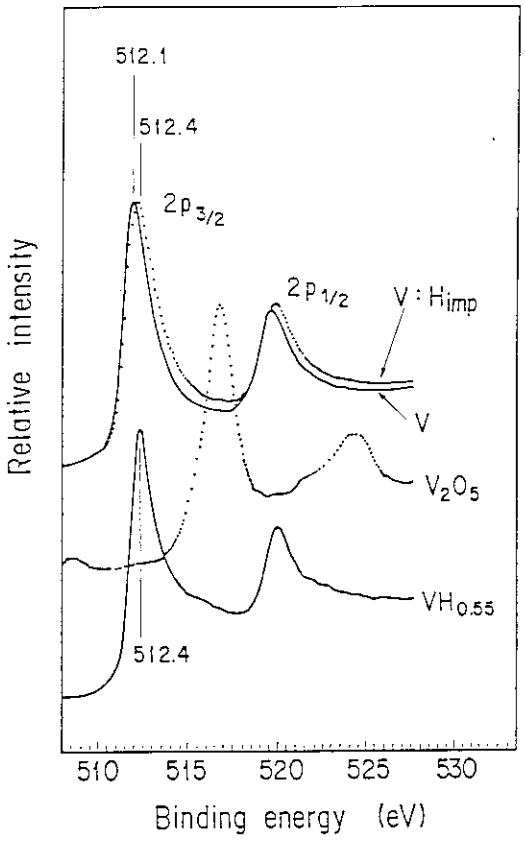

Fig. 2.11 V2p XPS spectra of $V:H_{imp}$, V, V_2O_5 and $VH_{0.55}$.

Table 2.4 Photopeak positions and chemical shifts for hydrogen-implanted vanadium $V:H_{imp}$ and thermally synthesized hydride $VH_{0.55}$

Line	Position (eV) V	Position (eV) $V:H_{imp}$	Chemical Shift (eV)	Position (eV) $VH_{0.55}$	Chemical Shift (eV)
$V2p_{1/2}$	519.8	520.1	0.3	520.1	0.3
$V2p_{3/2}$	512.1	512.4	0.3	512.4	0.3 (0.8 for $VH_{1.93}$)[82]
V3s	66.1	66.3	0.2	66.7	0.6
V3p	37.0	37.3	0.3	37.5	0.5
V3d-H1s	–	5.0	–	4.2	–

2.3.5 Core-line XPS spectra of yttrium

The Y3d XPS spectrum of hydrogen-ion implanted yttrium $Y:H_{imp}$ is shown in **Fig. 2.12**. For comparison, the spectra of yttrium metal, Y_2O_3 and the thermally synthesized hydride $YH_{2.98}$ are also presented. The energy shift of the $Y3d_{5/2}$ line between yttrium metal and Y_2O_3 is 2.7 eV, which is almost equal to that previously reported[96]. As metallic yttrium is highly sensitive to oxidation compared with the other transition metals, the peak corresponding to Y_2O_3 seems to be slightly superposed on the $3d_{5/2}$ peaks in the spectra of the yttrium metal and $Y:H_{imp}$. The surface of the $YH_{2.98}$ sample was also covered with a large amount of oxide. To separate the oxide contribution in these spectra, deconvolutions were carried out, as displayed in **Fig. 2.13**. The ratios of the areas of the oxide peaks to the total areas of the 3d line are listed in **Table 2.5**, together with the intensity ratios of O1s/Y3d. In all cases, the area ratios multiplied by the O1s/Y3d ratios of Y_2O_3, i.e., 0.66 eV are nearly equal to the corresponding O1s/Y3d ratios. The results imply that the $3d_{5/2}$ peaks at 155.9-156.4 eV for the yttrium metal, $Y:H_{imp}$ and $YH_{2.98}$ do not contain any peaks other than Y-O bond. The core-line energies for the yttrium metal and $Y:H_{imp}$ are summarized in **Table 2.6**.

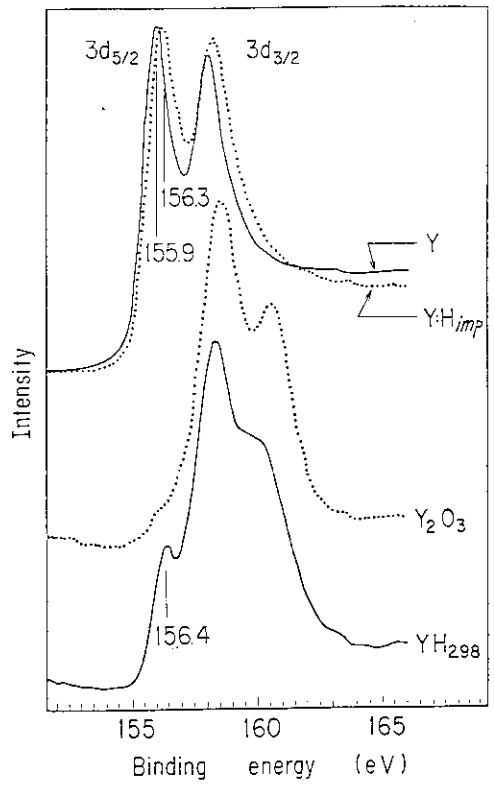

Fig. 2.12
Y3d XPS spectra of $Y:H_{imp}$, Y, Y_2O_3 and $YH_{2.98}$.

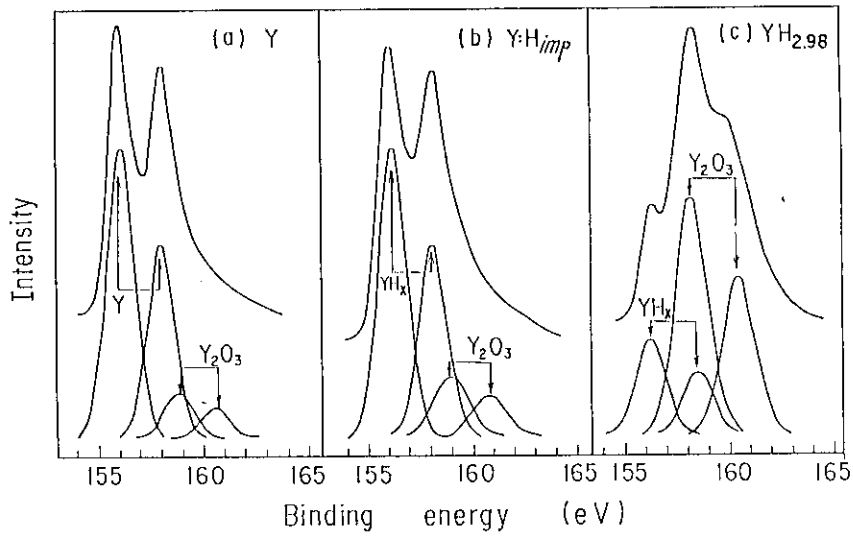

Fig. 2.13 Deconvolution profiles of the Y3d region for yttrium metal (a), $Y:H_{imp}$ (b) and $YH_{2.98}$ (c), using Gaussian distribution. The ratios of the areas of the oxide peaks to the total areas of the 3d line are summarized in **Table 2.5**.

Table 2.5 Peak area ratios of $Y3d_{(oxide)}/Y3d_{(total)}$ (≡R) obtained by deconvolution profiles in **Fig. 2.13**, and peak intensity ratios of O1s/Y3d

Sample	R	O1s/Y3d	R×0.66
Y	0.13	0.084	0.086
$Y:H_{imp}$	0.21	0.13	0.14
$YH_{2.98}$	0.73	0.45	0.48
Y_2O_3	1.00	0.66	0.66

Table 2.6 Photopeak positions and chemical shifts for Y metal and hydrogen-implanted yttrium $Y:H_{imp}$

Line	Position (eV)		Chemical Shift (eV)
	Y	$Y:H_{imp}$	
$Y3p_{3/2}$	299.3	299.6	0.3
$Y3d_{3/2}$	157.9	158.2	0.3
$Y3d_{5/2}$	155.9	156.3	0.4
Y4p	24.1	24.3	0.2
Y4d-H1s	–	~3.0	–

The $Y3d_{5/2}$ energy of the $Y:H_{imp}$ shifts to the higher energy side by 0.4 eV from that of the $YH_{2.98}$ sample. It is reported that there exist two stable hydrides of yttrium, i.e., YH_2 and YH_3[62]. The present result suggests that the ion-implanted hydrogen forms the hydride layer whose composition is close to YH_3.

2.3.6 Core-line XPS spectra of zirconium

Fig. 2.14 shows the Zr3d region of the hydrogen-ion implanted zirconium $Zr:H_{imp}$.

The spectral pattern and peak position of $Zr:H_{imp}$ were independent of the total fluence from 3×10^{17} to 1×10^{18} ions/cm^2. For comparision, the spectra for zirconium metal, ZrO_2 and the $ZrH_{1.64}$ sample are also presented. The energy shift of the $Zr3d_{5/2}$ line between zirconium metal and ZrO_2 is 4.3 eV, in agreement with the chemical shift previously reported[86,96,101]. On the other hand, the surface of the $ZrH_{1.64}$ sample was found to be contaminated with a considerable amount of ZrO_2. This was also confirmed from the presence of the intense O1s line at 531.0 eV. Neverthless, a distinct 179.6-eV peak of the sample and of $Zr:H_{imp}$, in **Fig. 2.14**, could be assigned to that from the hydride, because its chemical shift from the metallic state is 0.6 eV, in good agreement with a reported value for $ZrH_{1.65}$[86]. Other firm evidence for the presence of the hydride was obtained by heating the $ZrH_{1.64}$ sample at a temperature over thermal decomposition in the vacuum. This treatment brought about the disappearence of the 179.6-eV peak and the appearence of a new photopeak at 179.0 eV attributable to the $Zr3d_{5/2}$ line for the metallic state.

Discrepancy in the signal intensity of the Zr3d region for $Zr:H_{imp}$ from the spin-orbit coupling ratio is due to the superposed contribution of the oxide overlayer. Monitoring of the O1s line revealed that the amount of the oxide impurity estimated from the O1s-to-Zr3d ratio is about 25% in terms of ZrO_2, though definite structure attributable to the oxide(s) is invisible in the Zr3d spectrum of $Zr:H_{imp}$. The formation of the oxide overlayer is presumably due to implantation of O_2^+ ions which may be contained as an impurity in the

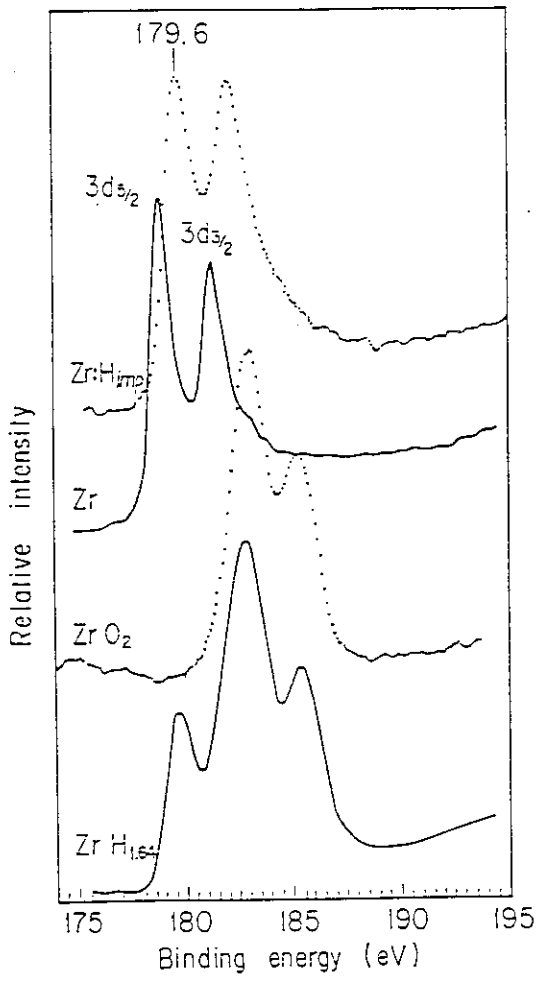

Fig. 2.14 Zr3d XPS spectra of $Zr:H_{imp}$, Zr, ZrO_2 and $ZrH_{1.64}$.

hydrogen-ion beam.

It is apparent that the XPS in the present work is far more sensitive to the oxide(s) than to the hydride, taking the penetration depth of the ions into account. The projected range of an 8-keV O_2^+ ion (4 keV/O atom) is estimated to be less than 5 nm in zirconium metal[102], while that of an 8-keV H_2^+ ion (4 keV/H atom) is about 20 nm[103]. Thus oxygen ions would be accumulated in the surface layer including the escape depth of the Zr3d photoelectron, viz., 1.5 nm. To confirm this assumption, the $Zr:H_{imp}$ surface was etched with 5-keV Ar^+ ions for 2 minutes. This treatment made the right-hand side of the $Zr3d_{5/2}$ region for $Zr:H_{imp}$ in **Fig. 2.14** lower and increased the sharpness of the 179.6-eV peak. In addition, an abrupt decrease in the peak intensity of the O1s line was observed.

The core-line energies of the hydride determined from the $Zr:H_{imp}$ sample and their shifts from the metallic state are summarized in **Table 2.7**. The chemical shifts of the Zr4s and Zr4p lines are fairly large compared with the other core-lines. The observation agrees well with the results by Veal et al.[86] who have reported 0.7 and 1.0 eV for the chemical shifts of the $Zr3d_{5/2}$ and Zr4p lines for $ZrH_{1.65}$, respectively.

Table 2.7 Photopeak positions and chemical shifts for Zr metal and hydrogen-implanted zirconium $Zr:H_{imp}$

Line	Position (eV)		Chemical Shift (eV)
	Zr	$Zr:H_{imp}$	
Zr3s	430.2	431.6	1.4
$Zr3p_{3/2}$	329.9	330.7	0.8
$Zr3d_{3/2}$	181.4	182.0	0.6
$Zr3d_{5/2}$	179.0	179.6	0.6
Zr4p	27.5	28.9	1.4
Zr4d-H1s	–	3.4	–

2.3.7 Core-line XPS spectra of niobium

Fig. 2.15 displays the Nb3d region of hydrogen-ion implanted niobium $Nb:H_{imp}$, niobium metal, Nb_2O_5 and the $NbH_{0.86}$ sample. The spectral pattern and the peak position of $Nb:H_{imp}$ were independent of the total fluence of the hydrogen ions as in the case of $Zr:H_{imp}$.

Because of charging effects during the XPS measurement, the spectrum of insulating Nb_2O_5 was found to shift to higher binding energy. Therefore, the peak position of the $Nb3d_{5/2}$ line for the most oxidized species on the $NbH_{0.86}$ surface was coincided with that for Nb_2O_5.

With this alignment, the separation energy of the $Nb3d_{5/2}$ line between niobium metal and Nb_2O_5 is 5.5 eV, in agreement with the chemical shift measured by previous work[104].

A tailing to the higher binding-energy side and an increase in the full width at half maxima of the Nb3d spectrum for $Nb:H_{imp}$, compared with niobium metal, imply that the $Nb:H_{imp}$ surface is composed of several different chemical species. The deconvolution shown in **Fig. 2.16** gives evidence for the presence of NbO_2 and an unidentified species. Since the photoelectron from the latter species has the same binding energy as that of a 203.2-eV peak for the $NbH_{0.86}$ sample, the unidentified species is the hydride. The core-line energies of $Nb:H_{imp}$ and their chemical shifts are summarized in **Table 2.8**.

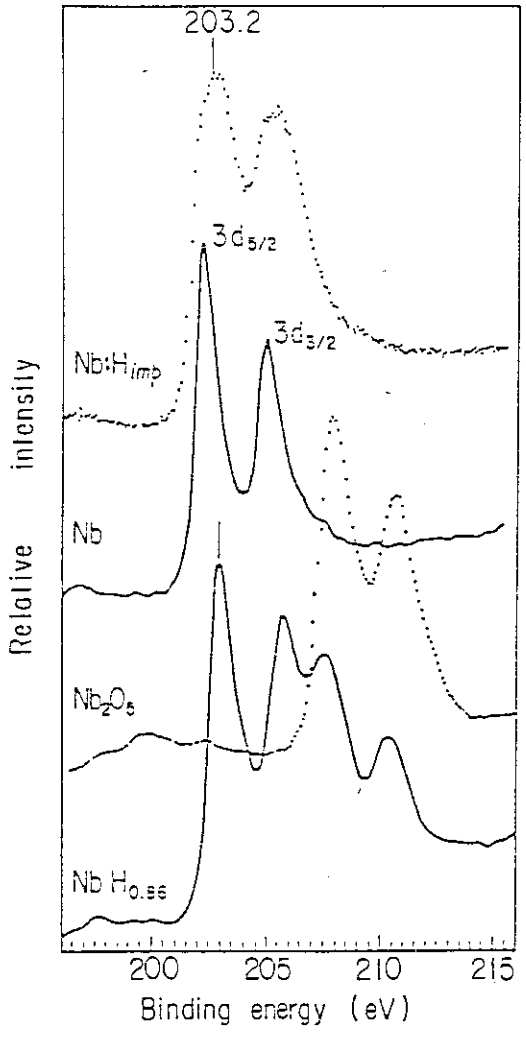

Fig. 2.15 Nb3d XPS spectra of $Nb:H_{imp}$, Nb, Nb_2O_5 and $NbH_{0.86}$.

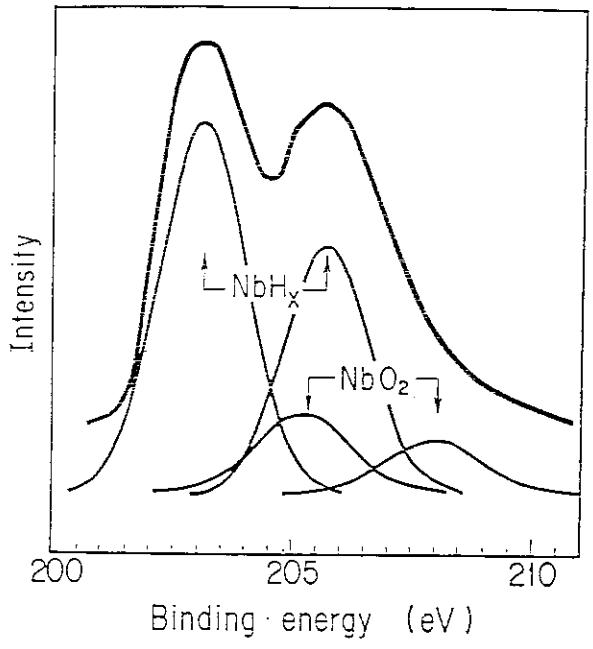

Fig. 2.16 Deconvolution profile of the Nb3d region for $Nb:H_{imp}$ using Gaussian distribution.

Table 2.8 Photopeak positions and chemical shifts for Nb metal and hydrogen-implanted niobium $Nb:H_{imp}$

Line	Position (eV)		Chemical Shift (eV)
	Nb	$Nb:H_{imp}$	
Nb3s	467.1	467.7	0.6
$Nb3p_{3/2}$	360.7	361.5	0.8
$Nb3d_{3/2}$	205.2	205.9	0.7
$Nb3d_{5/2}$	202.4	203.2	0.8
Nb4p	31.0	31.7	0.7
Nb4d-H1s	–	4.6	–

2.3.8 Core-line XPS spectra of chromium, nickel and molybdenum

Figs. 2.17 and **2.18** indicate the 2p XPS spectra for chromium and nickel compounds, respectively, and the 3d XPS spectra for molybdenum compounds are displayed in **Fig. 2.19**. Even after the hydrogen-ion bombardment, the peak energies of the core-lines for these metals did not change up to a total fluence of 3×10^{18} atoms/cm^2, except for the small overlapping of the oxide-peaks.

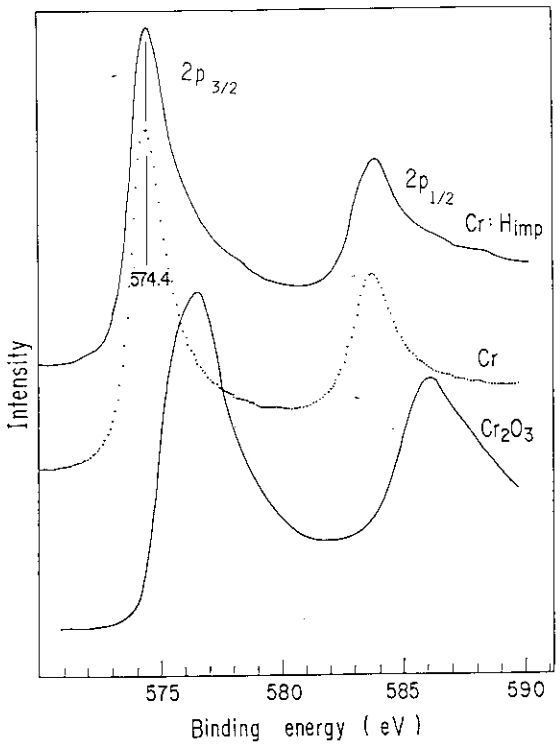

Fig. 2.17 Cr2p XPS spectra of Cr:H_{imp}, Cr and Cr_2O_3.

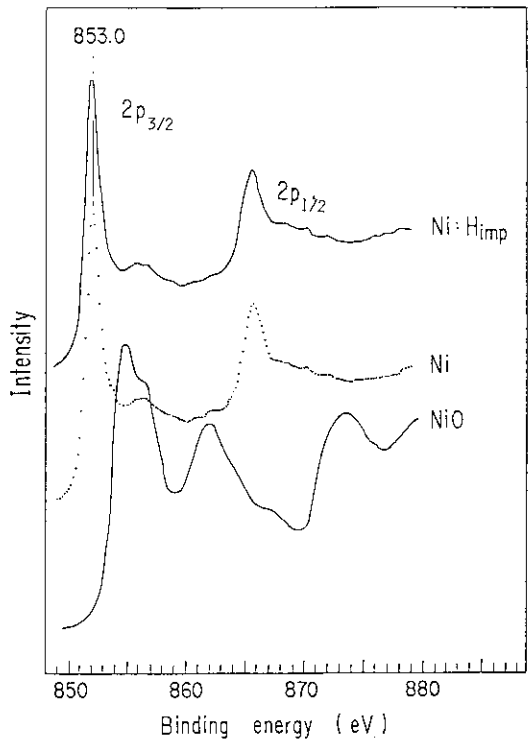

Fig. 2.18 Ni2p XPS spectra of Ni:H_{imp}, Ni and NiO.

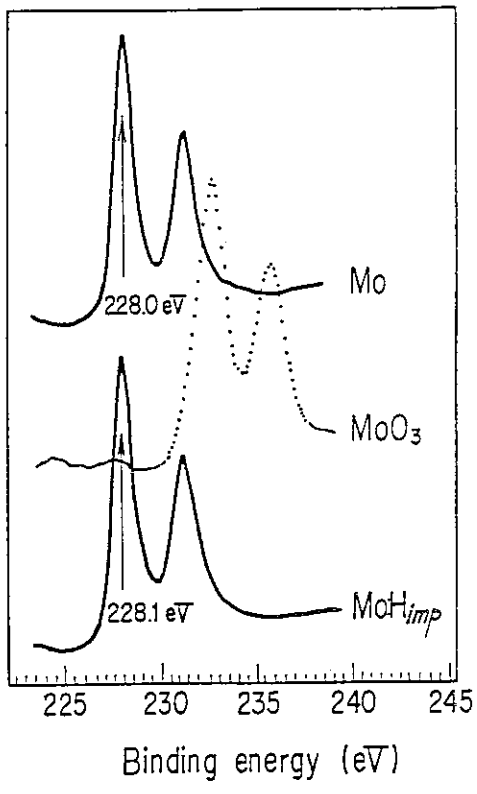

Fig. 2.19 Mo3d XPS spectra of Mo:H_{imp}, Mo and MoO_3.

According to Bϕttiger et al.[105], considerable amount of hydrogen is trapped in molybdenum, when bombarded with energetic hydrogen ions. They have measured the depth profiles of hydrogen in molybdenum by a resonance nuclear reaction $H(^{19}F,\alpha\gamma)^{16}O$. As a result, they could observe hydrogen atoms at the surface after the 16-keV hydrogen-ion bombardment. Trapping of hydrogen has been also confirmed for nickel exposed to 3-keV H^+ ions[106]. Thus, most of hydrogen ions seem to be implanted in the present metals, whereas there exists no evidence for the formation of the metal-H bond(s) in the core-line spectra. Therefore, it is presumed that hydrogens implanted in molybdenum and nickel at room temperature are trapped as an atomic or molecular form in the metal lattice or defect produced by the ion-bombardment. This assumption is consistent with the results by Bϕttiger et al.[105], who have showed that the trapping efficiency of ion-bombarded hydrogen in molybdenum is enhanced by the pre-bombardment by He^+-ions.

2.3.9 Dose-dependences of chemical shifts

The XPS spectra so far obtained are measured over the fluence of 1×10^{18} atoms/cm^2. To examine the dependences of the hydrogen-ion fluences on the XPS spectra, the core-line spectra were also taken at the lower fluences. **Fig. 2.20** shows the changes in the chemical shifts of the $2p_{3/2}$ or $3d_{5/2}$ orbital for hydrogen-implanted metals as a function of the fluence. The figure reveals two important facts about the hydrogen-ion bombardment.

First, the chemical shifts mostly grow up with the increase in the fluence up to 1×10^{18} atoms/cm^2. At this fluence, hydrogen atoms are accumulated at the metal surface which can be detected by the XPS (~1.5 nm). On the other hand, the chemical shifts are saturated over the fluence of 1×10^{18} atoms/cm^2. The saturated values are nearly equal to those of the corresponding hydrides obtained by thermal reaction. The saturation of hydrogen at the metal surface is in consistent with the results previously reported for deutron-implanted titanium[75] and zirconium[107], which have been obtained by resonance nuclear reactions. Thus the implanted hydrogen, after saturation in the surface layer, diffuses from the implanted layer to the bulk. This consideration supports the Local Mixing Model proposed by Doyle et al.[108–110]. In this model, hydrogen implanted in solid in advance is considered to be replaced atoms finally re-emitted from surface, resulting in a final reemission rate close to

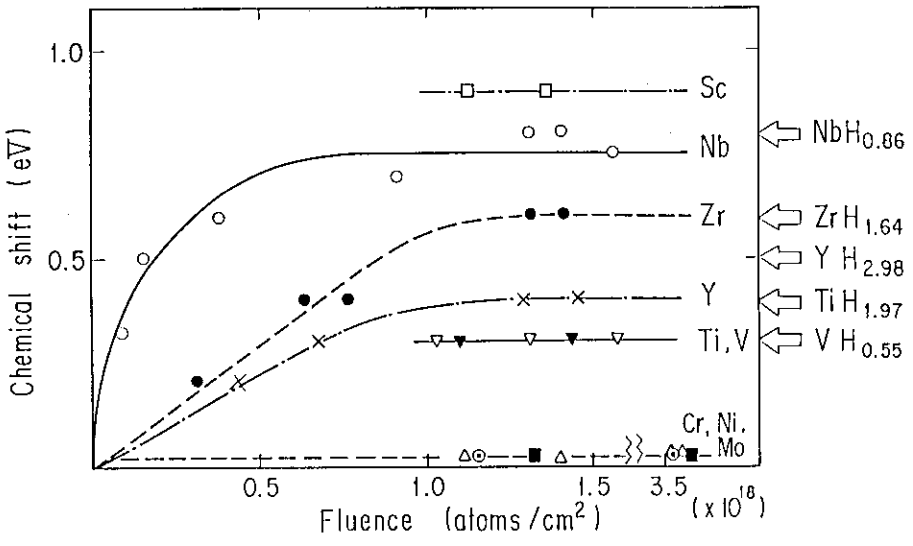

Fig. 2.20 Changes in the $2p_{3/2}$ or $3d_{5/2}$ chemical shifts for the hydrogen-implanted metals as a function of the ion fluences.

100% at high fluence. If hydrogens occupy fully in the stable interstitial site of the metal lattice, hydrogen to metal ratio becomes 6. The present observation revealed that the content of hydrogens which form chemical bonds with these metals do not exceed stoichiometric H/metal ratios even by means of the ion implantation. The result is also consistent with a fact that the free energies of formation of titanium and niobium hydrides rapidly increase when H/metal ratios exceed 2 and 1, respectively[62].

Secondly, the transition metals examined are divided into two groups, i.e., the metals which form hydride layers by the ion bombardments and those which do not. The difference in this property is related to the following thermodynamical parameters. The metals in the former group easily absorb hydrogen to form relatively stable hydrides, and solution of hydrogen in these metals is strongly exothermic. Whereas the metals in the latter group hardly react with hydrogen, and solution of hydrogen takes place through endothermic reaction[62]. The present results suggest that there exists no appreciable difference in the reaction product between ion-implantation and thermal process in the case of the metal-hydrogen system.

Whether the hydrogen-ion implanted metal forms hydride layer or not will be further discussed in section 3.3.8 in relation to the thermochemical properties of the metal-hydrogen systems.

2.4 Conclusions

1) Bombardments of 8-keV Ar^+ ions on titanium, vanadium, yttrium, zirconium and niobium cause the core-line energy shifts from those of the corresponding metallic surfaces obtained by the mechanical scraping. This is associated with the formations of amorphous phases by the ion-bombardments.

2) The core-line chemical shifts of the metal $2p_{3/2}$ lines for $Sc:H_{imp}$, $Ti:H_{imp}$ and $V:H_{imp}$ are 0.9 eV, 0.3 eV and 0.3 eV, respectively, from the peak energies of the corresponding metallic states. The energy shifts are saturated over the fluences of 1×10^{18} atoms/cm^2. The energy shifts for $Ti:H_{imp}$ and $V:H_{imp}$ are well consistent with those of the thermally synthesized hydrides, i.e., $TiH_{1.97}$ and $VH_{0.55}$, which suggests that hydrogen-ion bombardments induce the formation of hydrides whose chemical compositions are nearly equal to those of the thermally synthesized ones.

3) The core-line shifts of the metal $3d_{5/2}$ lines for $Y:H_{imp}$, $Zr:H_{imp}$ and $Nb:H_{imp}$ are 0.4 eV, 0.6 eV and 0.8 eV, respectively, from the peak energies of the corresponding metallic states. The energy shifts are almost the same as those of the thermally synthesized hydrides, i.e., $YH_{2.98}$, $ZrH_{1.64}$ and $NbH_{0.86}$. These results indicate the formations of hydride phase by the hydrogen-ion bombardments.

4) The core-line spectra of chromium, nickel and molybdenum bombarded with hydrogen-ions show no appreciable change up to the total fluences of 3×10^{18} atoms/cm^2. Thus the hydrogen implanted in these metals are supposed to be trapped as atomic or molecular form in the metal lattice or defect.

3. Valence-band XPS spectra of transition metals bombarded with energetic hydrogen ions

3.1 Introduction

As indicated in the previous chapter, the core-line XPS spectra revealed that the hydrogen-ion bombardments on some transition metals induce the formation of hydride layers in the surface region of the targets. The formation of the metal-H bond accompanies the hybridization of H1s and metal-d orbitals. This, in turn, causes the changes in the valence-band (VB) structure of the host metal. Thus, the measurements of the XPS spectra in the VB region for the hydrogen-implanted metals seem to provide the information on the electronic structure as well as level structure of the hydride.

Regarding the VB structure of the stoichiometric hydrides, the metal-H bonds have been investigated for some transition-metal hydrides. From the theoretical viewpoint, the bond-structures of these hydrides have been investigated based on the band theory[111–121] or molecular-orbital calculations[81,122,123]. In these works, it has been revealed that there exist new bonding levels attributed to the metal-H bonds at 4-8 eV below the Fermi level.

Photoelectron spectroscopy (PES) is one of the methods to elucidate the nature of the metal-H bonds, though in most cases yield of photoelectron from H1s orbital is less than the detection limit. Thus, several investigators have made attempts at the indirect observations of the metal-H bonds for thermally synthesized hydrides or hydrogen-adsorbed metals by means of UPS[124,125] or XPS[83,85,86].

In this chapter, the VB-XPS spectra are presented for the hydrogen-bombarded 3d and 4d transition metals, and the spectra obtained are compared with those obtained by the theoretical calculations.

3.2 Experimental

All the samples used and the condition of the hydrogen-ion bombardments are the same as those described in chapter 2. Accumulations of the VB spectra required more than 10 hours to obtain good S/N ratio.

3.3 Results and discussion

3.3.1 VB-XPS spectra of scandium

The XPS spectrum in VB region for $Sc:H_{imp}$ is shown in **Fig. 3.1** together with those for scandium metal, Sc_2O_3 and the $ScH_{0.68}$ sample. The curve displayed as open circles represents a spectrum calculated for ScH_2 by means of discrete variational (DV)-Xα cluster method[123]. In the spectra for $Sc:H_{imp}$ and the $ScH_{0.68}$ sample, broad photopeaks resulting from the oxide overlayer are observed at 5-9 eV below the Fermi level. Besides the oxide peaks, new photopeaks seem to be observed in both spectra at 3-5 eV, which are slightly overlapped by the oxide peaks. To eliminate the contribution from the oxide overlayer, the peaks of the surface oxides were subtracted from the spectra for $Sc:H_{imp}$ and $ScH_{0.68}$ as a following procedure.

First, the spectrum was taken for scandium metal exposed to oxygen at a pressure of

5×10^{-6} Pa for 10 sec. The spectrum for the oxygen-adsorbed sample was subtracted from those for $Sc:H_{imp}$ and $ScH_{0.68}$ on a point-by-point basis. **Fig. 3.2** displays the subtracted spectrum together with those for $Sc:H_{imp}$, $ScH_{0.68}$ and oxygen-adsorbed scandium metal. In these procedures, the spectral intensity is normalized at the peak positions of the O2s lines. Even after this treatment, broad peaks were observed at 3.0 eV for $Sc:H_{imp}$ and 5.0 eV for $ScH_{0.68}$, respectively. The peak position in the subtracted spectrum for $ScH_{0.68}$ is almost equal to that in the calculated spectrum seen in **Fig. 3.1**. The VB spectrum of the Ar^+-ion bombarded scandium metal was also taken, however any photopeaks were not observed in the subtracted spectrum. The fact shows that the peak at 3.0 eV in the subtracted spectrum for $Sc:H_{imp}$ is attributable not to the radiation damage but to the Sc-H bond, though the peak position is lower by ~2.0 eV than the calculated one.

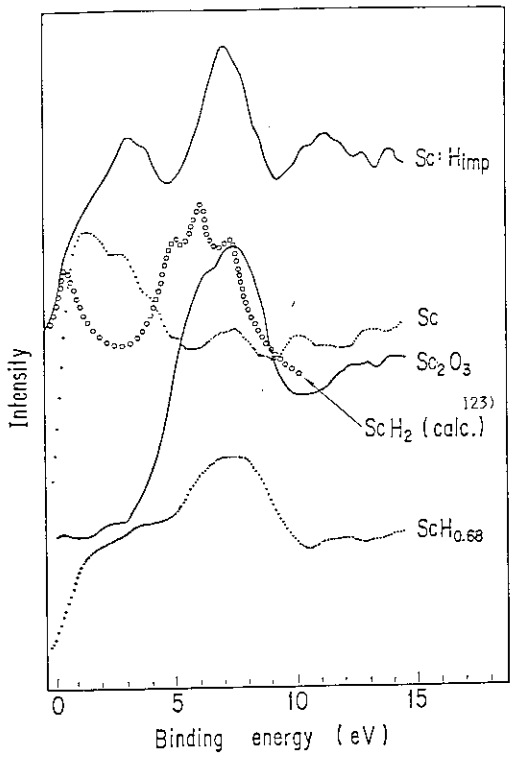

Fig. 3.1 VB XPS spectra of $Sc:H_{imp}$, Sc, Sc_2O_3 and $ScH_{0.68}$. A curve with open circles is spectrum calculated for ScH_2, taken from ref. 123.

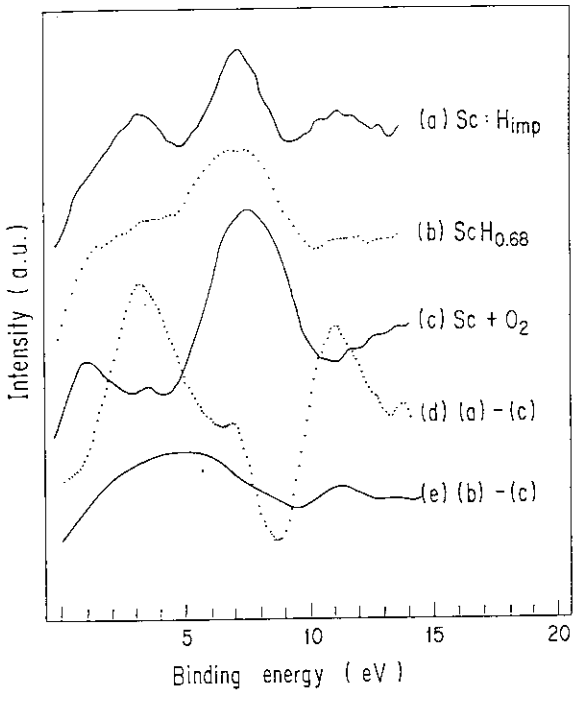

Fig. 3.2 VB XPS spectra of $Sc:H_{imp}$ (a), $ScH_{0.68}$ (b) and scandium metal exposed to oxygen (c). Oxygen was adsorbed at a pressure of 5×10^{-6} Pa for 10 sec. Curves (d) and (e) were obtained by subtracting curve (c) from (a) and (b), respectively, after being normalized at the peak position of the O2s line.

3.3.2 VB-XPS spectra of titanium

Fig. 3.3 displays the VB spectrum of $Ti:H_{imp}$ together with those of titanium metal, TiO_2 and $TiH_{1.97}$. A curve displayed as open circles represents a spectrum theoretically calculated for TiH_2 by means of DV-Xα cluster method[81]. New photopeaks are observed at 3.5 eV and 7.5 eV for $Ti:H_{imp}$. The binding energy of the former peak is lower by 1.5-2.5 eV than those previously reported for $TiH_{1.8}$[83], $TiH_{1.5}$[125] and hydrogen-adsorbed titanium[126]. It is also lower by 2.5 eV than the value calculated for TiH_2[81]. The damage layer may be produced by the hydrogen-ion bombardment. However, the peak at 3.5 eV could be attributed

to one of the components of the Ti-H bonding level, because such peak was not observed in the spectrum for titanium bombarded with Ar^+ ions up to the total fluence of 1×10^{18} ions/cm^2.

In spite of the introduction of highly pure hydrogen into the present ion-gun shown in **Fig. 2.2**, the peak corresponding to the O1s line was observed in the wide scan of Ti:H_{imp}. The ratio of the peak intensity for O1s/Ti2p was 0.28. This is due to the adsorption of oxygen during the ion bombardment. In order to check whether the peak at 3.5 eV in the VB spectrum for Ti:H_{imp} results from the adsorbed oxygen or not, the VB spectrum was also taken for titanium metal exposed to oxygen at a pressure of 7×10^{-4} Pa for 2 min. The VB spectrum for the oxygen-adsorbed sample was displayed as curve (b) in **Fig. 3.4** together with that for Ti:H_{imp} as curve (a). The curve (c) was obtained by subtracting the curve (b) from the curve (a) on a point-by-point basis. After this treatment, the peak at 3.5 eV was clearly observed in curve (c), which shows that the peak in the VB spectrum for Ti:H_{imp} is not attributed to the adsorbed oxygen but to the Ti-H bond as in the case of Sc:H_{imp}. On the basis of these results, it is concluded that the ion-implanted hydrogen in titanium forms a hydride layer on the metal surface, which is consistent with the core-line spectral change shown in the previous chapter.

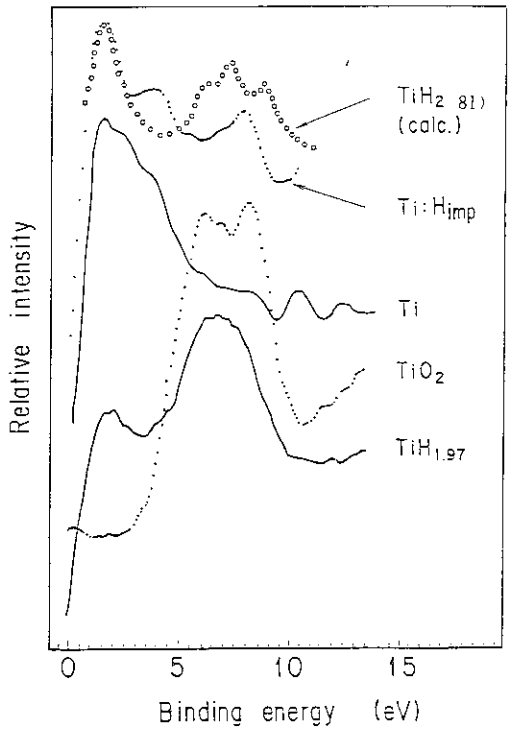

Fig. 3.3 VB XPS spectra of Ti:H_{imp}, Ti, TiO_2 and $TiH_{1.97}$. A curve with open circles is spectrum calculated for TiH_2, taken from ref. 81. Photopeaks at 5-9 eV which are observed for Ti:H_{imp}, TiO_2 and $TiH_{1.97}$ correspond to the surface oxides. The peak at 3.5 eV for Ti:H_{imp} is attributed to the Ti3d-H1s bond.

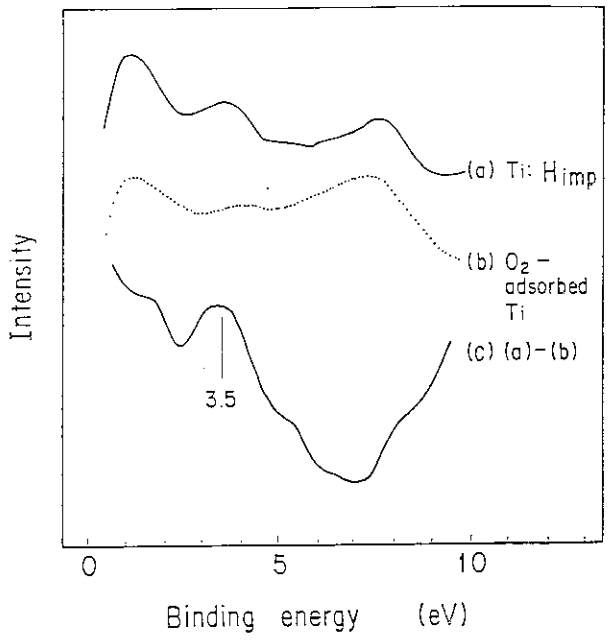

Fig. 3.4 VB XPS spectra of Ti:H_{imp} (a) and titanium metal exposed to oxygen (b). Oxygen was adsorbed at a pressure of 7×10^{-4} Pa for 2 min. Curve (c) was obtained by subtracting curve (b) from curve (a), after normalized at the peak position of the O2s line.

3.3.3 VB-XPS spectra of vanadium

The VB spectra for the vanadium compounds are displayed in **Fig. 3.5**. The spectrum calculated for VH_2 by means of DV-Xα method[81] is also indicated as open circles. A spectral trend obtained is a little different from that for the titanium system. New photopeaks observed at 5.0 eV for $V:H_{imp}$, and at 4.2 eV for $VH_{0.55}$ are apparently attributed to the V3d-H1s bond. The binding energies of these peaks are almost the same as those previously observed for $VH_{1.0}$[121] in the photoelectron spectra with synchrotron radiation, and are approximately equal to those calculated for VH_2, i.e., 6 eV[81]. The result indicates that the ion-implanted hydrogen in vanadium forms hydride layer whose chemical structure is similar to that synthesized by thermal reaction. The fact is in consistent with the result obtained by V2p XPS spectra (sec. 2.3.4).

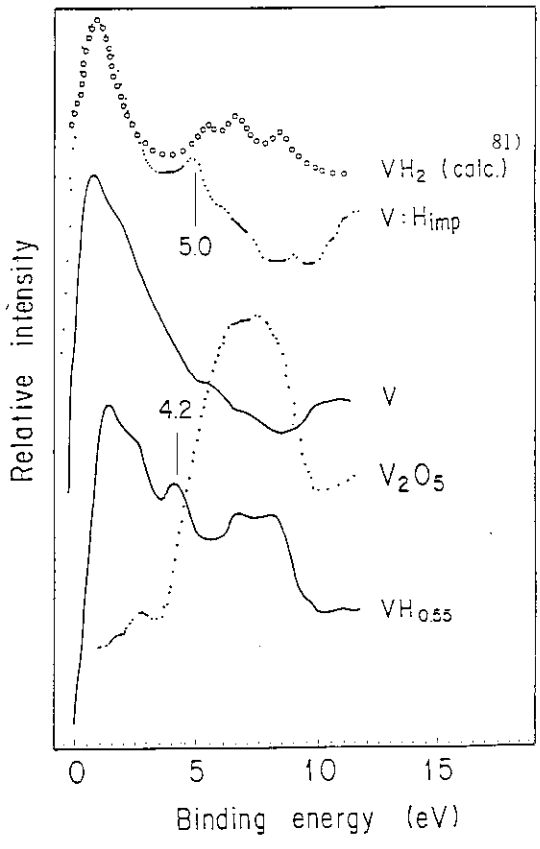

Fig. 3.5 VB XPS spectra of $V:H_{imp}$, V, V_2O_5 and $VH_{0.55}$. A curve displayed as open circles is spectrum calculated for VH_2, taken from ref. 81. The peaks at 5.0 eV for $V:H_{imp}$ and at 4.2 eV for $VH_{0.55}$ are attributed to the V3d-H1s bond.

3.3.4 VB-XPS spectra of yttrium

The VB spectrum of $Y:H_{imp}$ is shown in **Fig. 3.6** together with those of yttrium metal, Y_2O_3 and $YH_{2.98}$. The curve indicated as open circles represents a spectrum theoretically calculated for YH_2 by means of DV-Xα cluster method[123]. In the spectra for $Y:H_{imp}$ and the $YH_{2.98}$ sample, broad photopeaks resulting from the oxide overlayer are observed at 5-8 eV. Furthermore new photopeaks appear at 2.5-3.0 eV.

To eliminate the contribution of the oxide overlayer, the spectral subtraction was

done by the same procedure as those described for scandium and titanium systems. The oxygen-adsorbed yttrium was obtained by exposing yttrium metal to oxygen at a pressure of 7.5×10^{-6} Pa for 20 sec. **Fig. 3.7** displays the VB spectra of $Y:H_{imp}$ and $YH_{2.98}$ which were obtained by subtracting the contribution of the oxygen adsorption. In the subtracted spectrum for $YH_{2.98}$, a broad peak is observed at 5 eV, which is almost in consistent with both the calculated values[116,123] and the experimental value previously obtained by UPS[124]. Whereas, the peak energy in the subtracted spectrum for $Y:H_{imp}$ is lower by 3-4 eV than that in the calculated spectra. Neverthless, the peak is attributable to one of the components of the Y4d-H1s bonding level, since the Ar^+-ion bombardment does not bring about an appearence of such a peak.

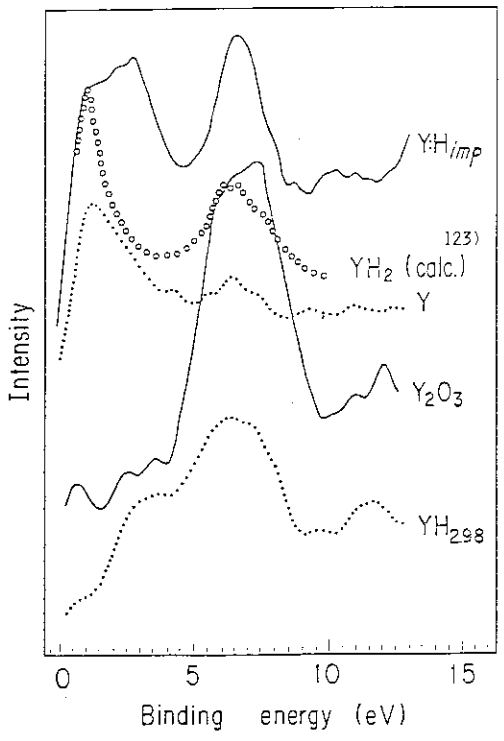

Fig. 3.6 VB XPS spectra of $Y:H_{imp}$, Y, Y_2O_3 and $YH_{2.98}$. A curve displayed as open circles is spectrum calculated for YH_2, taken from ref. 123.

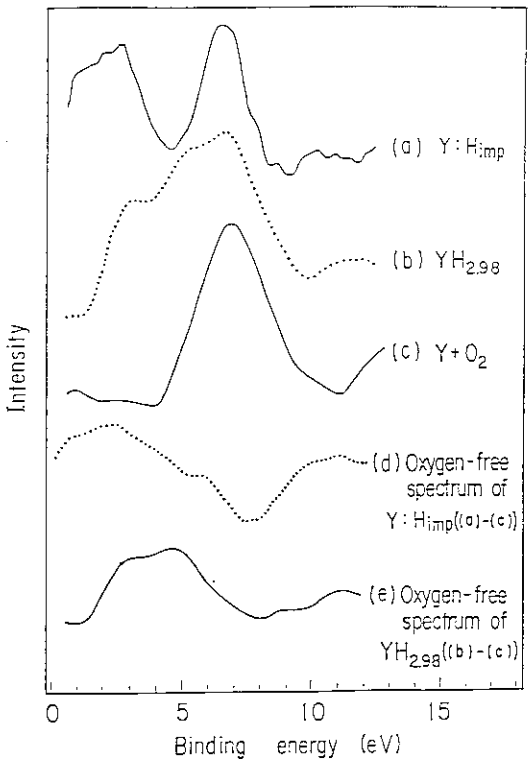

Fig. 3.7 VB XPS spectra of $Y:H_{imp}$ (a), $YH_{2.98}$ (b) and yttrium metal exposed to oxygen (c). Oxygen was adsorbed at a pressure of 7.5×10^{-6} Pa for 20 sec. Curves (d) and (e) were obtained by subtracting curve (c) from (a) and (b), respectively, after being normalized at the peak position of the O2s line.

3.3.5 VB-XPS spectra of zirconium

Veal et al.[86] have found, by means of the data-separation technique, that the Zr-H bond ranges from 4 to 9 eV below the Fermi level. However, our attempt to extract a pure hydride spectrum showed that the reproducibility in the $Zr:H_{imp}$-ZrO_2 separation procedure is not too good because of complexity of the spectral pattern (**Fig. 2.14**) in 3-9 eV. Therefore, the attention is focused mainly on a new photopeak found in the present work.

Fig. 3.8 shows the VB regions for $Zr:H_{imp}$, zirconium metal and oxygen-adsorbed zirconium. In order to determine the origin of the 3.4-eV peak of $Zr:H_{imp}$, the last spectrum

was obtained by exposing a clean metallic surface to oxygen at a pressure of 5×10^{-5} Pa until the O1s-to-Zr3d ratio became equivalent to that of $Zr:H_{imp}$. The presence of the well-defined Fermi edge and chemical shift of 1.0 eV in the Zr4p line indicate that the adsorbed surface is composed of the metallic state and ZrO_2. It is also apparent that the oxygen adsorption does not induce any new photopeak at around 3-4 eV in the binding energy. Furthermore, exposure of zirconium metal to 5000-L (1 L = 1 langmuir = 7.5×10^{-5} Pa·sec) hydrogen brought about neither core-line shift nor change in the VB region except for the O2s and O2p regions attributable to a small amount of the oxygen contamination. This result is in agreement with the previous observation[127] that both the chemisorption and adsorption at room temperature result in no hydride formation detectable by the XPS.

An enlarged spectrum near the Fermi level of $Zr:H_{imp}$ is displayed in **Fig. 3.9** together with those of zirconium metal, ZrO_2 and the $ZrH_{1.64}$ sample. The (5-9)-eV photopeak observed for all samples is mainly due to the oxides. A small bump at 3.9 eV in **Fig. 3.8** for the $ZrH_{1.64}$ sample is probably from the Zr-H bond. Open circles represent a spectrum calculated for ZrH_2[81] by means of DV-Xα cluster method. Since damage by (5-10)-keV Ar^+-ion bombardment does not produce any new photopeaks in the VB region of the metal,

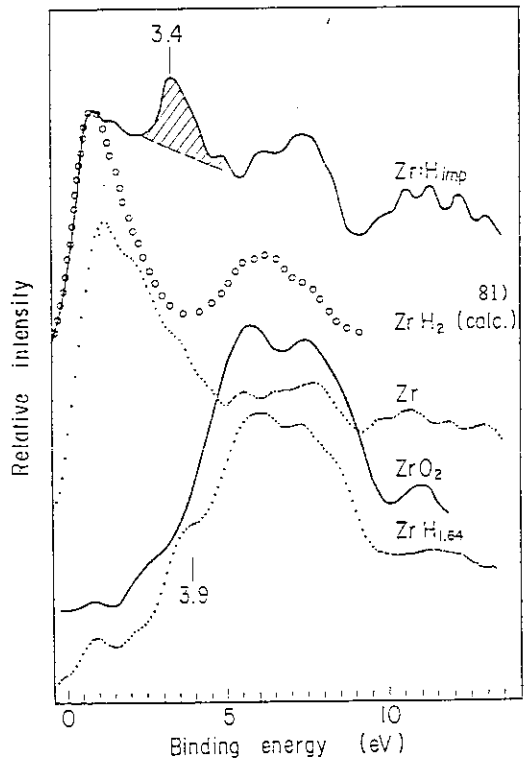

Fig. 3.8 VB XPS spectra of $Zr:H_{imp}$, Zr and oxygen-adsorbed Zr. The last sample has been exposed to oxygen until its O1s-to-Zr3d ratio becomes equivalent to that of $Zr:H_{imp}$.

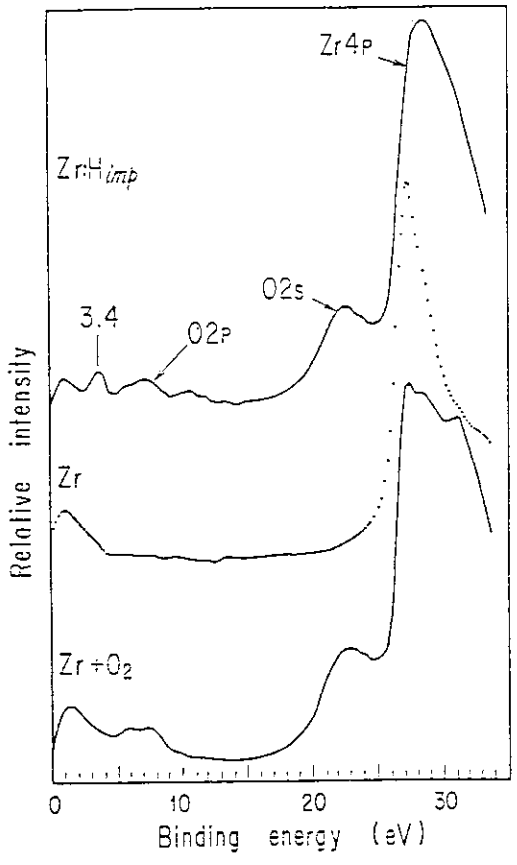

Fig. 3.9 Blowup of the XPS spectra near the Fermi level of $Zr:H_{imp}$, Zr, ZrO_2 and $ZrH_{1.64}$. The curve using open circles is spectrum calculated for ZrH_2, taken from ref. 81. The photopeak at 5-9 eV which is observed for all samples is mainly due to oxide(s). The small bump at ~3.9 eV for the $ZrH_{1.64}$ sample is probably from the Zr4d-H1s bond.

the photopeak indicated by hatching is attributed to the Zr-H bond. The peak position is in the lower binding energy, compared with the $ZrH_{1.64}$ sample whose main structure of the Zr-H bond would locate at 5-8 eV as previously observed for $ZrH_{1.65}$[86]. The appearence of the new photopeak seems to be associated with the difference in the sites occupied by hydrogen atoms. The experimental data obtained for the thermally synthesized hydrides are for the face-centered-tetragonal phase and the calculations for the dihydride with fluorite structure, while the present spectrum is for the hydrogen-ion implanted surface of zirconium metal.

A question may be raised as to why the new photopeak of the Zr-H bond appears in the spectrum for $Zr:H_{imp}$. One of the plausible reasons is as follows. The hydrogen bombardment may induce the radiation damage in the surface region. Consequently, the crystal lattice of the zirconium surface would become distorted. On the other hand, the DV-Xα calculations for a $[Zr_4H_8]$ cluster in ZrH_2 provide molecular-orbital (MO) levels which are sensitive to the bond length between zirconium and hydrogen atoms. Assuming that the bond length is contracted by 40%, the spectrum has a three peak-structures, i.e., 1.6, 3.3, and 5-8.5 eV below the Fermi level. The 3.3-eV peak is split off from the (4.5-8)-eV photopeak with the binding character of ZrH_2 shown in **Fig. 3.9**. Thus, it contains a considerable amount of the H1s character. As a result, the interaction between the Zr4d and H1s orbitals in the broad peak is diluted, though the strongest interaction still remains near 5.5 eV. The overall features described above are in reasonable agreement with the spectrum for $Zr:H_{imp}$ in **Fig. 3.9**.

3.3.6 VB-XPS spectra of niobium

Fig. 3.10 represents the VB spectra of the niobium compounds. Although the binding energy of the photopeak at 4.6 eV indicated by crosshatching is lower by at least 0.3 eV than the small bump of $NbH_{0.86}$ and also by 2 eV than the previous calculations for NbH_2[81,121,122], the peak is attributable to the Nb-H bond, as the reason discussed in detail in the previous section.

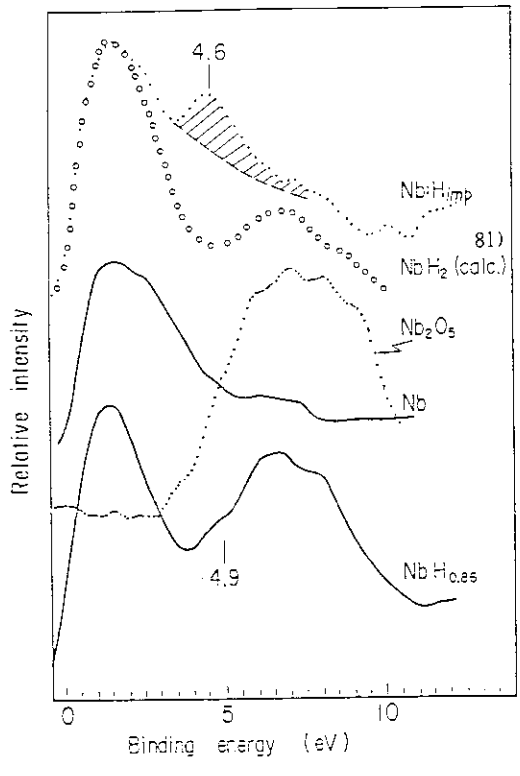

Fig. 3.10
Enlargement of the XPS spectra near the Fermi level of $Nb:H_{imp}$, Nb, Nb_2O_5 and $NbH_{0.86}$. The curve using the open circles is a spectrum calculated for NbH_2 taken from ref. 81. The small bump at ~4.9 eV for the $NbH_{0.86}$ sample is probably from the Nb4d-H1s bond.

3.3.7 VB-XPS spectra of chromium, nickel and molybdenum

The VB spectra of hydrogen-ion bombarded chromium, nickel and molybdenum were also taken, which are displayed in **Figs. 3.11-3.13** together with those of the corresponding

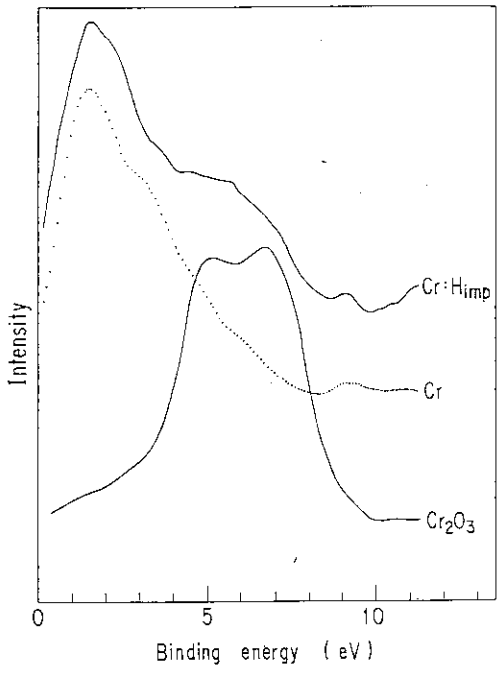

Fig. 3.11 VB XPS spectra of $Cr:H_{imp}$, Cr and Cr_2O_3.

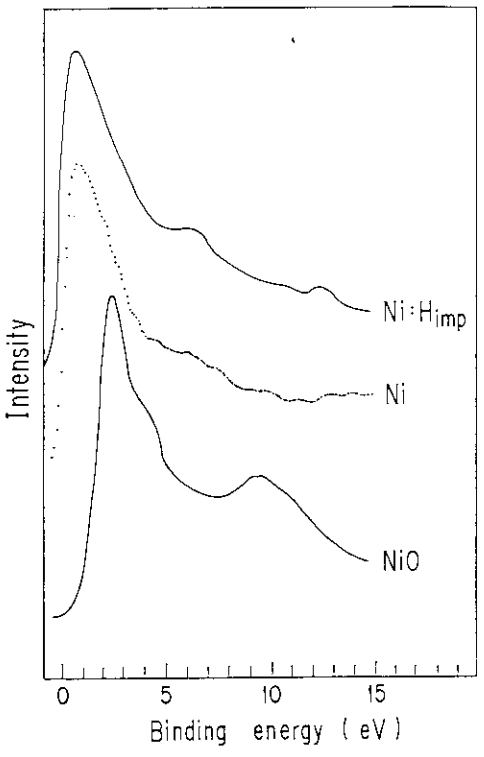

Fig. 3.12 VB XPS spectra of $Ni:H_{imp}$, Ni and NiO.

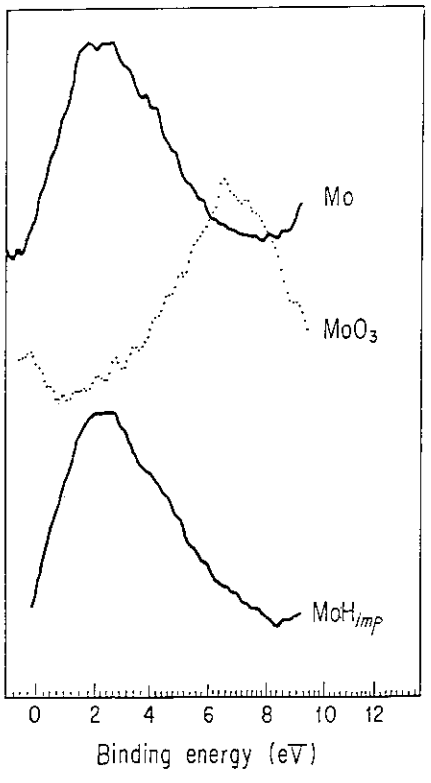

Fig. 3.13 VB XPS spectra of $Mo:H_{imp}$, Mo and MoO_3.

metals and oxides. In all spectra, slight overlapps of the (5-10)-eV peaks resulting from the adsorbed oxygen are observed after the hydrogen-ion bombardments. However, any distinct hydride-peaks which were observed in the scandium, titanium, vanadium, yttrium, zirconium and niobium systems did not appear at 3-5 eV up to the total fluence of 3×10^{18} atoms/cm^2. The results are in consistent with those of the core-line spectra shown in chapter 2. The results also support the consideration that the hydrogens implanted in these metals are trapped as atomic or molecular form in the metal lattice or defect without forming chemical bond with the targets.

3.3.8 Summary of chemical state of hydrogen implanted in transition metals

Fig. 3.14 summarizes the chemical shifts of the main XPS core-lines and the binding energies of the metal-H peaks in the VB spectra for the hydrogen-bombarded transition metals. The XPS data newly obtained for the hydrogen bombarded aluminium, graphite and silicon are added. In this figure, the classification of hydrides is also indicated[62,128]. The nature of the chemical bond of hydride can be classified into four groups as indicated in the figure. In the case of the transition metals, the formation of hydride is thermodynamically divided into two groups.

The first group is the metals belonging to groups IIIA (Sc, Y, La), IVA (Ti, Zr, Hf) and VA (V, Nb, Ta). These metals easily absorb hydrogen resulting in the formation of stable metallic hydrides such as MeH_2 (Me : metal), because the formation of the hydride is occurred through exothermic reaction. In the case of the ion-implantation process, the present XPS results indicate that the implantation of hydrogen also brings about the formation of the stoichiometric hydrides in the surface layer. Such similarity between thermal reaction and ion-implantation process is also true of the metals belonging to the second group.

The metals in VIA, VIIA and VIIIA groups except for palladium hardly react with

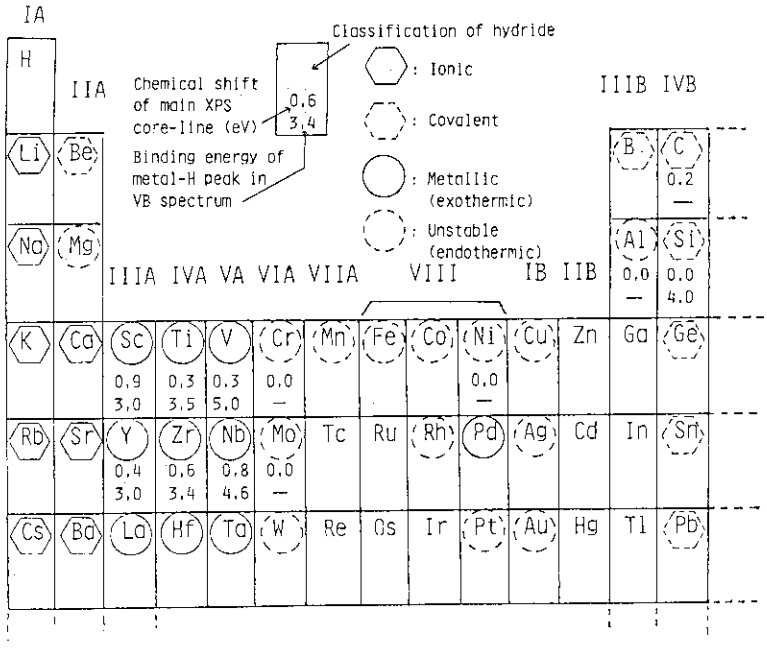

Fig. 3.14 Classification of hydrides represented in periodic table. The chemical shifts of main XPS core-lines ($2p_{3/2}$ for 3d metals, $3d_{5/2}$ for 4d metals) and binding energies of metal-H peaks in the VB spectra for Me:H_{imp} are also shown.

hydrogen, and there exist no stable hydride phases for these metals, because the introduction of hydrogen in these metals is endothermic. The hydrogen-ion bombardments on chromium, nickel and molybdenum also did not induce the formation of hydrides.

Such a similarity between thermal reaction and ion-implantation process will be applied to the estimation of the trapping state of the ion-implanted hydrogen in other metals.

3.4 Conclusions

1) The metal-H bonds in the VB spectra for $Sc:H_{imp}$, $Ti:H_{imp}$, $Y:H_{imp}$, $Zr:H_{imp}$ and $Nb:H_{imp}$ appear at 3.0 eV, 3.5 eV, 3.0 eV, 3.4 eV and 4.6 eV, respectively, all of which are lower by 1-3 eV than those calculated for MeH_2 (Me: metal) by DV-Xα cluster method. These discrepancies seem to be attributed to the crystal lattice distortion induced by the ion bombardments.

2) The V3d-H1s bonding levels in the VB spectra for $V:H_{imp}$ and $VH_{0.55}$ are observed at 5.0 eV and 4.2 eV, respectively. The binding energies of these new photopeaks are almost the same as those previously measured for $VH_{1.0}$ by UPS and those calculated for VH_2 by DV-Xα cluster method.

3) Hydrogen-ion bombardments on chromium, nickel and molybdenum did not bring about any new photopeaks in the VB region up to the total fluences of 3×10^{18} atoms/cm^2. The results are in consistent with the core-line spectra which also did not change after the hydrogen-ion bombardments.

4. Thermal release of hydrogen implanted in metals

4.1 Introduction

Hydrogen thermally absorbed in metals forms a solid solution (α-phase) in certain concentration range. In equilibrium condition, the concentration of hydrogen in metal is specified at certain temperature and pressure. Under the condition of constant temperature, hydrogen concentration is proportional to the square root of the pressure, which is called a Sieverts' law. While, under the condition of constant pressure, the effect of temperature on the concentration is divided into two cases. If the metal is highly reactive with hydrogen, the dissolution of hydrogen is exothermic. Therefore, the hydrogen in the metal is released with increasing the annealing temperature. On the contrary, dissolution of hydrogen is enhanced with increasing the annealing temperature if the dissolution of hydrogen is endothermic. Such behaviors of hydrogen in metals have been extensively investigated as pressure-composition isotherms at various temperatures[62,65].

On the other hand, if hydrogen is introduced into the metal by ion-implantation, strong non-equilibrium state of solid solution is produced. Neverthless the chemical states of implanted hydrogen are similar to those of the thermally absorbed one, which is described in chapters 2 and 3. The ion-implanted hydrogen, in addition, creates radiation damages such as Frenkel defects, point defect clusters and dislocation networks which affect the diffusion in the metal lattice. This means that the behavior of the ion-implanted hydrogen following the thermal annealing is assumed to be different from that of the thermally absorbed hydrogen. In fact, it has been observed that thermal diffusion of tritium which is recoil-implanted in UO_2 is different from that introduced with thermal process[129].

In this chapter, thermochemical behaviors of ion-implanted hydrogen from transition metals accompanied by the thermal annealing are investigated. The evolution of ion-implanted hydrogen is monitored by the XPS spectral changes. The results are compared with those of the thermally synthesized hydrides. Thermogravimetric analysis is also used for the investigation of dehydrogenation behavior of hydrides.

4.2 Experimental

The procedures and apparatus for the ion-bombardments and XPS measurements were the same as those described in chapter 2.

The hydrogen-implanted samples were isochronally heated in the analyzer chamber at various temperatures up to 610°C for 30 min, and the XPS spectra were measured after cooling to room temperature. The surface temperatures were measured with an infrared thermometer through a quartz window.

The TG analysis of the thermally synthesized hydrides was carried out with a Rigaku-denki Co. 8101A2 differential thermobalance in vacuum condition. Prior to the TG analysis, the surface of the hydride was polished with an emery paper in dry nitrogen atmosphere. The temperature of the furnace was raised at a rate of 5-10 °C/min.

4.3 Results and discussion

4.3.1 Thermal release of hydrogen implanted in titanium

The VB spectral changes for the hydrogen-implanted titanium Ti:H_{imp} following the isochronal annealing are shown in **Fig. 4.1**. To compare the thermal stability of the implanted hydrogen with that of the thermally absorbed one, the TG curve of the thermally synthesized hydride $TiH_{1.97}$ is displayed in the upper part of **Fig. 4.2**. The TG curve of $TiH_{1.97}$ shows that the hydrogen begins to be released at 400°C, and about 85% of total hydrogen is released at 550°C. On the other hand, the Ti3d-H1s peak at 3.5 eV in the VB spectra, seen in **Fig. 4.1**, survives even when annealed at 550°C. In addition, the binding energy of the $Ti2p_{3/2}$ line in the core-line spectrum for Ti:H_{imp} also remains unchanged up to 550°C. These results suggest that the hydrogen introduced in titanium by ion-implantation is hard to be released from the surface compared with that absorbed by thermal reaction.

Another spectral feature in **Fig. 4.1** is the slight growth of the photopeak corresponding to the Ti-H bond with the increase in the annealing temperature. The relative intensities of the hydride peak in the VB spectra are displayed in the lower part of **Fig. 4.2**. It should be noted that the projected range of 8-keV H_2^+ ions in titanium metal is less than ~30 nm[103], which is much deeper than the escape depth of photoelectron, i.e., ~1.2 nm[130]. Thus the growth of the hydride peak suggests the thermal diffusion of hydrogen atoms from the implanted layer to the metal surface detected by XPS.

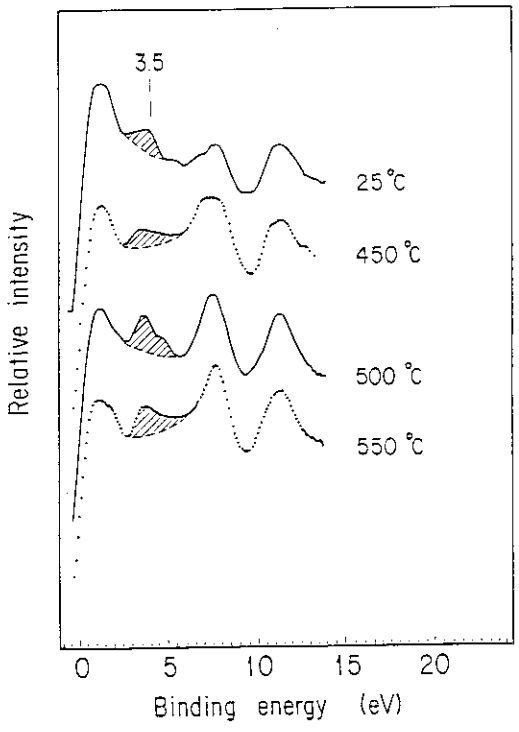

Fig. 4.1 Spectral changes in the VB region of Ti:H_{imp} following isochronal annealing for 30 min.

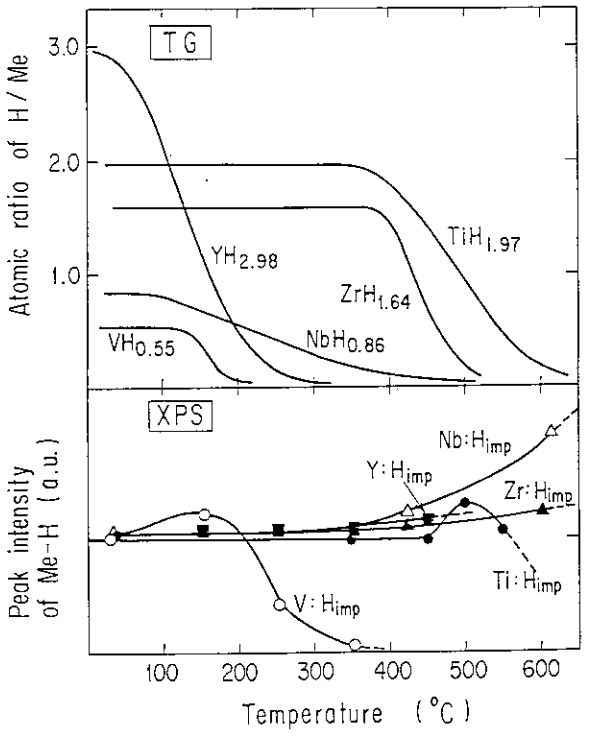

Fig. 4.2 TG curves of the thermally synthesized hydrides (upper side) and changes in the XPS intensities of the metal-H peaks for the hydrogen-ion implanted metals (lower side).

4.3.2 Thermal release of hydrogen implanted in vanadium

Figs. 4.3 and **4.4** indicate the VB-spectral changes of the isochronally annealed $V:H_{imp}$ and $VH_{0.55}$, respectively. The effect of the thermal annealing on the spectral pattern is a little different from that observed in the titanium system. The 5-keV peak in **Fig. 4.3** grew up until ~150°C due to the thermal diffusion of implanted hydrogen from bulk to surface. The peak, however, almost disappeared by annealing at 350°C. The observed mobility of hydrogen in vanadium is associated with large diffusion coefficient of hydrogen in vanadium compared with those in the other transition metals[131–133].

While the thermally synthesized hydride decomposes at 220°C, as indicated in **Fig. 4.2**, the incomplete release of ion-implanted hydrogen at 250°C suggests its lower diffusion in the surface layer than that of thermally absorbed hydrogen. The hydrogen evolution of $VH_{0.55}$ at lower temperature was confirmed also by the spectral changes. A photopeak at 4.2 eV, seen in **Fig. 4.4**, disappeared by annealing at 150°C.

After the dehydrogenation, the binding energies of the $V2p_{3/2}$ lines for both $V:H_{imp}$ and the $VH_{0.55}$ sample remained almost unchanged. These results suggest that the structure of the dehydrogenated metal is different from that of the metallic vanadium before the hydrogenation. Once the metal is hydrogenated, the inter-atomic distance of the V-V bond extends as a result of the permeation of hydrogen atoms into the metal lattice. On the other hand, the dehydrogenation may keep the enlarged metal lattice almost constant. The energy shift due to the lattice expansion has been observed in the case of the metal surfaces bombarded with Ar^+ ions[134–136]. In fact, the higher energy shift of the $V2p_{3/2}$ line for the Ar^+-ion bombarded vanadium has been observed for the mechanically scraped metal[134]. This energy shift is nearly equal to that for the dehydrogenated sample, which suggests that the inter-atomic distance of the V-V bond for the dehydrogenated vanadium metal is close to that for the Ar^+-ion bombarded vanadium metal.

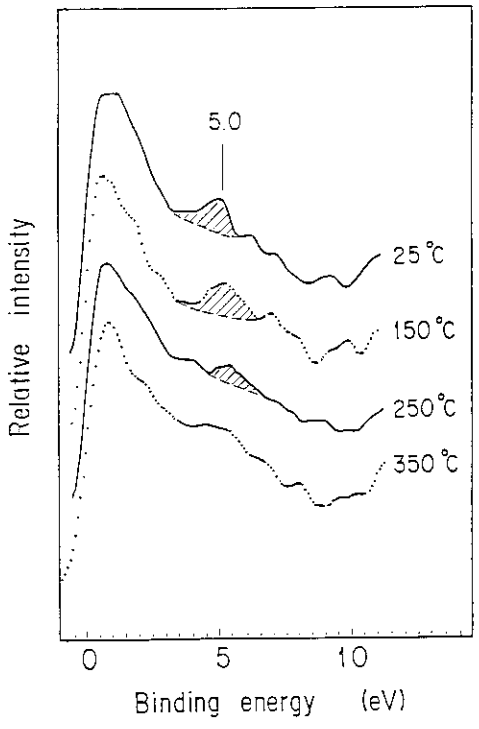

Fig. 4.3 Spectral changes in the VB region of $V:H_{imp}$ following isochronal annealing for 30 min.

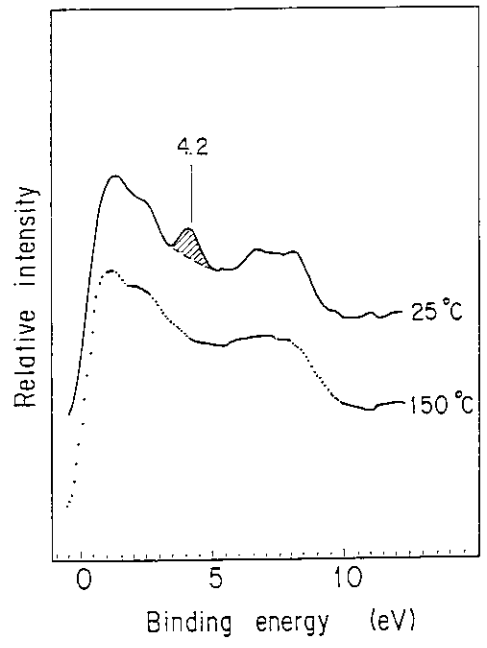

Fig. 4.4 Spectral changes in the VB region of $VH_{0.55}$ following isochronal annealing for 30 min.

4.3.3 Thermal release of hydrogen implanted in yttrium

The XPS spectral changes in the Y3d region for $Y:H_{imp}$ and the $YH_{2.98}$ sample are shown in **Figs. 4.5** and **4.6**, respectively. The VB spectral changes are also displayed in **Figs. 4.7** and **4.8**.

According to the result of the TG analysis, seen in **Fig. 4.2**, the thermally synthesized yttrium hydride $YH_{2.98}$ decomposes below 300°C, which is similar to the previous result[137]. In the Y3d spectra for $YH_{2.98}$ sample, the hydride peak at 154.6 eV disappears at 300°C, which is in consistent with the result of the TG analysis. The VB spectral changes in **Fig. 4.8** also shows the disappearence of the shoulder corresponding to the hydride at 3.0 eV. On the other hand, hydride peaks in the Y3d and VB spectra for $Y:H_{imp}$ survive up to 450°C. The result shows that the hydrogen introduced in yttrium by ion-implantation is hard to be released compared with that absorbed by thermal reaction, as observed in the other transition-metal systems such as $T:H_{imp}$ and $V:H_{imp}$. The fact is correlated with the ion-induce distortions of the lattice and the surface roughness. In the present experiment, the lattice of the yttrium metal would be distorted by the hydrogen-ion bombardment, and its surface sufficiently exposed to the hydrogen-ion may become amorphous. The damage layer thus obtained is considered to prevent the thermal diffusion of hydrogen at the metal surfaces.

4.3.4 Thermal release of hydrogen implanted in zirconium

Figs. 4.9 and **4.10** show the VB-spectral changes in the isochronal annealing for $Zr:H_{imp}$ and $ZrH_{1.64}$, respectively. One of the most noticeable results obtained is that the peak position of the Zr-H bond in $Zr:H_{imp}$ shifts from 3.4 eV to 3.6 eV, as seen in **Fig. 4.9**. Furthermore, its intensity grows on raising the annealing temperature. These observations are closely related to the partial recovery of the ion-induced distortions of the crystal lattice. On the other hand, the Zr-H bond of the $ZrH_{1.64}$ sample remains almost unchanged until at least 600°C. The disappearence of the (3-9)-eV spectrum at 1100°C in **Fig. 4.10** is due to the reduction of the oxide overlayer with the hydrogen evolved from the sample itself.

4.3.5 Thermal release of hydrogen implanted in niobium

The spectral changes in the Nb3d region of the $NbH_{0.86}$ sample following isochronal annealing are indicated in **Fig. 4.11**. The spectral patterns of the core-line for $Nb:H_{imp}$ are independent of annealing temperature up to 610°C. On the other hand, the Nb3d region for $NbH_{0.86}$ yields spectral changes as shown in **Fig. 4.11**. The 203.2-eV peak in question shifts by 0.4 eV at 420°C, where bulk niobium hydride evolves hydrogen gas. Furthermore, decreases in the oxide overlayer and spectral shifts to the lower binding-energy side are observed on raising the annealing temperature. This is due to thermal diffusion of hydrogen to the surface layer, resulting in the reduction of Nb_2O_5 on the $NbH_{0.86}$-sample surface. With annealing at 1100°C, the most prominent peak appears at 202.6 eV, as in the case of annealing at 475°C. Although the position of the new photopeak disagrees with that of niobium metal, this is supposed to be from the metallic phase which has vacancies from the detrapped hydrogen atoms. The chemical process,

$$Nb_2O_5 \xrightarrow{\Delta} NbH_x \xrightarrow{\Delta} Nb$$

was also reinforced by analyzing the changes in the O1s-to-Nb3d ratio. Thus the 203.2-eV peaks for $NbH_{0.86}$ and also for $Nb:H_{imp}$ are attributed to the $Nb3d_{5/2}$ line of the hydride.

Figs. 4.12 and **4.13** represent the VB spectral changes for $Nb:H_{imp}$ and $NbH_{0.86}$, respectively. A photopeak at 4.6 eV indicated by crosshatching in **Fig. 4.13** is attributable to the Nb-H bond. The peak becomes sharp with an increase in the annealing temperature.

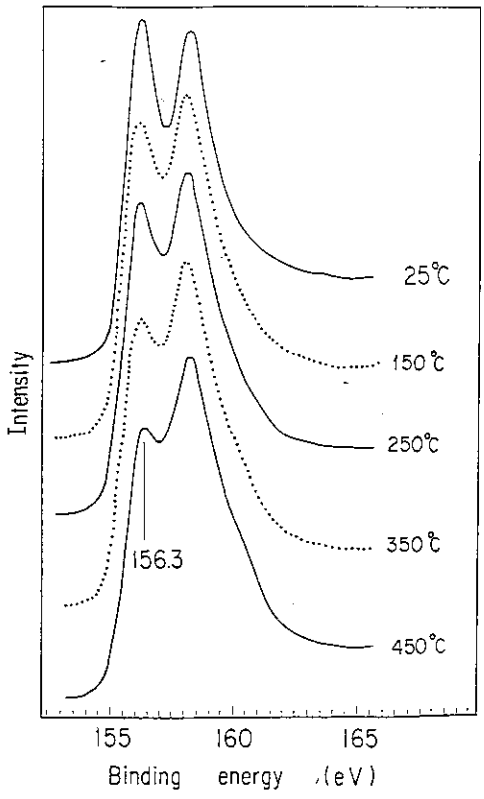

Fig. 4.5 Spectral changes in the Y3d region of $Y:H_{imp}$ following isochronal annealing for 30 min.

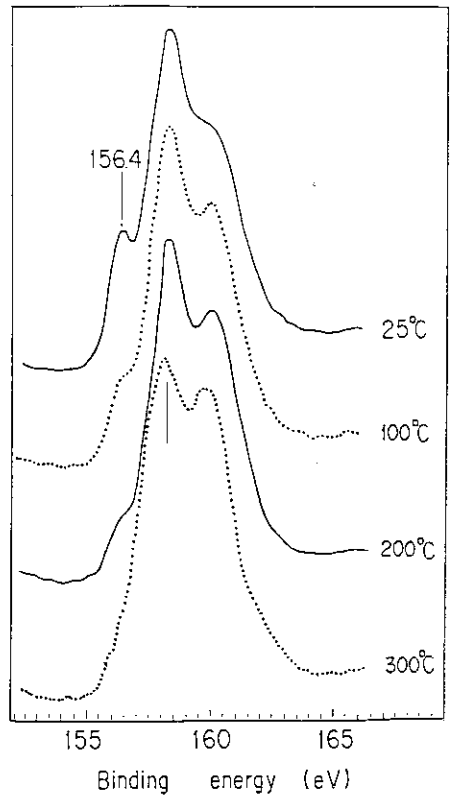

Fig. 4.6 Spectral changes in the Y3d region of the $YH_{2.98}$ sample following isochronal annealing for 30 min.

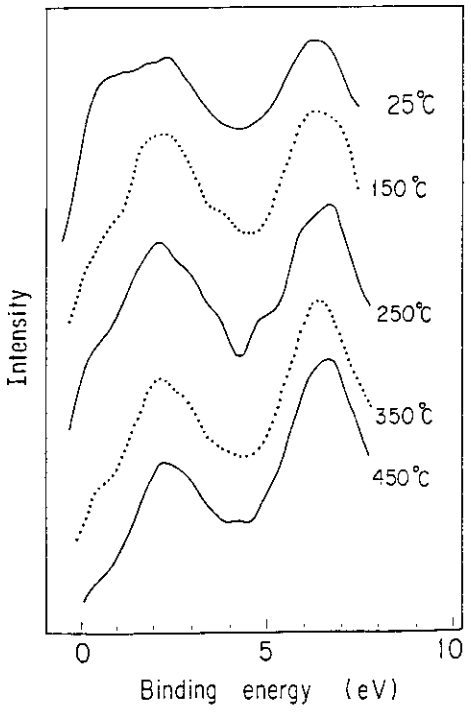

Fig. 4.7 Spectral changes in the VB region of $Y:H_{imp}$ following isochronal annealing for 30 min.

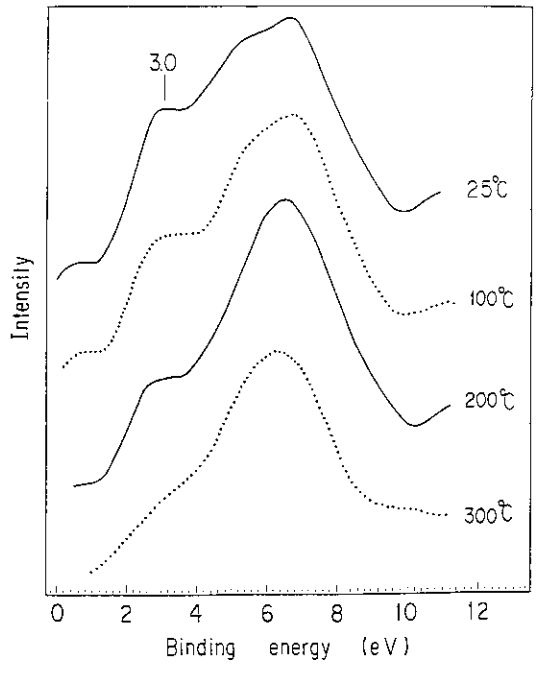

Fig. 4.8 Spectral changes in the VB region of the $YH_{2.98}$ sample following isochronal annealing for 30 min.

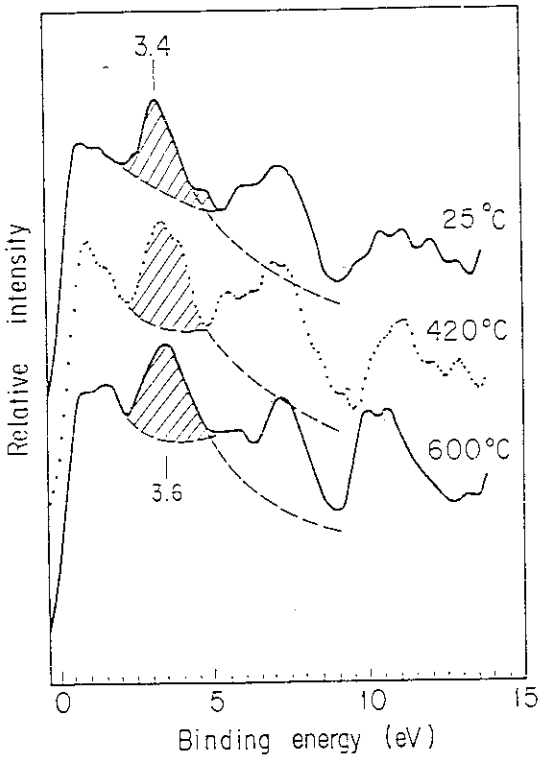

Fig. 4.9 Spectral changes in the VB region of $Zr{:}H_{imp}$ following isochronal annealing at various temperatures for 30 min.

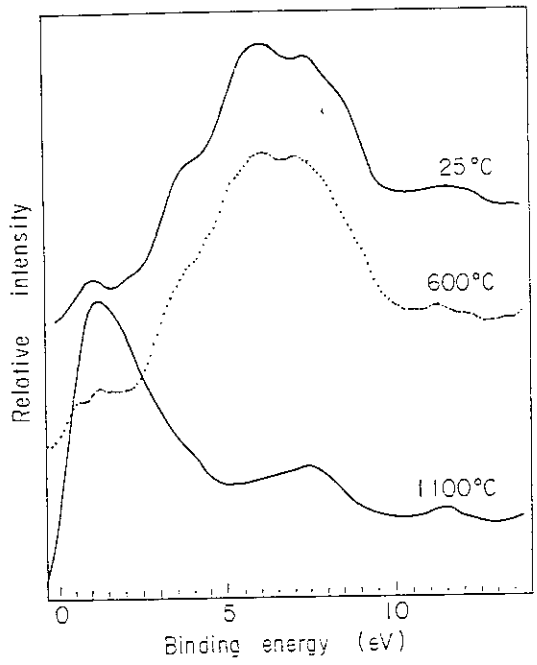

Fig. 4.10 Spectral changes in the VB region of the $ZrH_{1.64}$ sample following isochronal annealing at various temperatures for 30 min.

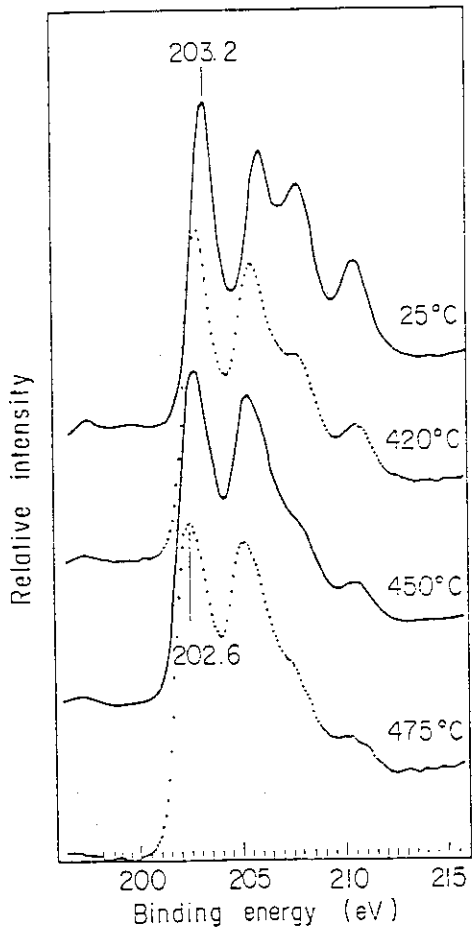

Fig. 4.11
Spectral changes in the Nb3d region of the $NbH_{0.86}$ sample following isochronal annealing at various temperatures for 30 min.

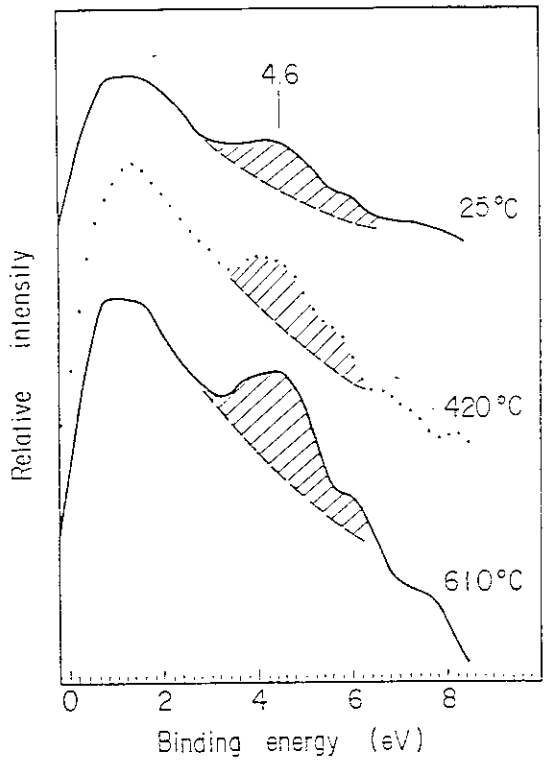

Fig. 4.12 Spectral changes in the VB region of Nb:H_{imp} following isochronal annealing at various temperatures for 30 min.

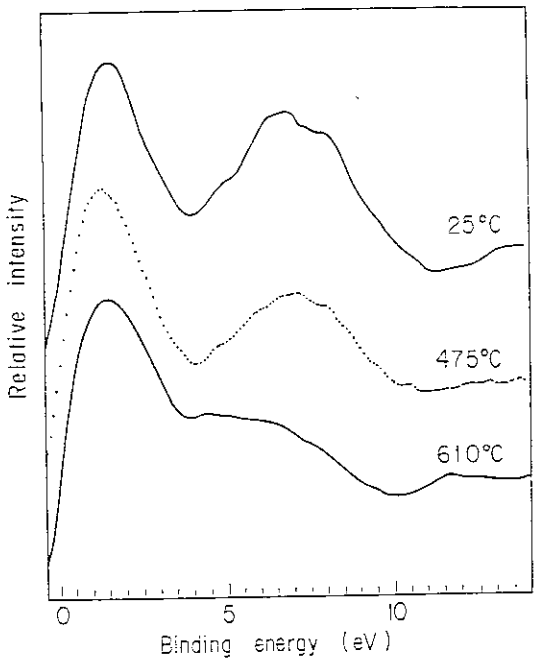

Fig. 4.13 Spectral changes in the VB region of the $NbH_{0.86}$ sample following isochronal annealing at various temperatures for 30 min.

On the contrary, the 4.9-eV bump of the Nb-H bond and (5-9)-eV peak of the oxide overlayer of the $NbH_{0.86}$ sample in **Fig. 4.13** decrease on raising the annealing temperature, which is in consistent with the annealing behavior of the core-line shift (**Fig. 4.11**). Considering that the peak positions of both the core-line and Nb-H bond in Nb:H_{imp} remain unchanged, recovery of the crystal structure seems to be incomplete even at 600°C. If the crystalline distortions are completely removed, the peak positions would shift slightly (0.3 eV) toward the higher-energy side as observed for Zr:H_{imp}.

4.4 Conclusions

1) The photopeak corresponding to the Ti3d-H1s bond for Ti:H_{imp} grows up on raising the annealing temperature up to 550°C, due to the thermal diffusion of the implanted hydrogen from bulk to surface. In the case of the vanadium compounds, the peak of the V3d-H1s disappears at 350°C for V:H_{imp} and at 150°C for $VH_{0.55}$, respectively, reflecting the high diffusibility of hydrogen in vanadium.

2) While thermally synthesized yttrium hydride completely decomposes at 300°C, the hydrogen implanted in the metal is held up to 450°C. The fact that the temperature of the thermal release of ion-implanted hydrogen from the metal is higher than that of thermally absorbed one is associated with the fact that the amorphous layer produced by the ion bombardment prevents the thermal diffusion of hydrogen at the metal surface.

3) In heating to 610°C, the core-line energies for both Zr:H_{imp} and Nb:H_{imp} remain unchanged, while those for the thermally synthesized $NbH_{0.86}$ shift to the lower binding-energy side attributable to the metallic state. Furthermore, the photopeaks of the metal4d-H1s bond grow on raising the annealing temperature to at least 600°C. The anomalies observed are

probably due to the lattice distortions caused by the ion-induced damage of the surface layers and their partial recovery in the annealing.

5. Application of X-ray-induced Auger electron spectroscopy to state analyses of hydrogen implanted in metals

5.1 Introduction

In chapters 2 and 3, an XPS was applied to the identification of the chemical states of the ion-implanted hydrogen in metals. The formation of the hydride layers was confirmed by both the chemical shifts of the core-line photopeaks and the photopeaks of the metal-H bonds in the VB spectra.

An alternative method of identifying surface chemical states is X-ray-induced Auger electron spectroscopy (XAES). In the case of 4d transition metals, the Auger electrons have a kinetic energy of 100-300 eV (being surface sensitive compared with X-ray-induced photoelectrons). Thus, the XAES is superior to XPS regarding resolution of detection depth. Using soft X-rays as an excitation source, the method has another superiority that it is less destructive than ordinary AES induced by electron beams. In addition, it has been reported that chemical shifts of Auger signals are often larger than those of core-line photopeaks[138-140]. Wagner et al. summarized the chemical shifts obtained by XAES using both Auger parameters[94,141] and two-dimensional plots[142-146] for many transition-metal compounds.

In this chapter, XAES is applied to state analyses of hydrogen implanted in 4d transition metals such as yttrium, zirconium, niobium and molybdenum. The spectral features and magnitudes of the Auger chemical shifts are compared with those of the $3d_{5/2}$ lines obtained by XPS. The XAES spectra obtained for related oxides and thermally synthesized hydrides are also presented.

5.2 Experimental

All samples used and condition of the hydrogen-ion bombardments employed are the same as those described in chapter 2. The XAES spectra were obtained simultaneously with XPS under the same condition as that described in chapter 2. Accumulation of the XAES data of the metal $M_{4,5}N_{2,3}V$ region required more than 80 min to obtain good S/N ratio.

5.3 Results

The XAES spectra of $Y(M_{4,5}N_{2,3}V)$ are shown in **Fig. 5.1**, and the kinetic energies of the Auger electrons are summarized in **Table 5.1**. The weak intensities of the Auger peaks are correlated with the small probability of Auger transition of yttrium, because it has only one electron in the 4d sub-shell from which the $M_{4,5}N_{2,3}V$ Auger signal is generated. Neverthless, an Auger peak is clearly observed at E_k =123.3 eV for the spectrum of the hydrogen-implanted sample $Y:H_{imp}$. In the spectrum for the thermally synthesized hydride $YH_{2.98}$, two peaks are observed. The lower-energy peak is attributed to the contribution from the surface oxide. The higher-energy peak at E_k =123.3, which disappears by heating to 300°C, is due to the hydride. The peak of $Y:H_{imp}$ shifts to the lower kinetic energy by 1.0 eV from that of yttrium metal (E_k =124.3 eV), which is in consistent with the hydride

peak. It should be noted that the $Y3d_{5/2}$ line for $Y:H_{imp}$ lacates at the binding energy higher only by 0.4 eV than that of yttrium metal, as shown in chapter 2.

The XAES spectra of $Zr(M_{4,5}N_{2,3}V)$ are presented in **Fig. 5.2**, and the kinetic energies of the Auger peaks and the chemical shifts of the $3d_{5/2}$ lines are also listed in **Table 5.1**. The Auger peaks of $Zr:H_{imp}$ (E_k =145.3 eV) shifts to the lower kinetic energy by 3.3 eV from that of zirconium metal. The separation energy is much larger than the corresponding XPS chemical shift of the $3d_{5/2}$ line (E_b =179.6 eV), i.e., 0.6 eV. Thus in some cases, XAES is more effective in identifying surface chemical state of hydrogen in zirconium than XPS.

To examine the surface sensitivity of XAES in chemical state analysis, an XAES spectrum was also taken for the thermally synthesized hydride $ZrH_{1.64}$. The spectral feature obtained is almost equal to that of ZrO_2, as seen in **Fig. 5.2(c)**. The result indicates that $ZrH_{1.64}$ surface detected by the XAES (less than 0.6 nm from the surface)[130] is completely covered with ZrO_2, whereas the Zr3d region shows the presence of zirconium hydride at E_b =179.6 eV (**Fig. 2.14**)[147].

To identify the chemical state more clearly, the effect of 30-min isochronal annealing on the XAES spectrum was investigated. The peak position of the $Zr(M_{4,5}N_{2,3}V)$ Auger line for $ZrH_{1.64}$ remained unchanged up to 610°C. However, it returned to the same position as the metallic state after heating to 1100°C. This is due to the dehydrogenation of $ZrH_{1.64}$.

Similar trends were also observed for the niobium system. The XAES spectra of $Nb(M_{4,5}N_{2,3}V)$ are shown in **Fig. 5.3**. The Auger peak of $Nb:H_{imp}$ shifts to the lower kinetic energy by 2.2 eV from that of niobium metal (E_k =167.8 eV). The separation energy is also much larger than as XPS shift of the $Nb3d_{5/2}$ line (E_b =203.2 eV), i.e., 0.8 eV.

The XAES spectrum shown in **Fig. 5.3(d)** for the thermally synthesized $NbH_{0.86}$ indicates that the sample surface detected by XAES is also completely covered with Nb_2O_5. On the other hand, the $Nb3d_{5/2}$ line corresponding to the Nb-H bond has been clearly observed at 203.2 eV in the XPS spectrum of $NbH_{0.86}$ (**Fig. 2.15**). When the hydride sample was heated to 550°C, the peak at 162.0 eV shifted to the higher kinetic energy by 2.0 eV. This is associated with the thermal diffusion of hydrogen from bulk to surface, resulting in a reduction in the oxide overlayer of Nb_2O_5.

Surface chemical change was also examined by the XAES for hydrogen implanted molybdenum. However, no appreciable changes in the spectral pattern were observed for $Mo(M_{4,5}N_{2,3}V)$ Auger line, as seen in **Fig. 5.4**. This observation suggests that the hydrogen ions do not interact chemically with molybdenum under the present experimental condition. The results are consistent with a fact that molybdenum metal does not interact with hydrogen and its hydride cannot become stable at ambient temperature[62].

5.4 Discussion

On the basis of the results given in **Table 5.1**, it is concluded that the chemical shifts in the XAES signals for the 4d transition-metal hydrides are larger than those of the corresponding $3d_{5/2}$ lines. Hence, the Auger signals in XPS spectra are more effective to elucidate the chemical state of hydrogen in these metals than core-line photopeaks.

More general expression available for chemical state analysis is to use the Auger parameter α[94], because the charging effect during the measurements can be cancelled and the correction of the work function becomes unnecessary. The magnitude of α is defined as

$$\alpha = E_k + E_p - h\nu \quad \cdots\cdots (1)$$

where E_k and E_p are the kinetic energy of the Auger electron and the binding energy of the photoelectron, respectively. The Auger parameters obtained and their shifts $\Delta\alpha$ from

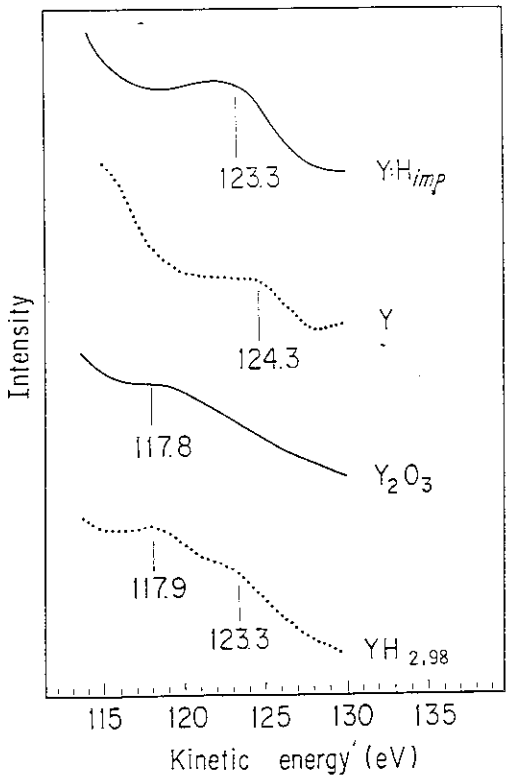

Fig. 5.1 X-ray-induced $M_{4,5}N_{2,3}V$ Auger spectra of $Y:H_{imp}$, Y, Y_2O_3 and $YH_{2.98}$.

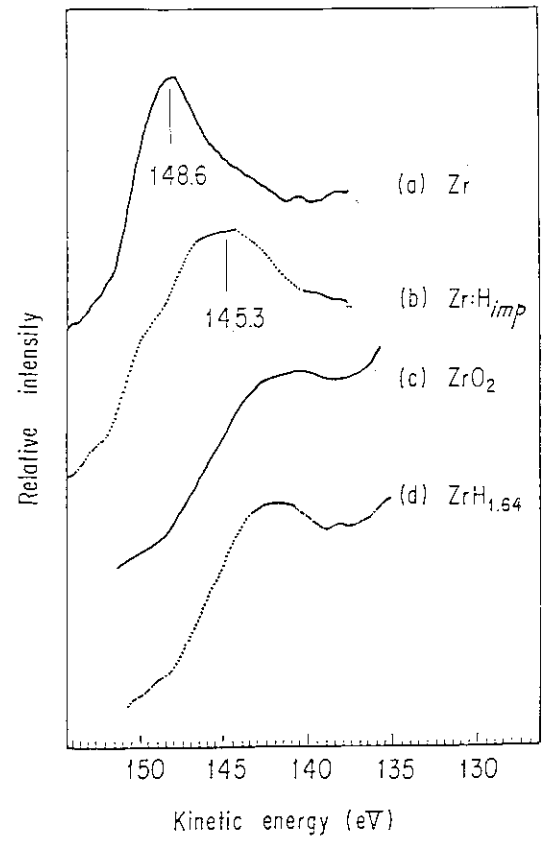

Fig. 5.2 X-ray-induced $M_{4,5}N_{2,3}V$ Auger spectra of Zr, $Zr:H_{imp}$, ZrO_2 and $ZrH_{1.64}$.

Table 5.1 Kinetic energies of $M_{4,5}N_{2,3}V$ Auger electrons (E_k), binding energies of $3d_{5/2}$ lines (E_b), and Auger parameters (α)

Sample	E_k (eV)	Auger Chemical Shift (eV)	E_b (eV)	$3d_{5/2}$ Chemical Shift (eV)	α (eV)	$\Delta\alpha$ (eV)
Y	124.3	–	155.9	–	−973.4	–
$Y:H_{imp}$	123.3	1.0	156.3	0.4	−974.0	0.6
Y_2O_3	117.8	6.5	158.6	2.7	−977.2	3.8
Zr	148.6	–	179.0	–	−926.0	–
$Zr:H_{imp}$	145.3	3.3	179.6	0.6	−928.7	2.7
ZrO_2	141.9	6.7	183.3	4.3	−928.4	2.4
Nb	167.8	–	202.4	–	−883.4	–
$Nb:H_{imp}$	165.6	2.2	203.2	0.8	−884.8	1.4
Nb_2O_5	161.6	6.2	208.1	5.7	−883.9	0.5

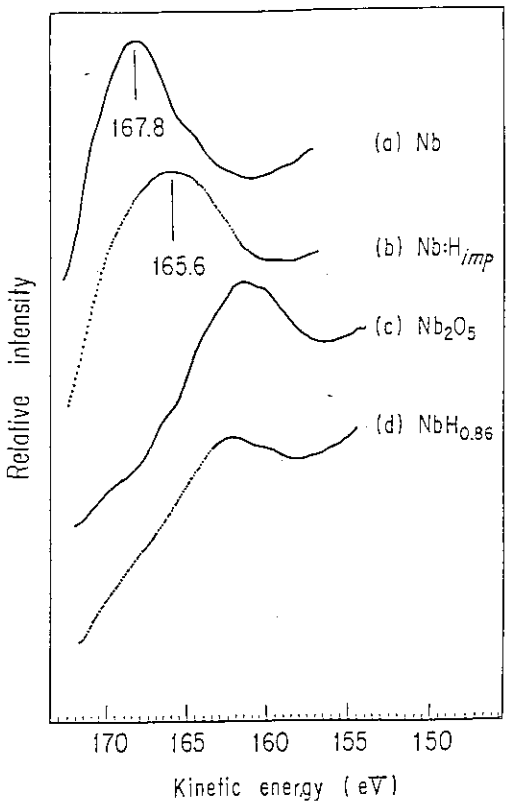

Fig. 5.3 X-ray-induced $M_{4,5}N_{2,3}V$ Auger spectra of Nb, Nb:H_{imp}, Nb_2O_5 and $NbH_{0.86}$.

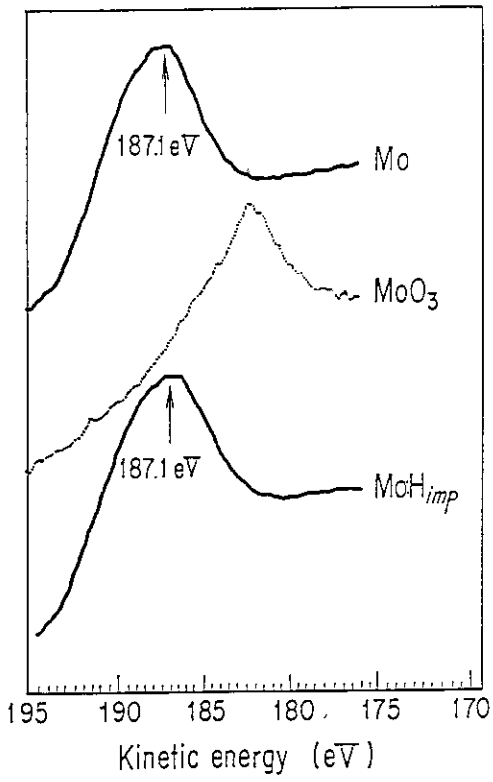

Fig. 5.4 X-ray-induced $M_{4,5}N_{2,3}V$ Auger spectra of Mo, MoO_3 and Mo:H_{imp}.

the metallic states are given in the last two columns of **Table 5.1**.

The kinetic-energy shift of Auger electron ΔE_k measured from the metallic state is correlated with that of the core-lines as follows[148)]

$$\Delta E_k(XYZ) = \Delta E_b(X) - \Delta E_b(Y) - \Delta E_b(Z) + \Delta R_{m\to c} \quad \cdots\cdots (2)$$

where X, Y and Z refer the electron shell relevant to the Auger transition, ΔE_b the binding-energy shift of the core-line electron, and ΔR the shift of the extra-atomic relaxation energy. The notation "m→c" represents that the energy shift is measured from the metallic state to the compound. The value of ΔR is correlated with a reduction in the binding energy of the emitted electron due to the rearrangement of whole electrons. In the present case, the relaxation energy is caused by the polarization of the surrounding atoms, which is induced by the positive hole in the center atom[149)].

All of the energy shifts in eq. (2) are measured from the metallic states. When the binding energy of the core-line electron in Z shell is used in calculating the Auger parameter, $\Delta\alpha$ is represented as

$$\begin{aligned}\Delta\alpha &= \Delta E_k(XYZ) + \Delta E_b(Z) \\ &= \Delta E_b(X) - \Delta E_b(Y) - \Delta R_{m\to c} \quad \cdots\cdots (3).\end{aligned}$$

If X and Y are inner shells, it is general that $\Delta E_b(X)$ is nearly equal to $\Delta E_b(Y)$, that is,

$$\Delta\alpha \simeq \Delta R_{m\to c} \quad \cdots\cdots (4).$$

Since the extra-atomic relaxation energy is the lowest for free atom, higher for compounds, and the highest for metallic state, the equation (4) can be rewritten as follows

$$\Delta\alpha \simeq \Delta R_{m\to a} - \Delta R_{c\to a} \quad \cdots\cdots (5)$$

where $\Delta R_{m\to a}$ and $\Delta R_{c\to a}$ are the shifts of the extra-atomic relaxation energies for metals and compounds, respectively.

Thus using eq. (5), we can obtain $\Delta R_{a\to c}$ for the hydrides and oxides of yttrium, zirconium and niobium. The experimental values of $\Delta R_{m\to a}$ for the present metals have not been reported yet. Thus we use the theoretically calculated values by Larkins[150] as $\Delta R_{m\to a}$ in the calculations of $\Delta R_{a\to c}$. The results are summarized in **Table 5.2**.

Table 5.2 Shifts of extra-atomic relaxation energies ΔR for Y, Zr, Nb and Mo, their hydrides obtained by ion-implantation, and their oxides. The expression $X\to Y$ represents the value of Y state measured from X state. The notation a, m, h and o are isolated atomic state, metal, hydride and oxide, respectively. The values of $\Delta R_{a\to m}$ are taken from ref. 150.

element	$\Delta R_{a\to m}$(eV)	$\Delta R_{m\to h}$(eV)	$\Delta R_{a\to h}$(eV)	$\Delta R_{m\to o}$(eV)	$\Delta R_{a\to o}$(eV)
Y	6.4	0.6	5.8	3.8	2.6
Zr	6.3	2.7	3.6	2.4	3.9
Nb	6.6	1.4	5.2	0.5	6.1
Mo	7.5	–	–	0.3	7.2

The calculated values for the yttrium compounds show that ΔR measured from isolated atomic state for $Y:H_{imp}$ is much larger than that for Y_2O_3. It has been reported that the extra-atomic relaxation energy, being related with the surrounding atoms, is almost proportional to the polarizability of the compounds[94]. Regarding the metal-O bond, we obtain the following order for the polarizabilities

$$Y\text{-}O < Zr\text{-}O < Nb\text{-}O < Mo\text{-}O.$$

Thus the Mo-O bond is the most poralized among the oxides examined. On the other hand, there exist no appreciable regularity for the poralizabilities in the metal-H system. Whereas the Y-H bond seems to be the most poralized among the present hydrides in contrast to the metal-O system. The magnitude of the porilazability for Y-H bond is even larger than that of the Y-O bond.

5.5 Conclusions

1) The chemical shifts of the X-ray-induced $M_{4,5}N_{2,3}V$ Auger peaks for the 8-keV hydrogen-ion implanted yttrium, zirconium and niobium metals are 1.0 eV, 3.3 eV and 2.2 eV, respectively. All of them are larger than those of the corresponding $3d_{5/2}$ lines in the XPS spectra. Thus the XAES revealed to be useful method for the state analyses of hydrogen in 4d transition metals.

2) Hydrogen-ion bombarded molybdenum metal showed no appreciable changes in the spectral features of the Auger lines, which is consistent with a fact that molybdenum metal hardly reacts with hydrogen by thermal process.

3) The extra-atomic relaxation energy measured from the isolated atomic state is larger for $Y:H_{imp}$ than that for Y_2O_3, which suggests a large polarizability of the Y-H bond compared with that of the Y-O bond.

6. Surface chemical changes of SiC, Si_3N_4 and SiO_2 by hydrogen-ion bombardments

6.1 Introduction

The interaction between energetic particles and the first-wall material used in fusion-reactor of tokamak type produces plasma-impurities by processes such as sputtering, blistering and evaporation[66,151]. It has been pointed out that small amounts of low-Z (Z: atomic number) impurities such as carbon, nitrogen, oxygen and silicon produced by above processes can be permissible in plasma, whereas the bremsstrahlung of high-Z impurities prevents the plasma ignition[152]. In these aspects, low-Z refractory materials such as graphite, silicon carbide (SiC) and silicon nitride (Si_3N_4) have been proposed for first-wall materials of tokamak fusion-reactor.

Thus, many workers have recently investigated the effects of energetic particles, especially hydrogen isotope ions, on graphite[153–155] and SiC[153,154,156–159] in relation to the recycling of hydrogen isotopes and the evaluation of surface damages. In these works, it has been observed that the low-energy hydrogen bombardments on SiC surface create a silicon-depleted layer in the near surface region[156,158]. With respect to the chemical state of hydrogen-bombarded surfaces, few works have been so far carried out although the re-emission behavior of hydrogen strongly depends on their trapped state in the material.

In this chapter, the changes in the surface chemical states of SiC, Si_3N_4 and SiO_2 by the bombarding H_2^+ ions are investigated by means of an XPS. For comparison, bombardments are also carried out on pure graphite and silicon. An AES as well as XPS is employed to evaluate the changes in the near surface composition.

6.2 Experimental

6.2.1 Materials

The SiC and Si_3N_4 samples were of ~100 μm thickness deposited on graphite substrate by chemical-vapor-deposition (CVD) method in Toshiba Ceramics Co. Ltd. The SiO_2 sample was pure quartz of ~300 μm thickness. These three samples were polished into mirrorlike plane by use of 1/4-μ diamond paste and mounted on sample holders using silver paste.

Highly pure graphite and silicon single crystal were used as reference materials in the examination of the chemical-state changes induced by the hydrogen-ion bombardments. The oxide overlayer on the Si(100) plane was removed by use of a mixed solution of nitric and fluoric acids.

Sample surfaces were chemically cleaned by heating the holder with the specimen at 350°C for 3 hours under a pressure of 10^{-7} Pa, and then Ar^+-ion etching was performed at room temperature for the elimination of the carbon- and/or oxygen-containing adsorbates. Exposure to a faint beam (ca. 4 $\mu A/cm^2$) of 8-keV Ar^+-ion proved to be effective for this purpose, and it caused no compositional changes in the surface regions of the samples themselves except for SiO_2.

6.2.2 Ion bombardments and measurements

The AES measurements were carried out using the 5-keV electron beams from a tungsten

hairpin-filament attached to a V.G.ESCALAB-5 spectrometer. For the quantitative evaluation of the C/Si ratio, the C(KLL, 260 eV) and Si(LVV, 75 eV) Auger signals were monitored after every bombardment. Details of the XPS measurements and hydrogen-ion bombardments were the same as those described in chapter 2.

6.3 Results

6.3.1 Hydrogen-ion bombarded SiC surface

Fig. 6.1 shows the variations of the compositional C/Si ratios in the near surface region of the SiC sample as functions of the hydrogen and Ar^+-ion fluences. The C/Si ratios determined by both AES and XPS methods increased with increasing the hydrogen-ion fluence and showed a trend of an increase even over a fluence of 2×10^{18} atoms/cm^2.

The XPS spectra in the C1s region for the SiC and graphite samples before and after the hydrogen-ion bombardments are displayed in **Figs. 6.2** and **6.3**, respectively. After the bombardments, the C1s lines of the SiC and graphite samples shifted to the higher binding-energies by 0.3 eV and 0.2 eV, respectively. The XPS spectra in the Si2p and Si2s regions were also measured for the SiC sample, but any appreciable changes in the spectral patterns were not observed up to the total fluence of 3×10^{18} atoms/cm^2.

6.3.2 Hydrogen-ion bombarded Si_3N_4 surface

The variation of the N/Si ratios in the near surface region of the ion-bombarded Si_3N_4 sample is shown in **Fig. 6.4** as functions of the hydrogen and Ar^+-ion fluences. In contrast to the SiC sample, the hydrogen-ion bombardments made the near surface of the Si_3N_4 sample silicon abundant. The quantitative analysis by XPS showed that the N/Si ratios varied from the bulk composition of 1.33 to 1.0 at a fluence of 5.3×10^{18} atoms/cm^2. The silicon-rich layer on the Si_3N_4 is removed by the Ar^+-ion etching, as the case of the SiC sample shown in **Fig. 6.1**. The formation of the silicon-rich layer seems to be correlated with a chemical reaction occurring in the near surface region of the Si_3N_4 sample.

The Si2p and VB-XPS spectra of the Si_3N_4 sample are displayed in **Figs. 6.5** and **6.6**, respectively. The spectral pattern in the Si2p region for the hydrogen-ion bombarded Si_3N_4

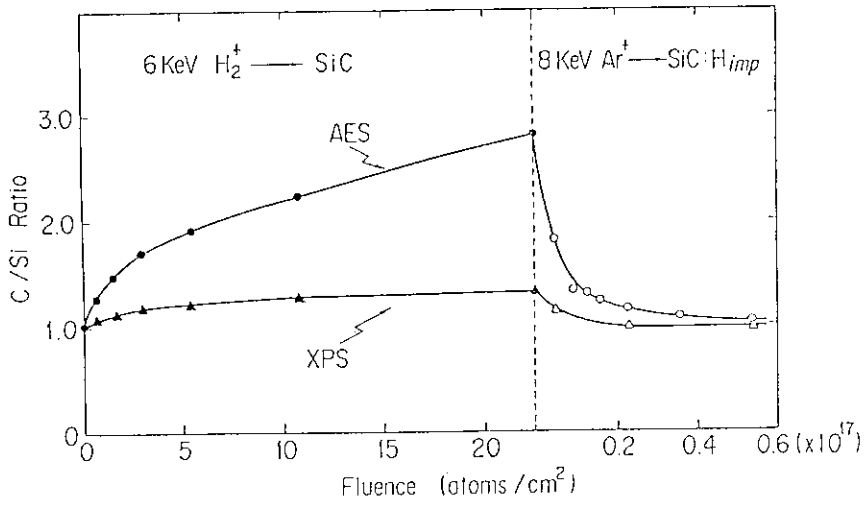

Fig. 6.1 Changes in C/Si ratios of SiC as functions of hydrogen-ion and Ar^+-ion fluences. The AES data were determined from signal ratios of Si(LVV, 75 eV)/C(KLL, 260 eV).

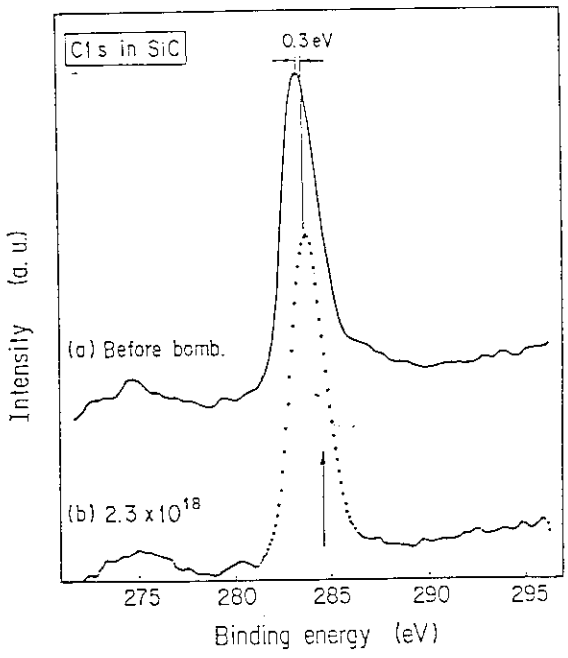

Fig. 6.2 C1s XPS spectra of SiC before and after 6-keV H_2^+-ion bombardments. An arrow indicates position of C1s line for graphite target bombarded with H_2^+ ions, taken from **Fig. 6.3**.

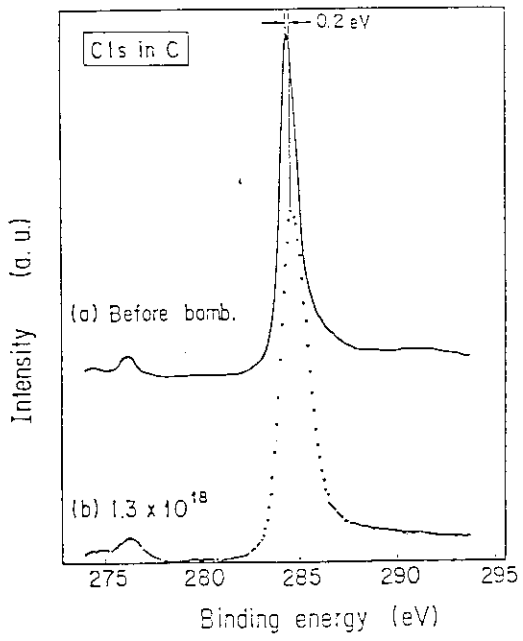

Fig. 6.3 C1s XPS spectra of graphite before and after 6-keV H_2^+-ion bombardments.

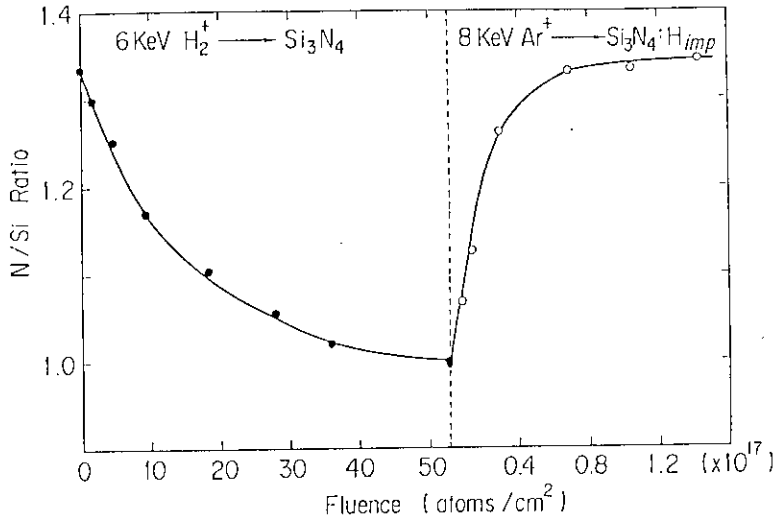

Fig. 6.4 Changes in N/Si ratios of Si_3N_4 as functions of hydrogen-ion and Ar^+-ion fluences.

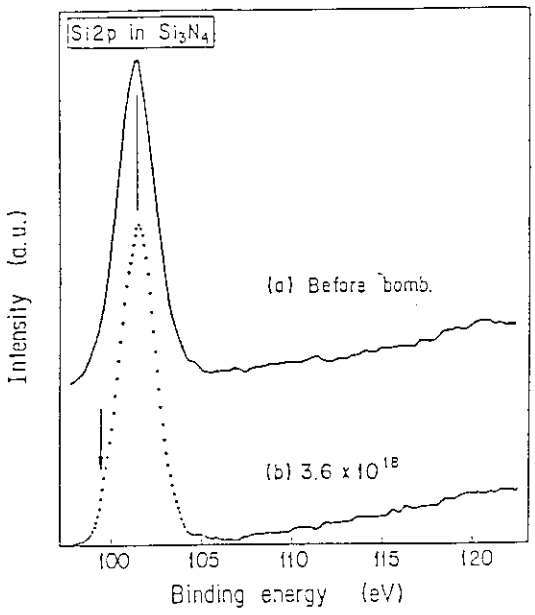

Fig. 6.5 Si2p XPS spectra of Si_3N_4 before and after 6-keV H_2^+-ion bombardments. An arrow indicates position of Si2p line for Si target bombarded with H_2^+ ions.

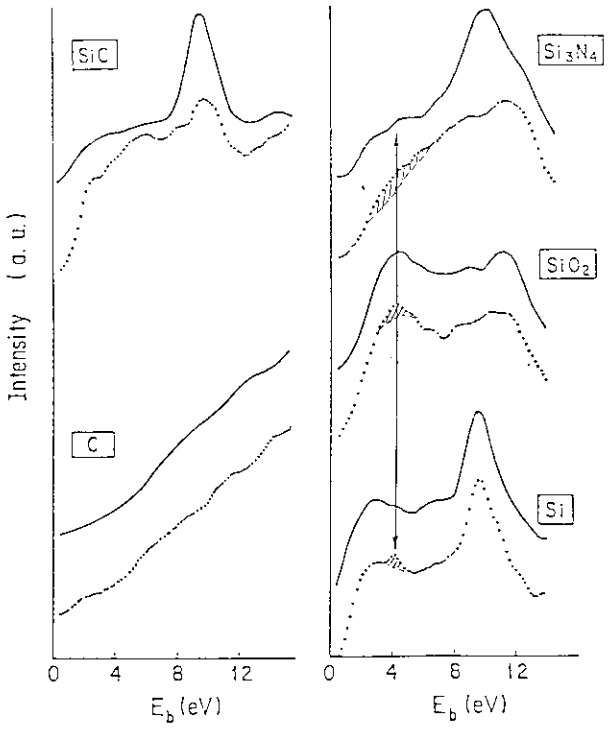

Fig. 6.6 VB XPS spectra before (——) and after (· · ·) 6-keV H_2^+-ion bombardments. Note a peak appeared at around 4 eV of Si target. This is attributable to silicon hydride(s).

remained unchanged, whereas the bombardment brought about an appearence of a weak photopeak at around 4 eV in binding energy. The similar peak was also found at the same energy position for the silicon crystal bombarded with hydrogen ions, which is also indicated in **Fig. 6.6**. Since any new photopeaks were not observed in the VB region by bombarding the Ar^+ ion, the 4-eV peak is attributed not to the radiation damage but to the formation of a new chemical bond.

6.3.3 Hydrogen-ion bombarded SiO_2 surface

Fig. 6.7 indicates the changes in the O/Si ratios in the near surface region of the SiO_2 sample as functions of the hydrogen and Ar^+-ion fluences. The O/Si ratios varied from 2.0 to 1.7 at a hydrogen fluence of 9×10^{17} atoms/cm^2. The recovery process of the O/Si ratio by the Ar^+-ion bombardment is different from those observed in the SiC and Si_3N_4 systems. The O/Si ratio of the hydrogen-ion bombarded SiO_2 became 1.75 by the prolonged etching with Ar^+ ions, which was lower by 13% than the bluk composition. The decrease in the oxygen content seems to be essential for the Ar^+-ion etching. Görlish et al.[160] have observed an appreciable change in the XPS spectral pattern in the Si2s region, accompanied by a decrease in the O/Si ratio. In the present work, the gradual decrease in the O1s/Si2p ratios (6.45→6.13) for the prolonged etching of the SiO_2 sample has been also confirmed. The phenomena are considered to be due to the preferential sputtering of O atoms from SiO_2 surface by the Ar^+-ion bombardment.

Fig. 6.8 indicates the XPS spectra in the Si2p region for the SiO_2 sample before and after the hydrogen-ion bombardment. The VB spectra of the same samples are also displayed in **Fig. 6.6**. The spectral pattern in the Si2p region for the hydrogen-ion bombarded SiO_2

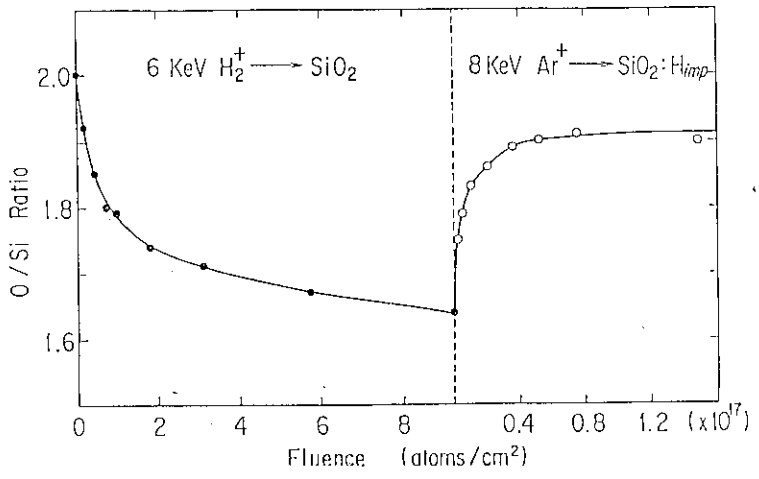

Fig. 6.7 Changes in O/Si ratios of SiO_2 as functions of hydrogen-ion and Ar^+-ion fluences.

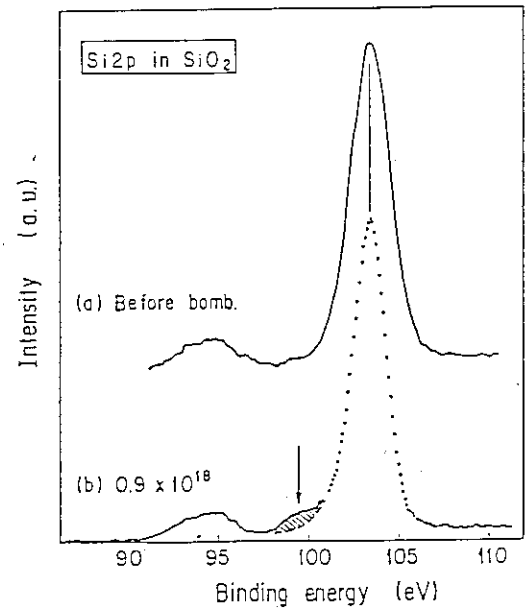

Fig. 6.8 Si2p XPS spectra of SiO_2 before and after 6-keV H_2^+-ion bombardments. An arrow indicates position of Si2p line for Si target bombarded with H_2^+ ions.

sample showed the formation of the reduced species. In addition, the hydrogen-ion bombardment brought about the appearence of a weak photopeak at around 4 eV in binding energy, as the case of the Si_3N_4 and silicon samples. The results also suggest the formation of the new chemical bond.

6.4 Discussion

6.4.1 Chemical state of ion-implanted hydrogen

The XPS spectra in the C1s region for the hydrogen-ion bombarded SiC and graphite samples, seen in **Figs. 6.2** and **6.3**, add important information to the previous observations by Yamashina and his co-workers[156,158]. First, the compositional change in question is

restricted in the near surface, because the changes in the C/Si ratios estimated from the C1s and Si2p peak intensities in the XPS spectra is less than that by AES whose resolution of the escape depth (~0.5 nm) is higher than that of XPS (~1.5 nm)[130]. Thus, the carbon-rich layer is easily removed by the Ar^+-ion etching, as seen in the right portion of **Fig. 6.1**. Since the etching rate in the present experiment was ca. 4 nm per a fluence of 2×10^{16} ions/cm^2, the thickness of the enriched layer is estimated to be within 2 nm from the top surface. Secondly, the shift of the peak position of the C1s line to the higher binding-energy implies a formation of the C-H bond. According to Wagner et al.[144], the C1s line of a polymer such as polyethylene which is composed of only carbon and hydrogen atoms locates at 284.6 eV. Thus, the hydrogen atoms implanted are possibly trapped at dangling-bond sites in the SiC surface-layer and formed the species containing C-H bond. This prediction is consistent with the observation for the graphite sample whose C1s line shifts from 284.45 eV to 284.65 eV by bombarding the hydrogen-ion, as seen in **Fig. 6.3**.

In the case of the hydrogen-ion bombarded Si_3N_4 sample, the core-line spectra in both Si2p and N1s regions show no appreciable changes within the detection limit of the core-line XPS spectra, which suggests that most of the hydrogen-ions implanted in Si_3N_4 form chemical bond with neither silicon nor nitrogen atoms and they are trapped as molecular or atomic state.

On the other hand, the 4-eV peak in the VB spectra (hatched area), in **Fig. 6.6**, show the existence of a small amount of the chemical bond, which could not be detected by the core-line spectra, newly formed by the ion-implantation. Because nitrogen atoms farely decrease accompanied by the hydrogen-ion bombardment, as seen in **Fig. 6.4**, some of the implanted hydrogens are trapped as silicon hydride(s). Furthermore, the binding energy of this photopeak is close to that reported for Si-H bond, i.e., 3.3 eV[161].

Similar trend was observed in the hydrogen-ion bombarded SiO_2. The 4-eV peak in the VB spectra for the hydrogen-ion bombarded SiO_2 also suggests the formation of the Si-H bond. The fact is confirmed by the core-line spectra in the Si2p region, seen in **Fig. 6.8**. The hatched area in the spectrum (b) is attributable to the silicon hydride.

6.4.2 Surface compositional changes by bombarding hydrogen ions

The most prominent feature for the surface compositional changes is that the SiC surface bombarded with hydrogen ion becomes Si-deficient in contrast to the other two compounds. The depletion of silicon cannot be explained in terms of thermal process, since it is well known that SiC hardly reacts with hydrogen even at high temperature[162]. Hence the result is attributed to another factor based on physical phenomena, as follows.

The ejection of atoms or molecules from solid surfaces under bombardment of energetic particles is known as sputtering. If there exist no chemical interactions between incident ions and target, the particle ejection is called physical sputtering. Therefore, physical sputtering depends on only momentum transfer from incident ions to target atoms. The magnitude of sputtering is represented by sputtering yield, defined as the number of surface atoms displaced by the bombardment of one particle.

Roth et al. have measured the sputtering yields for various elemental targets including graphite and silicon[163]. According to a universal curve deduced by them, the sputtering yields for pure graphite and silicon bombarded with 3-keV H^+ ions are estimated to be 3.8 and 6.3, respectively. At high fluence when the surface composition becomes constant, the surface C/Si ratio seems to reach opposite to that of the sputtering yields, because the number of two sputtered atoms must be equal considering the material balance. Thus the variation of C/Si ratios shown in **Fig. 6.1** is explained by the ratio of the sputtering yields of two

components, i.e., graphite and silicon. The present result suggests that the process of the ion-induced reaction is different from that of the thermochemical one, and contribution of physical sputtering is predominant in the case of the hydrogen-ion bombarded SiC.

Regarding the hydrogen-ion bombarded Si_3N_4 and SiO_2, there exist no data available for the estimation of the sputtering yields of nitrogen and oxygen atoms. In thermal process, there reported no chemical reaction between Si_3N_4 and hydrogen, and SiO_2 is not reduced up to 1350°C[164]. Thus the present results also suggest that the process of the ion-induced reaction differs from that of the thermal reaction.

Fig. 6.9 summarizes the variation rates of the compositional changes. In three silicon-containing ceramics examined, the rate of the compositional change for the Si_3N_4 sample is the lowest. The surface compositional change of the SiC sample is over 30% even at 5.3×10^{18} atoms/cm^2, while the change of the SiC sample is over 30% even at 2.2×10^{18} atoms/cm^2. Although the rate for the compositional change of the SiO_2 sample is larger than those for the other two, the equilibrium seems to reach at the lowest fluence.

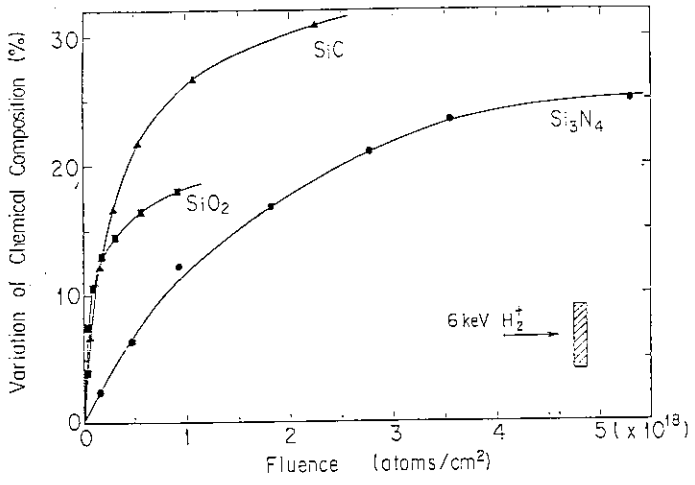

Fig. 6.9 Variation of the compositional changes for the SiC, Si_3N_4 and SiO_2 samples vs. hydrogen-ion fluence. The values plotted are data by the XPS measurements.

6.5 Conclusions

1) 6-keV H_2^+-ion bombardment on SiC made its surface carbon-rich. The result can be explained by the larger sputtering yield of silicon by the 3-keV H^+-ion bombardment than that of graphite. Whereas hydrogen-ion bombarded Si_3N_4 and SiO_2 surfaces became silicon-rich.

2) Although the binding energies of the Si2p and Si2p lines for SiC did not change after the hydrogen-ion bombardment, the C1s line shifted to higher binding energy, which suggests the formation of the C-H bond by the implantation of hydrogen ions.

3) The binding energies of the Si2p and N1s lines for the hydrogen-ion bombarded Si_3N_4 showed no appreciable changes, but a new small photopeak attributed to the Si-H bond appeared at 4.0 eV in the VB region.

4) The VB spectra of hydrogen-ion bombarded SiO_2 showed a new photopeak at 4.0 eV which corresponds to the Si-H bond. The result is consistent with the changes in the core-line spectrum in the Si2p region.

7. Surface chemical changes of TiC, TiN and TiO_2 by light-ion bombardments

7.1 Introduction

Metallic carbides and nitrides have been attracted much attention as structural and functional materials because of their prominent properties such as high melting point, extreme hardness and high electrical conductivity[165,166]. Among these compounds, titanium carbide (TiC) as well as titanium nitride (TiN) is now considered to be one of the candidate materials as first-wall of tokamak fusion-reactor, due to its refractory nature and low sputtering yield by the bombardment of energetic particles[167-170]. As the surface state of a first-wall material plays an important role in depression of plasma impurity, extensive data have been recently accumulated about physical and chemical changes of ion-bombarded TiC surfaces. With respect to the surface chemical composition, it has been observed in these works that carbon atoms of TiC is depleted from the surface accompanied by the bombardments of hydrogen isotopes[171-175]. Although the carbon depression apparently induces the changes in the surface bond-structure, the chemical state of TiC surface after the ion-bombardments has scarcely been examined yet. Moreover, the trapping state of implanted hydrogen isotopes, which is of importance for the evaluation of the tritium recycling, still remains obscure.

Regarding the bond structures of pure TiC and TiN, on the other hand, the nature of the Ti-C and Ti-N bonds have been revealed at length in recent years from both theoretical and experimental points of view. Band-structure and molecular-orbital calculations have elucidated the density of states near the Fermi-edge for TiC[176-183] and TiN[181,182,184,185]. Experimentally, the VB structures of these compounds have been measured with the photoelectron spectroscopy (PE). The results obtained with UPS for TiC[186-190] and TiN[184,188,191,192], and with XPS for TiC[176,186,190] and TiN[191,193] are fairly well consistent with the above calculated values.

In this chapter, an XPS is applied to the investigation of the surface chemical state of TiC and TiN bombarded with (0.5-10)-keV of light-ions such as H_2^+, D_2^+ and He^+. For comparison, ion-bombardments are also carried out on TiO_2 surface, because the practical surface of the first-wall materials containing titanium is considered to be oxidized to TiO_2. Besides XPS, an AES is employed to elucidate the surface compositional changes accompanied by the ion-bombardments. The species of the secondary ions emitted from the surfaces by the ion-bombardments are also analyzed by a quadrupole mass analyzer.

7.2 Experimental

7.2.1 Samples

TiC and TiN were of 20 μm-thickness deposited on molybdenum substrates by CVD method at JAERI (Japan Atomic Energy Research Institute) and Research & Development Center of Toshiba Corp., respectively. The sample surfaces were mechanically polished with diamond paste of 1/4 μm to make mirrorlike planes. TiO_2 was prepared by a following procedure. A highly pure titanium foil (99.9%) was polished with emery paper and diamond paste of 1/4 μm to make mirrorlike plane. Then the surface of the foil was oxidized at 550°C for 3 hours in oxygen atmosphere.

All the samples were attached to copper holders, then annealed at 450°C for 3 hours in the spectrometer chamber at a pressure of 1.5×10^{-7} Pa.

The clean surfaces of TiC and TiN were obtained by Ar^+-ion etchings at room temperature. This was performed by bombarding the samples with (6-8)-keV Ar^+ ions from PIG ion-gun at the current density of 15 μA for 10-60 min. After this treatment, carbon and oxygen-containing adsorbates were sufficiently removed, and the peak-intensity ratios of C1s/Ti2p and N1s/Ti2p became 0.12 and 0.23, respectively, both of which are almost equal to the theoretical ratios calculated by Scofield[194]. On the other hand, the sputter cleaning brought about the reduction of TiO_2. **Fig. 7.1** shows the Ti2p XPS spectra of TiO_2 bombarded with Ar^+ ions at various energies and fluences. After the bombardment of 8-keV Ar^+ ions, the Ti2p peaks of the reduced species, assigned to TiO, are observed at 455.7 eV. An appearence of the reduced species was also observed even when bombarded with 4-keV Ar^+ ions at 4 μA for 20 sec. Therefore, surface adsorbates were removed with fairly faint beams (2.5 keV, 0.3 μA, 30-60 sec). After this treatment, any reduced apecies were not observed in the Ti2p region.

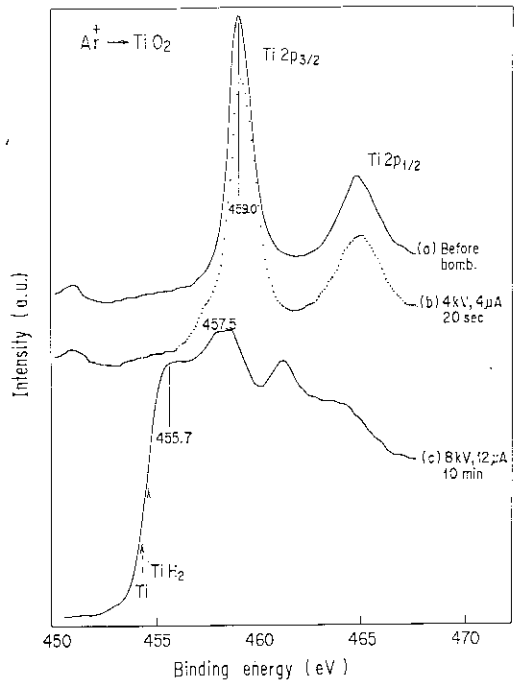

Fig. 7.1 Ti2p XPS spectra of TiO_2 before (a) and after (b), (c) Ar^+-ion bombardments. The peak positions of metallic titanium and hydride are indicated as arrows.

7.2.2 Bombardments

Schematic diagram of the ion-bombardments and measurements is shown in **Fig. 7.2**. The samples were bombarded with (0.5-10)-keV of H_2^+, D_2^+ and He^+ ions from the duoplasmatron ion-gun. The H_2, D_2 and He gases introduced into the ion-gun were purified by passing through molecular sieves at liquid nitrogen temperature. The ions produced in the ion-gun were mass-separated by the analyzing magnet, and introduced into the analyzer chamber. As the analyzer chamber and beam line were independently evacuated, the pressure of the analyzer chamber was $\sim5\times10^{-5}$ Pa during the ion bombardment. At the extraction voltage below 5 kV, the current density falls rapidly. Therefore in the case of the bombardments

of the low-energy ions below 5 keV, 5-keV H_2^+, D_2^+ and He^+-ions were bombarded on the target which was positively supplied with +(1-4.5)-keV bias.

The fluence of the ion-beam was measured directly by the ion current in the sample. Whereas it is well known that the beam durrent measured by a flat plate is generally different from real current measured by Faraday cup. Thus the beam currents were measured, in advance, by both flat plate and Faraday cup in the same size. The ratios of the current intensities measured by flat plate to Faraday cup, I_p/I_f , are displayed in **Fig. 7.3**. Although the I_p/I_f values are almost independent of the ion energies for He^+ and Ar^+ beams, there exist abrupt increase in the I_p/I_f at higher energies than 7 keV for H_2^+ beam. This increase is attributable to the high yield of secondary electron emission by H_2^+-ion bombardment at

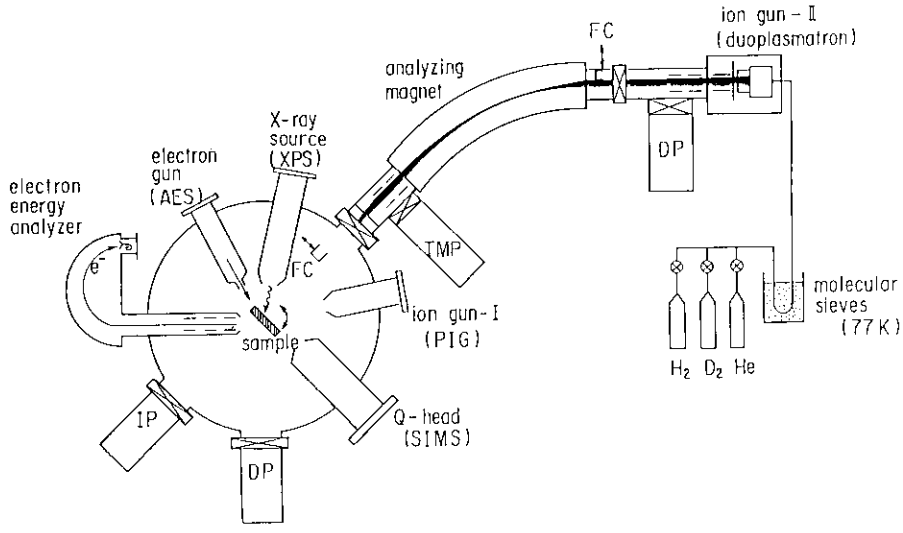

Fig. 7.2 Schematic diagram of ion bombardment and measurements.

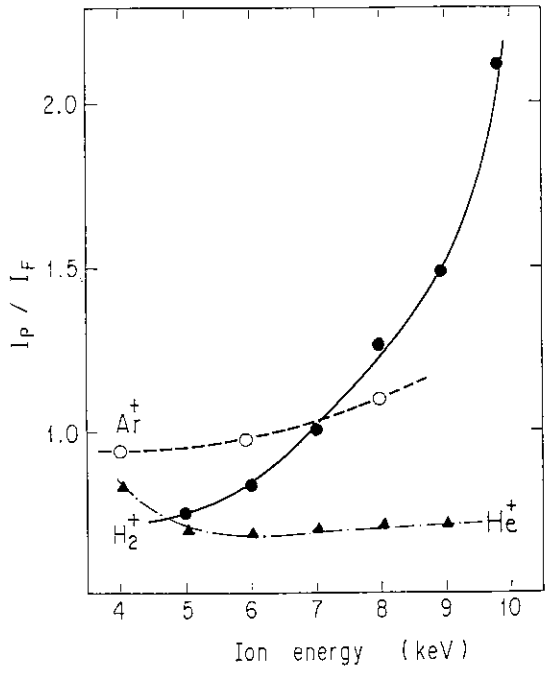

Fig. 7.3 Ratios of H_2^+, He^+ and Ar^+-ion currents measured by flat plate (I_p) to Faraday cup (I_f) as a function of ion energy.

higher energies. Upon these results, the fluences of the ion beams measured directly by the target current were corrected according to the I_p/I_f value at each energy.

7.2.3 Measurements

The conditions of XPS and AES measurements were the same as those described in chapters 2 and 6, respectively. The positive ions emitted from the surfaces by the ion bombardments were analyzed by a quadrupole mass-analyzer (Nippon Electric Varian Ltd. AGA-360). The beam currents during the mass analysis were 1 $\mu A/cm^2$.

7.3 Results

7.3.1 Ion-bombarded TiC surface

Figs. 7.4 and **7.5** show the XPS spectra in the Ti2p and C1s regions, respectively, for the TiC sample before and after the bombardments of 4-keV H_2^+ ions. The peak positions of the $Ti2p_{3/2}$, $Ti2p_{1/2}$ and C1s lines for the clean surface of TiC are almost the same as those of the previous observations using single-crystal TiC[190,195]. Although small amounts of oxide-peaks seem to be overlapped on the Ti2p line, the peak energies of the $Ti2p_{3/2}$ and $Ti2p_{1/2}$ lines remained unchanged after the ion bombardment. Moreover, the peaks corresponding to neither metallic titanium nor hydride, indicated as arrows, were observed up to the total fluences of 3×10^{18} atoms/cm^2. In the spectrum of the C1s line, a small peak was observed at 285 eV after the bombardment. The peak is assigned to the adsorbates of organic carbon[144]. Whereas the main peak-position of the C1s line did not change after the ion bombardment up to the total fluence of 3×10^{18} atoms/cm^2.

The bombardments of D_2^+ and He^+ ions were also carried out on the TiC sample. However, no appreciable changes in the core-line spectral patterns were observed.

The VB spectrum of the hydrogen-ion bombarded TiC is displayed in **Fig. 7.6** together

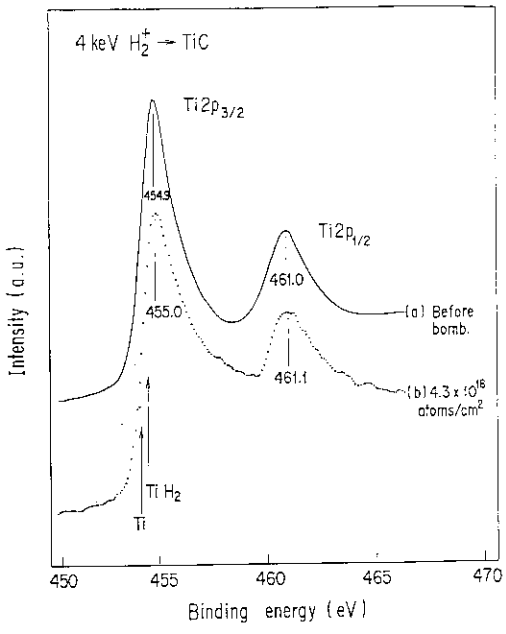

Fig. 7.4 Ti2p XPS spectra of TiC before and after 4-keV H_2^+-ion bombardment. The peak positions of metallic titanium and hydride are indicated as arrows.

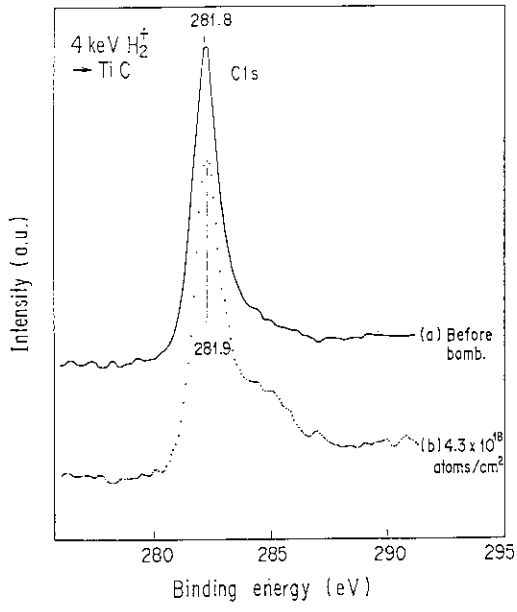

Fig. 7.5 C1s XPS spectra of TiC before and after 4-keV H_2^+-ion bombardment.

with that of the pure TiC surface. In the spectrum for the pure TiC, two peaks are observed. The lower-energy peak at 3.7 eV corresponds to the hybridized Ti3d and C2p states, and the higher-energy one at 10.9 eV is attributed to the isolated C2s obrital[177]. After the hydrogen-ion bombardment, a peak of the oxide-containing adsorbate was observed at around 6.8 eV. At the left-hand side of the 3.7-eV peak, a small shoulder was clearly observed at 3.0 eV, which is close to that of the hydrogen-ion implanted titanium metal, seen in **Fig. 3.3.**

The changes in the surface composition of TiC following the hydrogen-ion bombardments were also examined by AES as well as XPS. **Fig. 7.7** indicates the AES spectra of TiC before and after the bombardments of 0.8-keV H_2^+ ions. The peak heights in the spectra were normalyzed at those of the Ti(LMM) lines. Apparently, appreciable decreases in the intensities of the C(KLL) lines are observed after the bombardments.

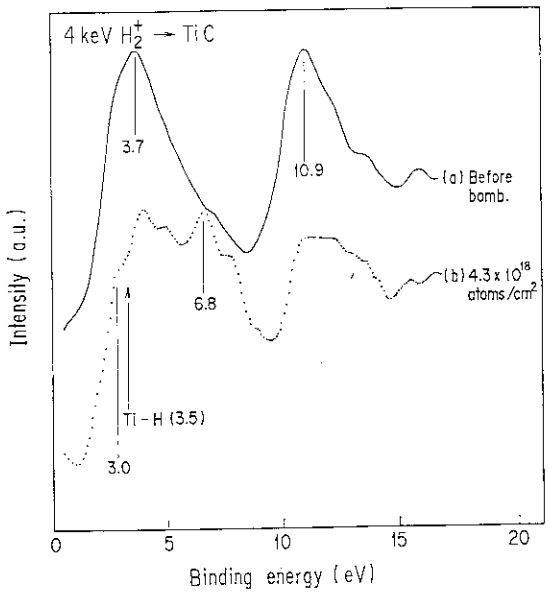

Fig. 7.6 VB XPS spectra of TiC before and after 4-keV H_2^+-ion bombardment. A small shoulder is clearly observed at 3.0 eV after the hydrogen-ion bombardment. The energy of this shoulder is approximately equal to that of the Ti-H bond, indicated as an arrow.

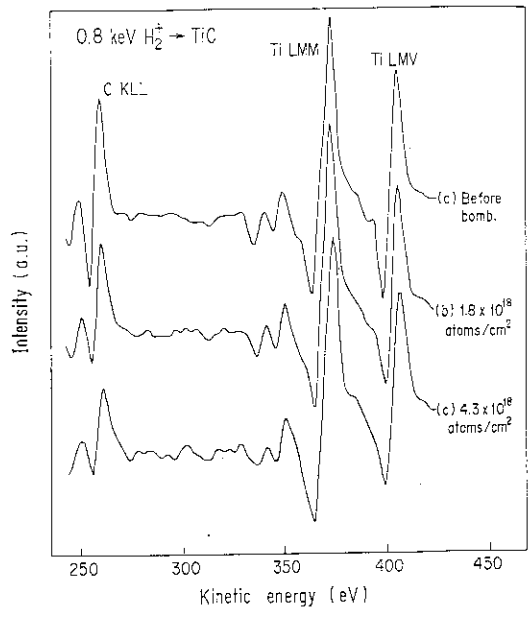

Fig. 7.7 AES spectra of TiC before (a) and after (b), (c) 0.8-keV H_2^+-ion bombardment. The intensities of the spectra are normalized at the Ti(LMM) peaks.

Fig. 7.8 shows the changes in the C/Ti ratios, which were measured by both XPS and AES, as functions of the D_2^+ and Ar^+-ion fluences. In both cases, the C/Ti ratios decrease with the increase in the hydrogen-ion fluence, whereas the ratio obtained by XPS is higher than that obtained by AES at each fluence. Considering that the escape depths of the C(KLL) and Ti(LMM) Auger electrons are relatively deep compared with those of the C1s and Ti2p photoelectrons[130], the result suggests that the changes in the C/Ti ratios are restricted in the near surface region, as the case of the hydrogen-ion bombarded SiC (chapter 6).

Fig. 7.9 displays the changes in the surface contents of carbon for the hydrogen-ion bombarded TiC as a function of the fluence. The result presents two pieces of important information on the further discussions. First, there exists appreciable energy-dependence on the rate of the carbon-depression. The bombardment of 0.8-keV H_2^+ ions reduces the surface composition of carbon from 0.5 to 0.37 at the fluence of 2.8×10^{18} atoms/cm^2, while it is reduced only to 0.46 by the bombardment of 5.0-keV H_2^+ ions at the same fluence. Secondly,

the content of carbon decreases rapidly at lower fluences, whereas it gradually becomes constant values over the fluence of 2×10^{18} atoms/cm^2.

The secondary ion mass spectrum (SIMS) of TiC by bombarding 6-keV D_2^+ ions is displayed in **Fig. 7.10**. Besides the C^+ and Ti^+ ions, combined ions such as CD^+, CD_2^+, TiD^+ and TiD_2^+ are considerably detected, while the intensity of the TiC^+ ion (M=60) is relatively small compared with that of Ti^+.

Fig. 7.11 indicates the energy dependences of the SIMS signal intensities measured at the same beam currents. The intensities of C^+ and CD^+ ions have a maximum at 1-1.5 keV/atom, whereas those of Ti^+ and TiD^+ ions are the highest at 1.5-2.5 keV/atom.

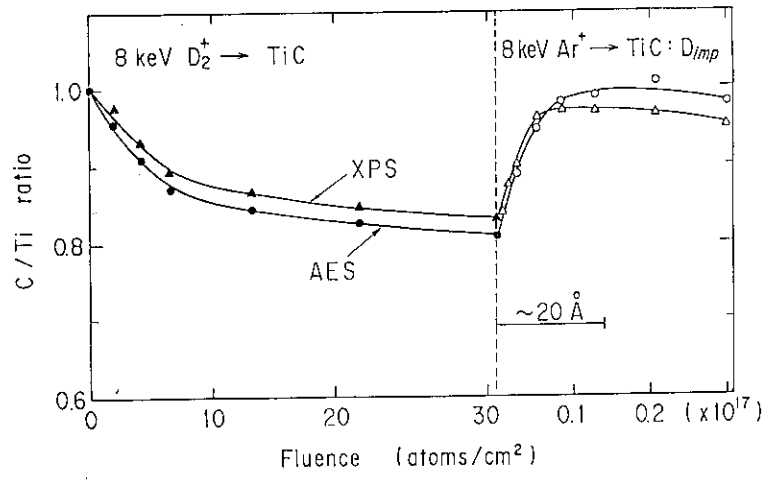

Fig. 7.8 Changes in C/Ti ratios measured by XPS and AES for TiC bombarded with 8-keV D_2^+ and Ar^+ ions as functions of fluences.

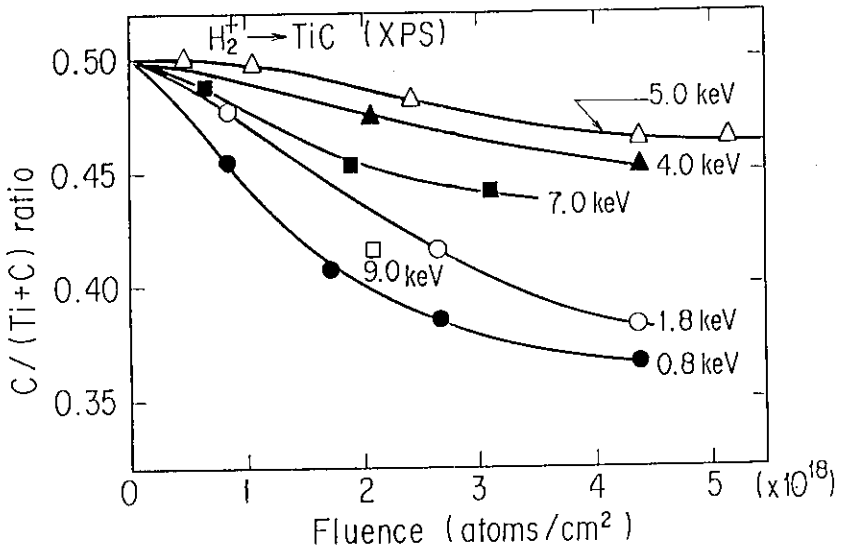

Fig. 7.9 Changes in surface C/(Ti+C) ratios measured by XPS for TiC bombarded with H_2^+ ions at various energies as a function of fluence.

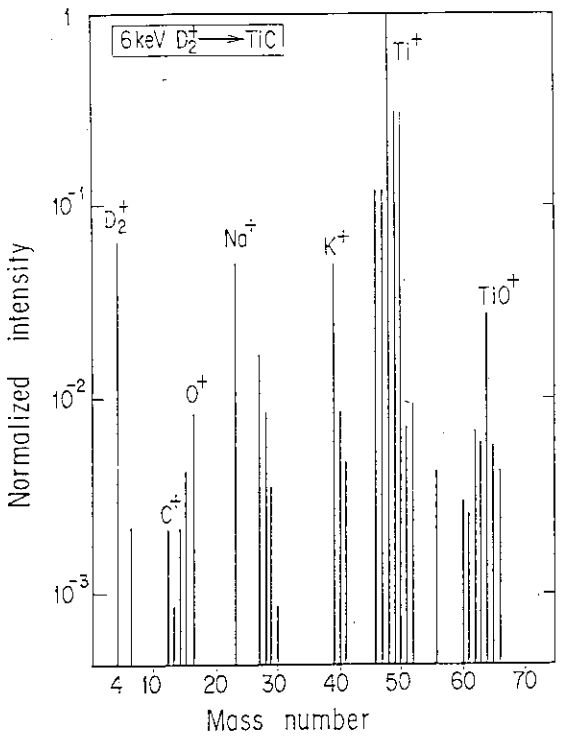

Fig. 7.10 SIMS spectrum of TiC bombarded with 6-keV D_2^+ ions.

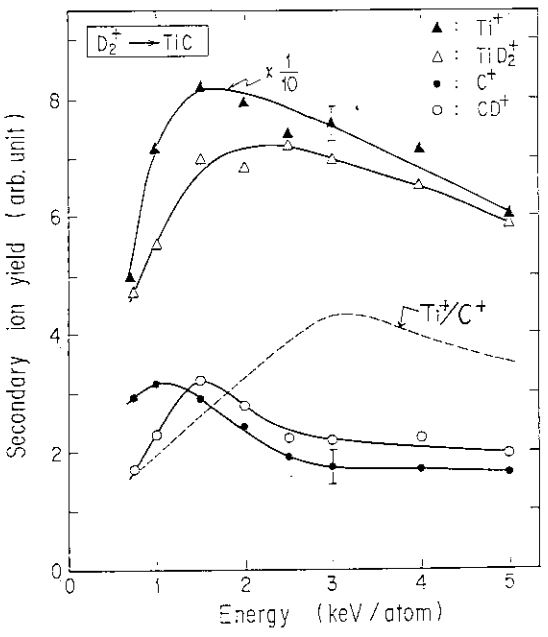

Fig. 7.11 Energy dependences of SIMS signal intensities for TiC bombarded with D_2^+ ions. The dotted line indicates the intensity ratios of Ti^+/C^+.

7.3.2 Ion-bombarded TiN surface

The peak positions of the $Ti2p_{3/2}$, $Ti2p_{1/2}$ and N1s lines for the pure TiN are 455.2 eV, 461.1 eV and 397.4 eV, respectively. The peak energies are in consistent with the reported values[191,193]. The core-line spectral pattern remained unchanged after the hydrogen-ion bombardments up to the fluence of 3×10^{18} atoms/cm^2 except for the small overlap of the oxide peak resulting from the adsorbed oxygen. The results indicate that neigher metallic titanium nor hydride phases were produced in the near surface region of TiN after the hydrogen-ion bombardment. The VB spectrum of pure TiN consists of two peaks. The lower-energy peak at 6.0 eV corresponds to the hybridized Ti3d and N2p states, whereas the higher-energy one at 16.6 eV is attributed to the isolated N2s orbital[188,191]. The hydrogen-ion bombardment did not bring about any appreciable changes in the VB spectral patterns up to 3×10^{18} atoms/cm^2.

Fig. 7.12 represents the changes in the surface contents of nitrogen atom for TiN bombarded with H_2^+ ions at various energies as a function of the fluences. The surface of the TiN sample becomes titanium-rich accompanied by the hydrogen-ion bombardments, as the case of the TiC sample. On the other hand, the energy-dependence on the rate of the nitrogen-depression is different from that of the TiC system. The N/(Ti+N) ratios of TiN surface bombarded with 1-keV H_2^+ ions varied from 0.5 to 0.47 at the fluence of 2.8×10^{18} atoms/cm^2, whereas the bombardment of 9-keV H_2^+ ions reduced it to 0.40 at the same fluence. Thus the content of nitrogen atom decreases monotonously with the increase in the ion energy.

The SIMS spectrum of TiN bombarded with 6-keV H_2^+ ions and the energy-dependences of the signal intensities are indicated in **Figs. 7.13** and **7.14**, respectively. The signal intensities of Ti^+ and TiH_2^+ ions have maximum values at 1.5 keV/atom, while those of N^+ and NH^+ ions are almost constant regardless of the ion energy.

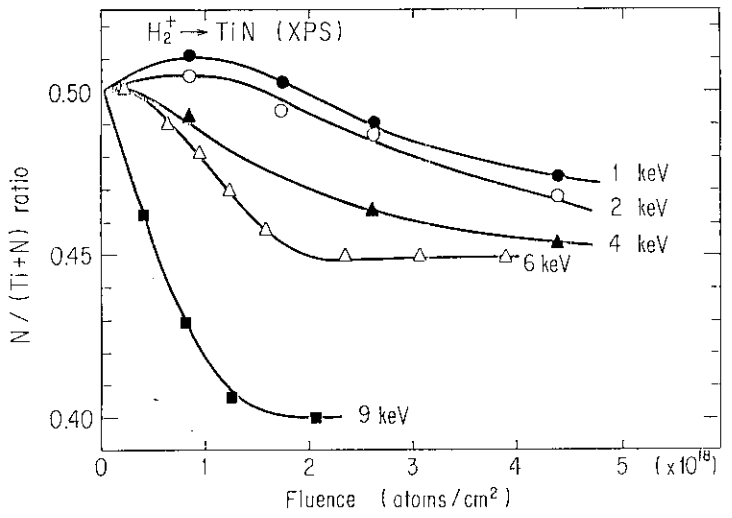

Fig. 7.12 Changes in surface N/(Ti+N) ratios measured by XPS for TiN bombarded with H_2^+ ions at various energies as a function of fluence.

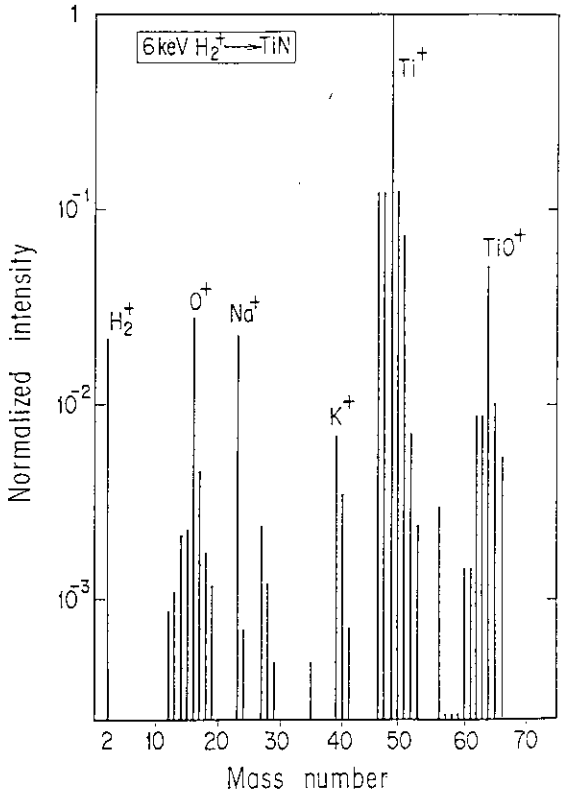

Fig. 7.13 SIMS spectrum of TiN bombarded with 6-keV H_2^+ ions.

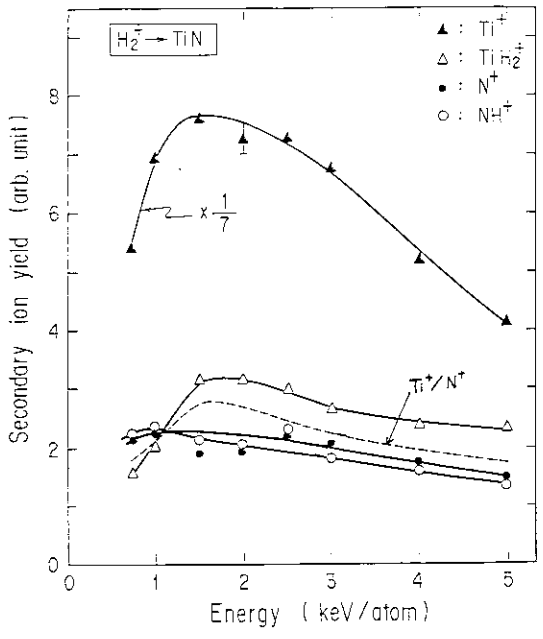

Fig. 7.14 Energy dependences of SIMS signal intensities for TiN bombarded with H_2^+ ions. The dotted line indicates the intensity ratios of Ti^+/N^+.

7.3.3 Ion-bombarded TiO_2 surface

Fig. 7.15 shows the Ti2p spectra for TiO_2 before and after the bombardments of 6-keV H_2^+ and He^+ ions. Although the spectral pattern did not show any appreciable changes in the O1s region, there appeared a slight split of the $Ti2p_{3/2}$ peak after the H_2^+-ion bombardment. The energy of the left-hand shoulder of the $Ti2p_{3/2}$ peak, i.e., 457.8 eV, did not change

with the energy of the incident ions. The energy of the shoulder is the same as that for the D_2^+-ion bombarded sample, while the He^+-ion bombardment brought about an appearence of a peak at lower binding-energy, i.e., 455.7 eV. The binding energy of this peak is the same as that produced by the Ar^+-ion bombardment (**Fig. 7.1**). The results suggest that the reduction of TiO_2 by the ion bombardment is closely related to the chemical reactivity of the incident ions.

Fig. 7.16 represents the AES spectra of TiO_2 before and after the bombardment of 6-keV H_2^+ ions. The curve (c) represents the AES spectrum for the sample further bombarded with 8-keV Ar^+ ions after the hydrogen-ion bombardment. The 6-keV H_2^+-ion bombardment brought about a slight decrease in the intensity ratios of O(KLL)/Ti(LMM), while it decreased further when bombarded with 8-keV Ar^+ ions. The decrease in the O(KLL)/Ti(LMM) ratios seems to be related with the reduction of TiO_2 by the ion bombardments (**Figs. 7.1, 7.13**).

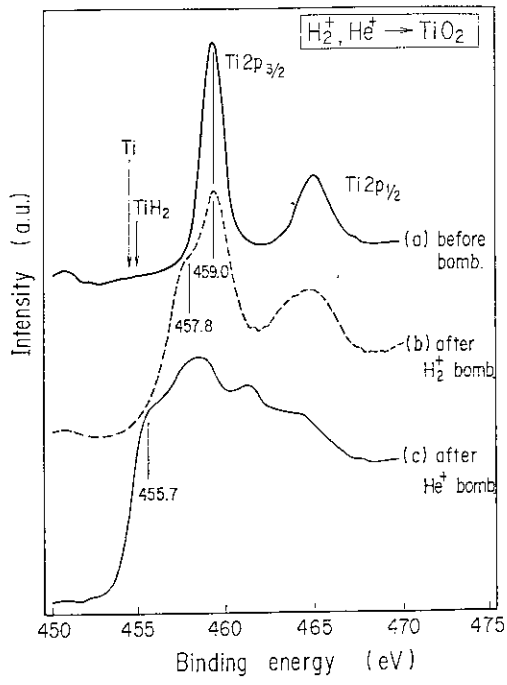

Fig. 7.15 Ti2p XPS spectra of TiO_2 before and after 6-keV H_2^+ and He^+-ion bombardments. Note that the changes in the spectral patterns are different in ion species. The peak positions of metallic titanium and hydride are indicated as arrows.

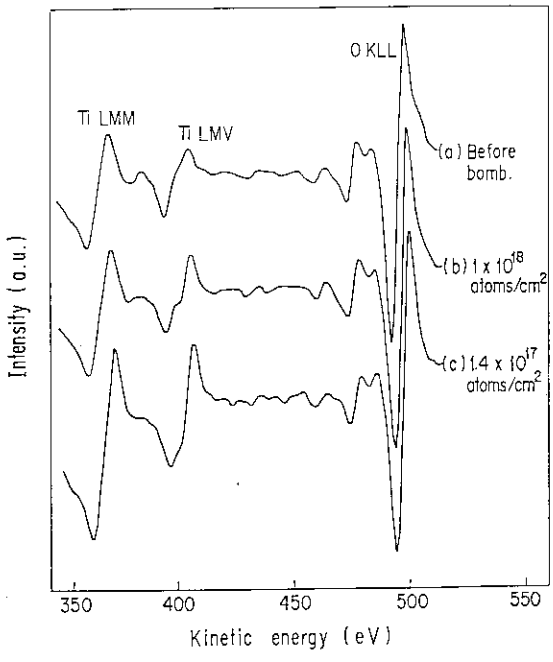

Fig. 7.16 AES spectra of TiO_2 before (a) and after (b) 6-keV H_2^+-ion bombardment. Curve (c) indicates the spectrum for the hydrogen-ion bombarded sample further bombarded with 8-keV Ar^+ ions.

More quantitative results are presented in **Fig. 7.17**, which shows the variations of the O/Ti ratios measured by both XPS and AES. At each fluence, the O/Ti ratio measured by XPS is higher than that obtained by AES, as the case of the hydrogen-ion bombarded TiC. The fact suggests that oxygen atoms are removed from the near surface region of TiO_2. On the other hand, the rate of the decrease in the O/Ti ratio is far more rapid than that in the C/Ti ratio (**Figs. 7.8, 7.9**). The ratio becomes constant value over the fluence of only 3×10^{17} atoms/cm^2. In addition, it decreases further more rapidly by the Ar^+-ion bombardment. These results indicate the instability of the Ti-O bond against the ion bombardment.

The changes in the surface oxygen contents of the hydrogen-ion bombarded TiO_2 are

presented in **Fig. 7.18**. In analogy with the TiN system, the variations of the surface compositions are enhanced with the increase in the ion-energies.

The SIMS spectrum of TiO_2 bombarded with 6-keV D_2^+ ions, and the energy dependences of the signal intensities are displayed in **Figs. 7.19** and **7.20**, respectively. The energy dependences of signal intensities are rather complex compared with those for the TiC and TiN systems.

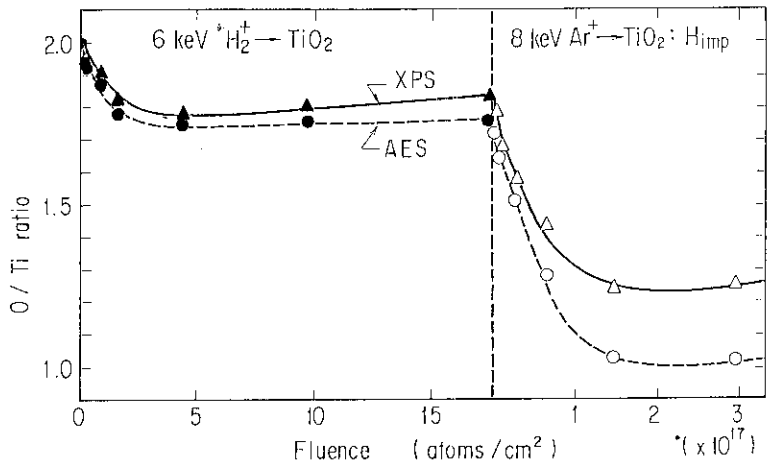

Fig. 7.17 Changes in O/Ti ratios measured by XPS and AES for TiO_2 bombarded with 6-keV H_2^+ ions and 8-keV Ar^+ ions as functions of ion fluences.

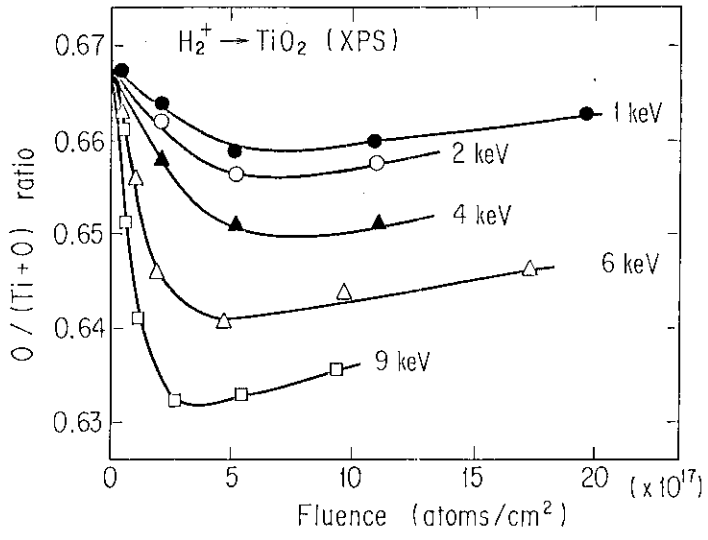

Fig. 7.18 Changes in surface O/(Ti+O) ratios measured by XPS for TiO_2 bombarded with H_2^+ ions at various energies as a function of fluence.

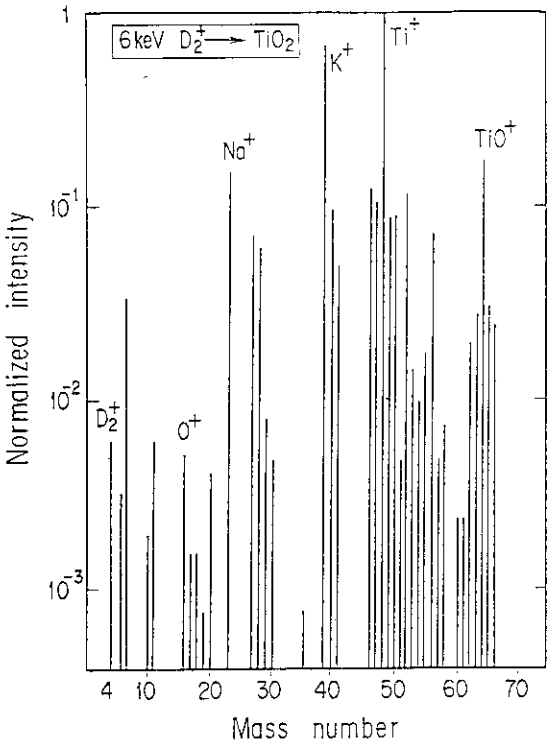

Fig. 7.19 SIMS spectrum of TiO_2 bombarded with 6-keV D_2^+ ions.

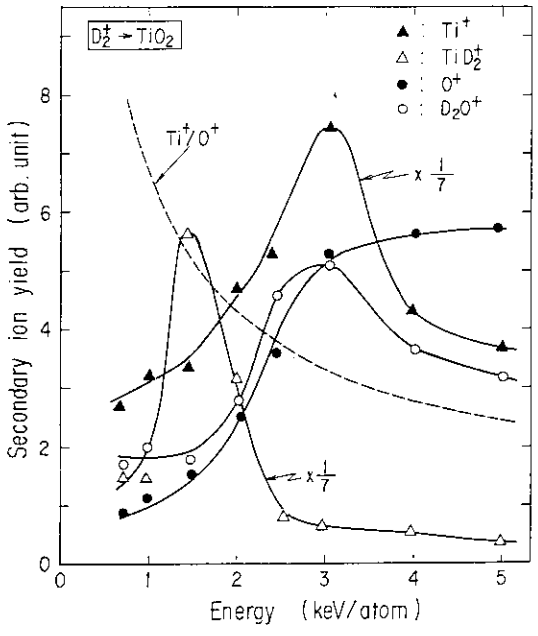

Fig. 7.20 Energy dependences of SIMS signal intensities for TiO_2 bombarded with D_2^+ ions. The dotted line indicates the intensity ratios of Ti^+/O^+.

7.4 Discussion

7.4.1 Surface compositional changes

The depression of carbon atoms from TiC surface by the hydrogen-ion bombardments, seen in **Figs. 7.8** and **7.9**, is consistent with the results reported by other workers[171–175]. Since there exist no chemical reactions between TiC and hydrogen through thermal process[196], the depression of carbon seems to be attributed to the sputtering by the ion bombardment, which is merely related to the momentum transfer from the incident ions to the target atoms. This assumption is confirmed by the following considerations.

Fig. 7.21 shows the energy dependences of the C/Ti ratios for the H_2^+, D_2^+, He^+ and Ar^+-ion bombarded TiC at high fluence in which the C/Ti ratios become constant. In order to compare the C/Ti ratios with the sputtering yield of two components, the ratios of the sputtering yields, Y, of pure titanium to graphite are also indicated in **Fig. 7.21**. The sputtering yields of titanium and graphite are cited from experimental values compiled by Roth et al.[163].

At high fluence when the surface composition becomes constant, the surface C/Ti ratio is considered to become opposite to that of the sputtering yields, i.e., Y_{Ti}/Y_C, because the ratio of the two sputtered atoms must be equal to the bulk composition, considering the material balance. A more quantitative treatment has been presented by Ho[197].

He calculated theoretically surface compositional changes by ion bombardments for binally alloy using sputtering yields of two components and diffusion coefficient of the sputtered atom in the solid. His calculation has revealed that a surface composition of the component a, C_a, in a--b alloy at steady state is expressed as following equation,

$$C_a = C_{a_0} Y_b / [Y_a(1-C_{a_0}) + Y_b C_{a_0}] \quad \cdots\cdots\cdots\cdots\cdots\cdots\cdots\cdots\cdots\cdots \quad (1)$$

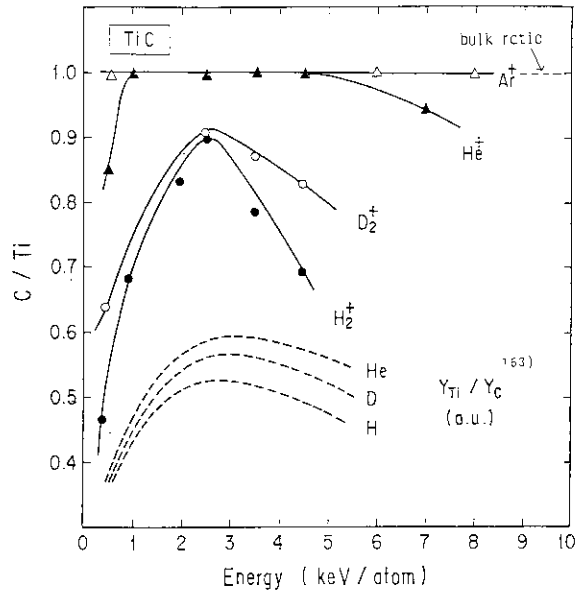

Fig. 7.21 Energy dependences of C/Ti ratios at steady state for TiC bombarded with various light ions. Dotted lines are the ratios of sputtering yields of titanium to graphite, taken from ref. 163.

where C_{a_0} is the bulk composition of component a , Y_a and Y_b are the sputtering yields of respective elements. As C_{a_0} equals to 0.5 in the TiC system, the surface composition of titanium C_{Ti} at steady state is represented as

$$C_{Ti}=Y_C/(Y_{Ti}+Y_C) \quad \cdots\cdots (2).$$

In the same manner, the surface concentration of carbon C_C is indicated as

$$C_C=Y_{Ti}/(Y_{Ti}+Y_C) \quad \cdots\cdots (3).$$

From equations (2) and (3), we obtain

$$C_C/C_{Ti}=Y_{Ti}/Y_C \quad \cdots\cdots (4).$$

In **Fig. 7.21**, the ratios of C/Ti have the maximum values at 2.5 keV/atom for H_2^+ and D_2^+-ion bombarded TiC and at 1.0-4.5 keV for He^+-ion bombarded one, respectively. The energy-dependences of all samples are similar to those of the calculated Y_{Ti}/Y_C ratios using the Roth's values, indicated as dotted lines.

Another evidence for the correlation between the compositional change and sputtering was obtained in the SIMS experiment, shown in **Fig. 7.11**. In this experiment, the current density of the incident ions was reduced down to 1 $\mu A/cm^2$. Thus the surface composition did not change during the measurements. The general trends for the C^+ and Ti^+ ion yields are similar to those of the sputtering yields for the graphite and titanium metal[163], though the maximum position in **Fig. 7.11** slightly shift to the higher energy side. The Ti^+/C^+ signal ratio in the D_2^+ bombardment is shown as dotted line.

According to the previous work by Gries and Rüdenauer[198], the yield of secondary ion A^+ for the bombarding ion with energy E_i is given as,

$$S_A^+=9.70\times10^{-3}\cdot\frac{\alpha S_n(E_i)U_s^{3/2}}{\bar{a}M^{1/2}(1-\phi)^3} \quad \cdots\cdots (5)$$

where α, $S_n(E_i)$ and U_s are a dimensionless quantity depending upon the mass ratio M_2/M_1 and the incident energy, the stopping nuclear cross-section and surface-barrier energy of

the target atom with atomic mass M_2, respectively, and I, ϕ and $\bar{a}$ are the ionization energy of the target atom, the work function and a fitting parameter, respectively. As the sputtering process can be described by the linear collision cascade model[199] in the present energy region, the yield Y_A of sputtered atom A in the nautral and ionic states is obtained as,

$$Y_A = \frac{0.042\,\alpha\,S_n(E_i)}{U_s} \quad \cdots\cdots (6).$$

From eqs. (5) and (6), we obtain $S_{Ti}^{+} \propto Y_{Ti}$ and $S_C^{+} \propto Y_C$ for the sputterings of pure titanium and graphite, respectively. If the sputtering of TiC is caused only by the physical factor relating to the momentum transfer from the incident ions to the target, the following equation can be expected,

$$\frac{S_{Ti}^{+}}{S_C^{+}} \propto \frac{Y_{Ti}}{Y_C} \quad \cdots\cdots (7).$$

It should be noted that the above equation is valid only at the initial state when the atomic ratio of C/Ti equals to 1. Therefore eq. (4) can be expressed as,

$$\frac{C_C}{C_{Ti}} \propto \frac{S_{Ti}^{+}}{S_C^{-}} \quad \cdots\cdots (8)$$

for the TiC target. The similarities of the energy dependence between **Fig. 7.11** (dotted line) and **Fig. 7.21** qualitatively assure the assumption that the surface compositional change, at least in the present energy region, is induced by the physical sputtering of Ti and C atoms, which is related to only momentum transfer from the incident ions to the target atoms.

Consequently, it is concluded that the sputtering is responsible for the surface compositional changes for the ion-bombarded TiC, and there exists no appreciable evidence for the chemical effect of the incident ions on the TiC surface.

In contrast to the TiC system, energy-dependence of the surface N/Ti ratio for the ion-bombarded TiN did not show the maximum values in the energy range of 0.5-4.5 keV/atom, as shown in **Fig. 7.22**. As there exist no available data for the sputtering yield of nitrogen, such energy-dependences of N/Ti ratios cannot be further discussed at the present stage. The depression of nitrogen atoms from TiN surface by the ion-bombardments is presumably associated with the large sputtering yield of nitrogen atoms compared with that of titanium.

On the other hand, the large variations in Ti2p-XPS spectra (**Figs. 7.1, 7.15**) and in the surface O/Ti ratios for the ion-bombarded TiO_2 (**Figs. 7.17, 7.18**) indicate the extreme sensitivity of TiO_2 to the ion bombardments in comparison to TiC and TiN systems. **Fig. 7.23** represents the energy-dependences of the O/Ti ratios for the ion-bombarded TiO_2 at steady state. In the case of the H_2^+-ion bombarded sample, the O/Ti ratio decreases only to 1.8, whereas it decreases to 1.3 by the He^+ and Ar^+-ion bombardments. The difference in the O/Ti ratios at steady state will be discussed in relation to the surface chemical state in the following section.

Fig. 7.24 summarizes the variation rates of the compositional changes measured by XPS as a function of the hydrogen-ion fluence. The rate for the compositional change of the TiC sample is the least in these three titanium-containing ceramics examined, and that of the TiO_2 sample is the largest. While the equilibrium reaches at the lowest fluence for TiO_2, and the value of the saturated variation is also the lowest in three compounds.

7.4.2 Changes in surface chemical states

The XPS spectrum of the hydrogen-ion bombarded titanium metal showed the energy shift of the $Ti2p_{3/2}$ line to higher-energy side by 0.3 eV from the metallic state, as shown in **Fig. 2.9**. The hydrogen-ion bombardment on graphite also brought about the slight energy

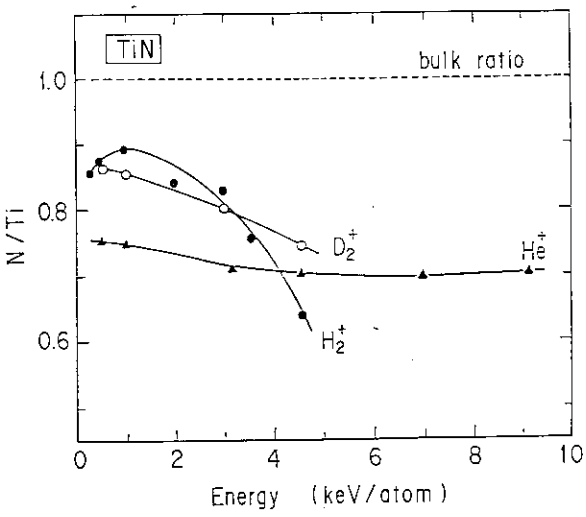

Fig. 7.22 Energy dependences of N/Ti ratios at steady state for TiN bombarded with various light ions.

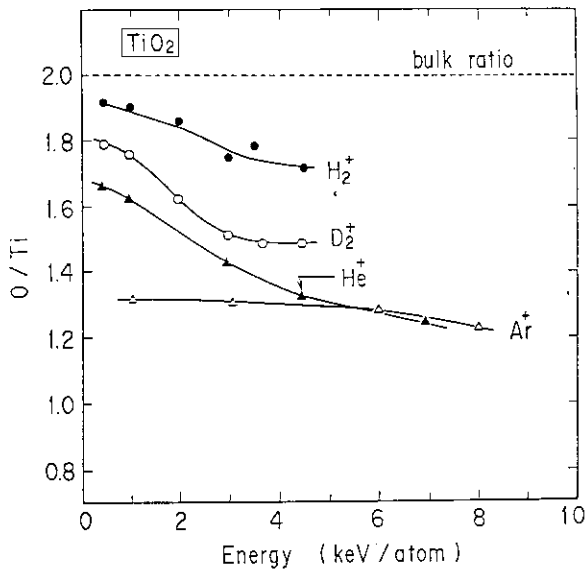

Fig. 7.23 Energy dependences of O/Ti ratios at steady state for TiO_2 bombarded with various light ions.

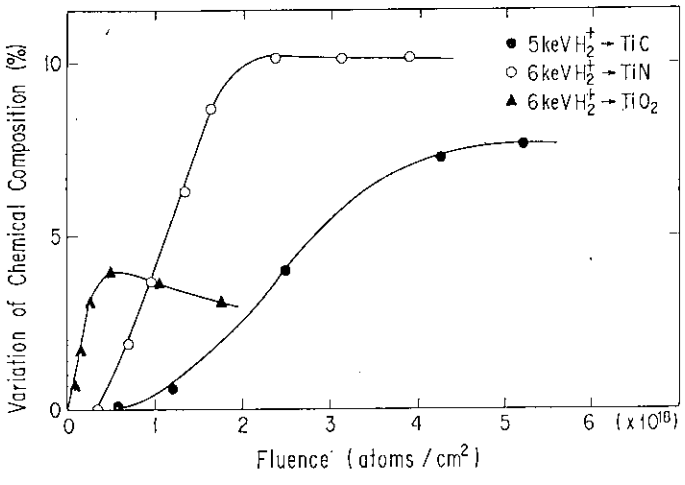

Fig. 7.24 Variations of the compositional changes for the TiC, TiN and TiO_2 samples vs. hydrogen-ion fluence. The values are the data measured by XPS.

shift of the C1s line (**Fig. 6.3**). In the case of the hydrogen-ion bombarded TiC, on the other hand, **Figs. 7.4** and **7.5** suggest that most of the hydrogen implanted in TiC forms neither Ti-H nor C-H bonds. According to the calculation by Brice et al.[220], about 80% of deutrium-ion is trapped in TiC, when exposed to 3.2-keV deutrium plasma to 10^{18} atoms/cm^2. Thus a considerable amount of hydrogen ions is assumed to be once trapped in TiC without forming chemical bond(s) with the target atoms. Therefore most of the implanted hydrogen is probably trapped in the interstitial site or void in TiC lattice as free atomic or molecular form.

A more precise observation of the changes in the surface bond-structure is obtained by the VB spectrum, indicated in **Fig. 7.6**. Although the spectral pattern scarcely changed after the hydrogen-ion bombardment except for the peak of oxide-containing adsorbate at 7 eV, a small shoulder was clearly observed at 3.0 eV. The energy of this shoulder is almost equal to the peak energy of the hydrogen-ion implanted titanium metal, seen in **Fig. 3.3**. Thus,

the shoulder is presumably attributed to the Ti-H bond. The observation of the Ti-H bond is associated with the fact that the escape depth of the VB-photoelectron, whose kinetic energy is about 1250 eV, is a little larger than that in the Ti2p region, i.e., E_k =800 eV[130], so that the detection depth of the VB spectrum is near to the range of the implanted hydrogen compared with that of the Ti2p spectrum. Hence a small fraction of the implanted hydrogen in TiC is assumed to form Ti-H bond.

The trapping state of the ion-implanted hydrogen in TiN is similar to that in TiC. Neither core-line nor VB spectra showed any appreciable changes after the hydrogen-ion bombardments, which also suggests that the trapped hydrogen stayed in TiN lattice as free atomic or molecular form.

In contrast to the TiC and TiN systems, the surface of the hydrogen-ion bombarded TiO_2 showed considerable changes in the XPS spectral pattern in the Ti2p region (**Figs. 7.1, 7.15**). For checking whether the unidentified shoulder observed in the spectrum for the hydrogen-ion bombarded TiO_2 results from the titanium hydroxide $Ti(OH)_x$ produced by the implantation of the hydrogen ions or not, the hydrogen-ion bombarded sample was heated in the analyzer chamber at a pressure of 5×10^{-7} Pa. Even after this treatment, the shoulder did not disappear up to 400°C. Considering that titanium hydroxide easily loses water below 300°C to become TiO_2[196], the present result indicates that the shoulder corresponds not to hydroxide but to the other oxide produced by the reduction of TiO_2. From the binding energies of the shoulder, the reduced species produced by the H_2^+ and D_2^+-ion bombardments are assigned to Ti_2O_3, whereas those produced by the He^+ and Ar^+-ion bombardments correspond to TiO[201]. This assignment is confirmed by the O/Ti ratios at steady state, seen in **Fig. 7.17**, as follows.

The O/Ti ratio measured by XPS for the hydrogen-ion bombarded TiO_2 at steady state is 1.78 (**Fig. 7.17**). Deconvolution of the Ti2p spectrum shows that about 58% of the Ti2p peak corresponds to the TiO_2 and the residual 42% is attributable to the reduced species, TiO_X ($X<2$). To obtain the value of X, the following calculation was done,

$$2\times0.58+X\times0.42=1.78 \quad \cdots\cdots (9).$$

From the above equation, we obtain X=1.48, thus the reduced species can be assigned to Ti_2O_3. The similar treatment for the Ar^+-ion bombarded sample revealed that the reduced species corresponds to TiO.

With respect to the reduction of metal oxide by the bombardment of rare-earth ions, Kim et al.[51,52] have investigated the mechanism of the reduction in terms of the thermodynamical parameters of the reduction reaction. According to their treatment, an Ar^+-ion bombarded oxides having higher standard Gibbs free energies of formation, ΔG, than −60 kcal/mol can be reduced to metallic state. These thermodynamical treatments are also applied to the TiO_2 system for both H_2^+ and He^+-ion bombardments, as follows.

Since the species of the stable titanium oxides at room temperature are TiO_2, Ti_2O_3 and TiO, the considerable reduction processes are summarized as,

$$2\,TiO_2 \longrightarrow Ti_2O_3 + O(a) \quad \cdots\cdots (10)$$

$$TiO_2 \longrightarrow TiO + O(a) \quad \cdots\cdots (11)$$

$$TiO_2 \longrightarrow Ti + 2\,O(a) \quad \cdots\cdots (12)$$

$$1/2\,Ti_2O_3 \longrightarrow TiO + 1/2\,O(a) \quad \cdots\cdots (13)$$

$$1/2\,Ti_2O_3 \longrightarrow Ti - 3/2\,O(a) \quad \cdots\cdots (14)$$

$$TiO \longrightarrow Ti - O(a) \quad \cdots\cdots (15)$$

where notation (a) represents a free atomic state. In order to evaluate the standard Gibbs free energies of the above reactions, the following free energies of formation[202] are used,

$$Ti(s)-1/2\,O_2(g) \longrightarrow TiO(s)+118\,(kcal/mol) \quad \cdots\cdots\cdots \quad (16)$$

$$2\,Ti(s)+3/2\,O_2(g) \longrightarrow Ti_2O_3(s)+343\,(kcal/mol) \quad \cdots\cdots\cdots \quad (17)$$

$$Ti(s)-O_2(g) \longrightarrow TiO_2(s)+213\,(kcal/mol) \quad \cdots\cdots\cdots \quad (18)$$

$$1/2\,O_2(g) \longrightarrow O(a)-55\,(kcal/mol) \quad \cdots\cdots\cdots\cdots \quad (19)$$

where notations (s) and (g) represent solid and gas phases, respectively. From equations (16)-(19), we obtain the standard Gibbs free energies of the reactions (10)-(15). The results are summarized in **Table 7.1**. Upon these results, the reaction (13) as well as (10) is the most possible to take place among the reactions (10)-(15). Thus the reduction of TiO_2 by the He^+ or Ar^+-ion bombardment is simply expressed as following two step reaction,

$$TiO_2 \xrightarrow{He^+,\,Ar^+} Ti_2O_3 \xrightarrow{He^+,\,Ar^+} TiO \quad \cdots\cdots\cdots\cdots \quad (20).$$

On the other hand, the free energy of the reduction to the metallic state, i.e., equation (15), is lower than those of the reactions (10) and (13). Assuming the threshold free energy of the reduction to be ~ -150 kcal/mol, which is close to the Kim's value, i.e., -118 kcal/mol, it is presumed that the reduction to the metallic state cannot be observed by the He^+ and Ar^+-ion bombardments.

Table 7.1 Standard Gibbs free energies ΔG of the reduction reactions for titanium oxides. The values are estimated using the ΔG values of equations (16)-(19)

Reaction	ΔG (kcal/mol)
$2\,TiO_2 \longrightarrow Ti_2O_3+O(a)$	−138
$TiO_2 \longrightarrow TiO+O(a)$	−150
$TiO_2 \longrightarrow Ti+2\,O(a)$	−268
$1/2\,Ti_2O_3 \longrightarrow TiO+1/2\,O(a)$	−134
$1/2\,Ti_2O_3 \longrightarrow Ti+3/2\,O(a)$	−255
$TiO \longrightarrow Ti+O(a)$	−174

In cases of the H_2^+ and D_2^+-ion bombardments, on the other hand, the chemical reaction of TiO_2 with hydrogen is supposed to be related to the reduction of the oxide. The possible reactions are represented as

$$2\,TiO_2+H_2 \longrightarrow Ti_2O_3+H_2O(g) \quad \cdots\cdots\cdots\cdots\cdots\cdots \quad (21)$$

$$TiO_2+H_2 \longrightarrow TiO+H_2O(g) \quad \cdots\cdots\cdots\cdots\cdots\cdots \quad (22)$$

$$TiO_2+2\,H_2 \longrightarrow Ti+2\,H_2O(g) \quad \cdots\cdots\cdots\cdots\cdots\cdots \quad (23)$$

$$1/2\,Ti_2O_3+1/2\,H_2 \longrightarrow TiO+1/2\,H_2O(g) \quad \cdots\cdots\cdots\cdots\cdots\cdots \quad (24)$$

$$1/2\,Ti_2O_3+3/2\,H_2 \longrightarrow Ti+3/2\,H_2O(g) \quad \cdots\cdots\cdots\cdots\cdots\cdots \quad (25)$$

$$TiO+H_2 \longrightarrow Ti+H_2O(g) \quad \cdots\cdots\cdots\cdots\cdots\cdots \quad (26).$$

Using the standard Gibbs free energies of the equations (16)-(19)[202] and that of the following reaction,

$$H_2(g)+1/2\,O_2(g) \longrightarrow H_2O(g)+55\,(kcal/mol) \quad \cdots\cdots\cdots\cdots \quad (27),$$

the free energies of the reactions (21)-(26) can be obtained. The results are summarized in **Table 7.2**. Compared with the bombardments of He^+ and Ar^+-ions, the free energies obtained have relatively high values. Among the reactions (21)-(26), the free energy of the reduction from TiO_2 to Ti_2O_3, i.e., −28 kcal/mol, is the highest of all the reduction reactions. If we assume the threshold free energy of the reduction by the hydrogen-ion bombardment to be ∼−30 kcal/mol, the experimental results can be explained by the high free energy of the reaction (21).

On the basis of these considerations, the ion-induced reduction of TiO_2 is related to the chemical reactivity of the ionic species rather than the sputtering by the ion-bombardment, in contrast to the TiC and TiN systems.

Table 7.2 Standard Gibbs free energies ΔG of the reactions between titanium oxides and hydrogen. The values are estimated using the ΔG values of equations (16)-(19) and (27)

Reaction	ΔG (kcal/mol)
$2\,TiO_2 + H_2 \longrightarrow Ti_2O_3 + H_2O(g)$	−28
$TiO_2 + H_2 \longrightarrow TiO + H_2O(g)$	−40
$TiO_2 + 2\,H_2 \longrightarrow Ti + 2\,H_2O(g)$	−103
$1/2\,Ti_2O_3 + 1/2\,H_2 \longrightarrow TiO + 1/2\,H_2O(g)$	−79
$1/2\,Ti_2O_3 + 3/2\,H_2 \longrightarrow Ti + 3/2\,H_2O(g)$	−137
$TiO + H_2 \longrightarrow Ti + H_2O(g)$	−64

7.5 Conclusions

1) Bombardments of 0.5-10 keV H_2^+, D_2^+ and He^+ ions on TiC, TiN and TiO_2 mostly result in the formations of titanium rich layers in the near surface regions of the targets. The surface C/Ti, N/Ti and O/Ti ratios after the H_2^+-ion bombardments reach constant values over the fluences of 5×10^{18}, 2×10^{18} and 3×10^{17} atoms/cm^2, respectively.

2) The surface of the C/Ti ratios at steady state for H_2^+, D_2^+ and He^+-ion bombarded TiC become maximum at the energy of 2-4 keV/atom. The energy dependence of the surface compositional changes is interpreted with the ratios of the sputtering yields of titanium to graphite. On the other hand, the surface N/Ti and O/Ti ratios at steady state decrease with the increase in the ion energies.

3) Ion bombarded TiC and TiN do not show any appreciable changes in the XPS spectral patterns in core-line regions, whereas the bombardments of light ions induce the reduction of TiO_2. The reduced species are Ti_2O_3 for the H_2^+ and D_2^+-ion, and TiO for the He^+ and Ar^+-ion bombardments, respectively. The difference in the reduced species is correlated to the standard Gibbs free energies of the corresponding reduction reactions.

Acknowledgements

The author would like to thank Drs. T. Abe of JAERI (Department of Thermonuclear Fusion Research) and S. Sukenobu of Toshiba Co. (R and D Center) for providing the CVD samples.

8. Summary

Among interactions between the energetic ions and the solid, changes in the surface chemical state have become important from both scientific and technological viewpoints. A conventional method to analyze the chemical species produced by the ion bombardment, mainly developed in the field of radiation chemistry, is based on the chemical method involving the dissolution of the ion-bombarded sample. On the other hand, several non-destructive methods have been applied to the analysis of the surface chemical state of ion-bombarded solids. Among these methods, a photoelectron spectroscopy was adopted in this work in the surface chemical studies of the ion-bombarded solids because of its superiority in analyzing molecular species and surface sensitivity. The chemical states of light-ion bombarded some transition metals and low-Z ceramics, some of which are considered to be candidate materials of the first-wall of fusion reactor, were analyzed by X-ray photoelectron spectroscopy (XPS), X-ray-induced Auger electron spectroscopy (XAES) and Auger electron spectroscopy (AES).

Some 3d and 4d transition metals were bombarded with 8-keV H_2^+ ions to the fluence of 1×10^{18} atoms/cm^2 using PIG ion gun. The binding energies of the XPS core-lines for scandium, titanium, vanadium, yttrium, zirconium and niobium metals shifted to higher energies by 0.2-1.4 eV after the ion bombardments. The chemical shifts obtained are almost the same as those of the thermally synthesized hydrides. The results indicate that the hydrogens implanted in these metals form hydride layers whose chemical compositions are close to those of the thermally synthesized hydrides. On the other hand, the core-line spectra of the hydrogen-ion bombarded chromium, nickel and molybdenum did not show any appreciable changes up to a total fluence of 3×10^{18} atoms/cm^2, which suggests that the implanted hydrogens are trapped as an atomic or molecular form in the metal lattice of defect produced by the ion-bombardment.

The hydrogen-ion bombardments on scandium, titanium, vanadium, yttrium, zirconium and niobium brought about the appearence of new VB-photopeaks attributed to the metal hydrides. The peak energies observed are lower by 1-3 eV than those calculated for the stoichiometric hydrides by DV-Xα cluster method. The difference in the peak energies seems to be due to the radiation damages produced by the ion bombardments.

To compare the thermal stability of the hydrides produced by the ion implantation with that of the thermally synthesized hydrides, the hydrogen-ion bombarded metals were annealed in the spectrometer chamber at various temperatures. The photopeaks corresponding to the Ti-H bond for $Ti:H_{imp}$ grew up on raising the annealing temperature up to 550°C because of the thermal diffusion of hydrogen from the bulk to the surface. On the other hand, the photopeak of the V-H bond disappeared at 350°C for $V:H_{imp}$ and 150°C for $VH_{0.55}$, respectively. The $YH_{2.98}$ sample decomposed at 300°C, while the ion-implanted hydrogen is not released up to 450°C. The thermal stability of the hydrides produced by the ion implantation was also observed for the bombarded zirconium and niobium. The fact is interpreted by the lowering of the thermal diffusion of hydrogen in the surface damage layer.

Besides XPS, an XAES was also used for the identification of the metal-H bond for the hydrogen-ion implanted 4d transition metals. The chemical shifts of the X-ray-induced $M_{4,5}N_{2,3}V$ Auger lines for $Y:H_{imp}$, $Zr:H_{imp}$ and $Nb:H_{imp}$ are 1.0 eV, 3.3 eV and 2.2 eV, respectively. These values are larger than the chemical shifts of the corresponding $3d_{5/2}$ lines in the XPS spectra. The XAES energy shifts are related to the extra-atomic relaxation energies

of the compounds. The shift of the extra-atomic relaxation energy measured from the isolated atomic state is much larger for $Y:H_{imp}$ than that for Y_2O_3, reflecting a larger polarizability of the Y-H bond than that of the Y-O bond.

The XPS and AES were applied to the surface chemical studies of ion-bombarded low-Z ceramics which are considered to be candidate materials of the first-wall of fusion reactor. The surface of the SiC bombarded with 6-keV H_2^+ ions became carbon-rich, which can be explained by the sputtering of the constituent elements, i.e., silicon and carbon. The implanted hydrogen forms the C-H bond in SiC, which was confirmed by the XPS chemical shift of the C1s line. In contrast, the bombardments of hydrogen ions on Si_3N_4 and SiO_2 made their surfaces silicon-rich. Although core-line spectra of Si_3N_4 show no appreciable changes, there appeared a new photopeak at 4.0 eV below the Fermi level. The similar photopeak was also observed for the hydrogen-ion bombarded SiO_2. The peak energy is a little larger than the reported value for the Si-H bond, suggesting that the implanted hydrogen is firmly trapped at dangling bond produced by the ion bombardment.

The bombardments of H_2^+, D_2^+ and He^+-ions on TiC, TiN and TiO_2 brought about titanium enrichments in the near surface regions, whereas the surface C/Ti, N/Ti and O/Ti ratios became constant at high fluences. The C/Ti ratios at steady state became maximum at 2-4 keV/atom, when bombarded with H_2^+, D_2^+ and He^+ ions. The incident-energy dependence of the C/Ti ratios is correlated with that of the sputtering yields of titanium to graphite. In contrast, the surface N/Ti and O/Ti ratios at steady state decrease with the increase in the ion energies. Incident-energy dependences of the Ti^+/X^+ (X=C, N, O) ratios determined by SIMS substantiate that the sputtering is responsible for the surface compositional change of the binary compounds. The bombardments of H_2^+, D_2^+ and He^+ ions on TiC and TiN did not bring about any appreciable changes in the core-line XPS spectra, while the surface of TiO_2 is easily reduced by the ion bombardments. The chemical species assigned are Ti_2O_3 for the H_2^+ and D_2^+-ion bombardments, and TiO for the He^+ and Ar^+-ion bombardments, respectively. The difference in the chemical species is interpreted in terms of the standard Gibbs free energies of the respective reduction reactions.

Throughout this work, it was revealed that an electron spectroscopic methods such as XPS, XAES and AES are effective to elucidate the surface chemical state of ion-bombarded solids. Further electron spectroscopic studies combined with SIMS will provide much more information on the ion-induced chemical reactions of solid surfaces.

Acknowledgments

The author would like to express his thanks to Professor Takeshi Tominaga of University of Tokyo for many valuable suggestions in the course of this study.

The author also wish to acknowledge Dr. Teikichi A. Sasaki of JAERI for his helpful discussions and suggestions throughout this work.

The author is deeply indebted to Dr. Takuji Komori, the members of Analytical Chemistry Laboratory, and the members of Solid State Chemistry Laboratory of JAERI for their valuable discussions. Thanks are also due to Dr. Kaoru Ueno, Director of Department of Chemistry of JAERI for his continuous encouragement.

of the compounds. The shift of the extra-atomic relaxation energy measured from the isolated atomic state is much larger for $Y:H_{imp}$ than that for Y_2O_3, reflecting a larger polarizability of the Y-H bond than that of the Y-O bond.

The XPS and AES were applied to the surface chemical studies of ion-bombarded low-Z ceramics which are considered to be candidate materials of the first-wall of fusion reactor. The surface of the SiC bombarded with 6-keV H_2^+ ions became carbon-rich, which can be explained by the sputtering of the constituent elements, i.e., silicon and carbon. The implanted hydrogen forms the C-H bond in SiC, which was confirmed by the XPS chemical shift of the C1s line. In contrast, the bombardments of hydrogen ions on Si_3N_4 and SiO_2 made their surfaces silicon-rich. Although core-line spectra of Si_3N_4 show no appreciable changes, there appeared a new photopeak at 4.0 eV below the Fermi level. The similar photopeak was also observed for the hydrogen-ion bombarded SiO_2. The peak energy is a little larger than the reported value for the Si-H bond, suggesting that the implanted hydrogen is firmly trapped at dangling bond produced by the ion bombardment.

The bombardments of H_2^+, D_2^+ and He^+-ions on TiC, TiN and TiO_2 brought about titanium enrichments in the near surface regions, whereas the surface C/Ti, N/Ti and O/Ti ratios became constant at high fluences. The C/Ti ratios at steady state became maximum at 2-4 keV/atom, when bombarded with H_2^+, D_2^+ and He^+ ions. The incident-energy dependence of the C/Ti ratios is correlated with that of the sputtering yields of titanium to graphite. In contrast, the surface N/Ti and O/Ti ratios at steady state decrease with the increase in the ion energies. Incident-energy dependences of the Ti^+/X^+ (X=C, N, O) ratios determined by SIMS substantiate that the sputtering is responsible for the surface compositional change of the binary compounds. The bombardments of H_2^+, D_2^+ and He^+ ions on TiC and TiN did not bring about any appreciable changes in the core-line XPS spectra, while the surface of TiO_2 is easily reduced by the ion bombardments. The chemical species assigned are Ti_2O_3 for the H_2^+ and D_2^+-ion bombardments, and TiO for the He^+ and Ar^+-ion bombardments, respectively. The difference in the chemical species is interpreted in terms of the standard Gibbs free energies of the respective reduction reactions.

Throughout this work, it was revealed that an electron spectroscopic methods such as XPS, XAES and AES are effective to elucidate the surface chemical state of ion-bombarded solids. Further electron spectroscopic studies combined with SIMS will provide much more information on the ion-induced chemical reactions of solid surfaces.

Acknowledgments

The author would like to express his thanks to Professor Takeshi Tominaga of University of Tokyo for many valuable suggestions in the course of this study.

The author also wish to acknowledge Dr. Teikichi A. Sasaki of JAERI for his helpful discussions and suggestions throughout this work.

The author is deeply indebted to Dr. Takuji Komori, the members of Analytical Chemistry Laboratory, and the members of Solid State Chemistry Laboratory of JAERI for their valuable discussions. Thanks are also due to Dr. Kaoru Ueno, Director of Department of Chemistry of JAERI for his continuous encouragement.

References

1) Wolfgang R. : Progress in Reaction Kinetics, 3, 97 (1965).
2) Carter G. and Colligon J.S. : "Ion Bombardment of Solid", Heinemann, London (1968).
3) Nelson R.S. : "The Observation of Atomic Collisions in Crystalline Solids", North-Holland, Amsterdam (1968).
4) Anderson T. and Ebbesen A. : Trans. Faraday Soc., 67, 3540 (1971).
5) Anderson T. : "Chemical Effects of Nuclear Transformations in Inorganic Systems", edited by Harbottle G. and Maddock A.G., North-Holland, Amsterdam, chap.23 (1979).
6) Preece C.M. and Hirvonen J.K. : "Ion Implantation Metallurgy", The Metallurgical Society of AIME, New York (1980).
7) Hubber G.K., Holland O.W., Clayton C.R. and White C.W. : "Ion Implantation and Ion Beam Processing of Materials", North-Holland, New York (1984).
8) Auciello O. and Kelly R. : "Ion Bombardment Modification of Surfaces", Elsevier, Amsterdam (1984).
9) Chernow F., Borders J.A. and Brice D.K. : "Ion Implantation in Semiconductors", Plenum Press, New York (1977).
10) Fan J.C.C. and Johnson N.M. : "Energy Beam-Solid Interactions and Transient Thermal Processing", North-Holland, New York (1984).
11) Maeda D.M. : Nucl. Fusion, 14, 289 (1974).
12) Eckhartt D. and Venus G. : JET Technical Note, 9 (1974).
13) Croatto U. and Giacomello G. : "Acta 45th Congress of SIPS", Naples (1954).
14) Wolfgang R. : J. Inorg. Nucl. Chem., 2, 180 (1956).
15) Andersen T. and Sørensen G. : Nucl. Instrum. Methods, 38, 204 (1965).
16) Andersen T. and Sørensen G. : Trans. Faraday Soc., 62, 3427 (1966).
17) Freeman J.H., Kasrai M. and Maddock A.G. : Chem. Comm., 19, 979 (1967).
18) Ascoli S., Cacace F., Giacomello G. and Possagno E. : J. Phys. Chem., 71, 427 (1967).
19) Paulus J.M. : Radiochim. Acta, 7, 141 (1967).
20) Wolf. G.K. and Fritsch T. : ibid., 11, 194 (1969).
21) Kasrai M., Maddock A.G. and Freeman J.H. : Trans. Faraday Soc., 67, 2108 (1971).
22) Jenkins G.M. and Wiles D.R. : Chem. Comm., 1177 (1972).
23) Chou N.J., Osburn C.M., van der Mueler Y.J. and Hammer R. : Appl. Phys. Lett., 22, 380 (1973).
24) Elman B.S., Shayegan M., Dresselhaus M.S., Mazurek H. and Dresselhaus G. : Phys. Rev., B 25, 4142 (1982).
25) Mathieu H.J. and Landolt D. : Applicat. Surf. Sci., 10, 100 (1982).
26) Fransen F., Vanden Berghe R., Vlaeminck R., Hinoul M., Remmerie J. and Maes H.E. : Surf. Interface Anal., 7, 79 (1985).
27) Lundquist T.R., Burgner R.P., Swann P.R. and Tsong I.S.T. : Applicat. Surf. Sci., 2, 7 (1981).
28) Takadoum J., Pivin J.C., Pons-Corbeau J., Berneron R. and Charbonnier J.C. : Surf. Interface Anal., 6, 174 (1984).
29) Hory J. and Que're' Y. : Rad. Effects, 13, 57 (1972).
30) Takai M., Tsien P.H., Tsou S.C., Roschenthaler D., Ramin M., Ryssel H. and Ruge I. : Appl. Phys., 22, 129 (1980).
31) Gruska B. and Götz G. : Phys. Stat. Sol. (a), 67, 129 (1981).
32) Freeman J.H., Grad G.A., Mazey D.J., Stephen J.H. and Whiting F.B. : Int. Conf. Application of Ion Beam to Semiconductor Technology, Grenoble, France, 75 (1967).
33) Pavlov P.V. and Shitova E.V. : Sov. Phys. Doklady, 12, 11 (1967).
34) Patricia A.F., Dieter M.G. and Dennis L.P. : "Radiation Effects on Solid Surfaces", edited by Kaminsky M., American Chem. Soc., Washington D.C., 30 (1976).
35) Hamilton J.C., Mills B.E. and Benner R.E. : Appl. Phys. Lett., 40, 499 (1982).
36) Myers D.R. and Grourley P.L. : J. Electrochem. Soc., 130, 217 (1983).
37) Wehner G.K. and Hajicek D.J. : J. Appl. Phys., 42, 1145 (1971).
38) Tsunoyama K., Suzuki T. and Ohashi Y. : Japanese J. Appl. Phys., 15, 349 (1976).
39) Malinowski M.E. : J. Vac. Sci. Technol., 16, 962 (1979).
40) Stulen R.H. : Applicat. Surf. Sci., 5, 212 (1980).
41) Bhatia C.S. : Thin Solid Films, 96, 249 (1982).
42) Daly D.F. and Pickar K.A. : Appl. Phys. Lett., 15, 267 (1969).
43) Brower K.L. and Borders J.A. : ibid., 16, 169 (1970).

44) de Wit J.G. and Ammerlaan C.A.J. : "Ion Implantation in Semiconductors", edited by Ruge I. and Graul J., Springer, Berlin, 39 (1971).
45) Brower K.L. and Beezhold W. : J. Appl. Phys., 43, 3499 (1972).
46) Siegbahn K., Nordling C., Fahlman R., Nordberg R., Hamrin K., Hedman J., Johansson G., Bergmark T., Karlsson S.E., Lindgren I. and Lindberg B. : "ESCA, Atomic, Molecular and Solid State Structure Studied by Means of Electron Spectroscopy", Almqvist and Wiksells, Uppsala (1967).
47) Siegbahn K., Nordling C., Johansson G., Heden P.F., Hamrin K., Gelius U., Bergmark T., Werme L.O., Manne R. and Baer Y. : "ESCA, Applied to Free Molecules", North-Holland, Amsterdam (1969).
48) Rabalais J.W., Colton R.J. and Guzman A.M. : Chem. Phys. Lett., 29, 131 (1974).
49) De Angelis B.A. : J. Electron Spectrosc. Relat. Phenom., 9, 81 (1976).
50) Sasaki T., Williams R.S., Wong J.S. and Shirley D.A. : J. Chem. Phys., 68, 2718 (1978), 69, 4374 (1978), 71, 4601 (1979).
51) Kim K.S., Baitinger W.E., Amy J.W. and Winograd N. : J. Electron Spectrosc., 5, 351 (1974).
52) Kim K.S., Baitinger W.E. and Winograd N. : Surf. Sci., 55, 285 (1976).
53) Holm R. and Storp S. : Physica Scripta, 16, 442 (1977).
54) Tsang T., Coyle G.J., Adler I. and Yin L. : J. Electron Spectrosc. Relat. Phenom., 16, 389 (1979).
55) Storp S. and Holm R. : ibid., 16, 183 (1979).
56) Bigelow R.W., Black J.G., Duke C.B., Salaneck W.R. and Thomas H.R. : Thin Solid Films, 94, 233 (1982).
57) Hofmann S. and Sang J.M. : Fresenius Z. Anal. Chem., 314, 215 (1983).
58) Christic A.B., Lee J., Sutherland I. and Walls J.M. : Applicat. Surf. Sci., 15, 224 (1983).
59) Göpel W., Anderson J.A., Frankel D., Jaehnig M., Phillips K., Schafer J.A. and Rocker G. : Surf. Sci., 139, 333 (1984).
60) Tomas J.H. and Hofmann S. : J. Vac. Sci. Technol., A3, 1921 (1985).
61) Mackey K.M. : "Hydrogen Compounds of the Metallic Elements", Spon Ltd., London (1966).
62) Mueller W.M., Blackledge J.P. and Libowitz G.G. : "Metal Hydrides", Academic Press, New York (1968).
63) Fromm E. and Gebhardt E. : "Gase und Kohlenstoff in Metallen", Springer, Berlin (1976).
64) Alefeld G. and Völkl J. : "Hydrogen in Metals I", Springer, Berlin (1978).
65) Alefeld G. and Völkl J. : "Hydrogen in Metals II", Springer, Berlin (1979).
66) McCracken G.M. : Rep. Progr. Phys., 38, 241 (1975).
67) Bohdansky J., Roth J., Sihha M.K. and Ottenberger W. : J. Nucl. Mater., 63, 115 (1976).
68) Möller W. : Nucl. Instrum. Methods, 209/210, 773 (1983).
69) Bernstein I.M. and Thompson A.W. : Int. Met. Rev., 212, 269 (1976).
70) Beachem C.D. : "Hydrogen Damage", American Society for Metals, Metals Park, Ohio (1977).
71) Behrisch R. : J. Nucl. Mater., 85/86, 1047 (1979).
72) Roberto J.B., Isler R.C., Kasai S., Murray L.E., Simpkins J.E., Withrow S.P. and Zuhr R.A. : ibid., 103/104, 531 (1981).
73) Bøttiger J. : ibid., 78, 161 (1978).
74) Pontau A.E., Haggmark L.G., Wilson K.L., Bastasz R., Malinowski M.E., Dawson D.B. and Bauer W. : ibid., 85/86, 1013 (1979).
75) Pontau A.E., Wilson K.L., Greulich F. and Haggmark L.G. : ibid., 91, 343 (1980).
76) Sheft I., Reiss Jr. A.H., Gruen D.M. and Pterson S.W. : ibid., 59, 1 (1976).
77) Wilson K.L. : Proc. Institute on Curriculum Development in Fusion, Center for Educational Affairs, ALA, Vol.1, chp.13 (1976).
78) Malinowski M.E. : J. Vac. Sci. Technol., 16, 962 (1979).
79) Slater J.C. and Koster G.F. : Phys. Rev., 94, 1498 (1954).
80) Ebisuzaki M. and O'Keefe M. : Prog. Solid State Chem., 4, 187 (1967).
81) Sasaki T.A. and Soga T. : J. Surf. Sci. Soc. Jpn., 3, 17 (1982).
82) Nefedov V.I., Salyn' Ya.V., Chertkov A.A. and Padurets L.N. : Russ. J. Inorg. Chem., 19, 785 (1974).
83) Lamartine B.C., Haas T.W. and Solomon J.S. : Applicat. Surf. Sci., 4, 537 (1980).
84) Schlapbach L. and Scherrer H.R. : Solid State Commun., 41, 893 (1982).
85) Fujimori A. and Schlapbach L. : J. Phys., C 17, 341 (1984).
86) Veal B.W., Lam D.J. and Westlake D.G. : Phys. Rev., B 19, 2856 (1979).
87) Wainwright C., Cook A.J. and Hopkins B.E. : J. Less Common Met., 6, 362 (1964).
88) Kim K.S., Sell C.D. and Winograd N. : Proc. Symp. Electrocatal., edited by Breiter M.W., 242 (1974).
89) Guentherschulze A. and Tollmien W. : Z. Phys., 119, 685 (1942).
90) Wehner G.K. and Hajicek D.J. : J. Appl. Phys., 42, 1145 (1971).
91) Cherns D. : Phil. Mag., 36, 1429 (1977).
92) Verheij L.K., Van den Berg J.A. and Armour D.G. : Surf. Sci., 122, 216 (1982).

93) Ley L., Kowalczyk S.P., McFeely F.R., Pollak R.A. and Shirley D.A. : Phys. Rev., B 8, 3583 (1975).
94) Wagner C.D. : Faraday Discuss. Chem. Soc., 60, 291 (1975).
95) Miller G.L. : "Tantalum and Niobium", Butterworths Scientific Publication, London, 372 (1959).
96) Nefedov V.I., Gati D., Dzhurinskii B.F., Sergushin N.P. and Salyn' Ya.V. : Zh. Neorg. Khim., 20, 2307 (1975).
97) Gimzewski J.K., Fabian D.J., Watson L.M. and Affrossman S. : J. Phys., F 7, 1305 (1977).
98) Sawatzky G.A. and Post D. : Phys. Rev., B 20, 1546 (1979).
99) Werfel F., Drager G. and Berg U. : Cryst. Res. Technol., 16, 119 (1981).
100) Kasperkiewicz J., Kovacich J.A. and Lightman D. : J. Electron Spectrosc. Relat. Phenom., 32, 123 (1983).
101) Makurin Y.N., Streskalovskii V.N. and Vorkorub E.G. : J. Struct. Chem., 21, 147 (1980).
102) Winterbon K.B. : "Ion Implantation Range and Energy Deposition Distributions", Vol.2, Plenum, New York (1977).
103) Anderson H.H. and Ziegler J.F. : "Hydrogen Stopping Powers and Ranges in All Elements", Pergamon, New York (1977).
104) Fontaine R., Caillat R., Feve L. and Guittet M.J. : J. Electron Spectrosc. Relat. Phenom., 10, 349 (1977).
105) Bøttiger J., Picraux S.T., Rud N. and Lausen T. : J. Appl. Phys., 48, 920 (1977).
106) Bernas H., Traverse A., Brossard L., Chaumont J., Lalu F. and Dumoulin L. : Nucl. Instrum. Methods, 182/183, 1033 (1981).
107) Möller W. and Bøttiger J. : J. Nucl. Mater., 88, 95 (1980).
108) Staudenmaier G., Roth J., Behrisch R., Bohdansky J., Eckstein W., Staib P., Matterson S. and Erent S.K. : ibid., 84, 149 (1979).
109) Doyle B.L., Brice D.K. and Wampler W.R. : Rad. Effects Lett., 57, 81 (1980).
110) Möller W., Besenbacher F. and Bøttiger J. : Appl. Phys., A 27, 19 (1982).
111) Switendick A.C. : Ber. Bunseges. Phys. Chem., 76, 535 (1972).
112) Switendick A.C. : J. Less-Common Met., 49, 283 (1976).
113) Switendick A.S. : "Transition Metal Hydrides", American Chemical Society, Washington D.C., 311 (1978).
114) Klikov N.I., Borozov V.N. and Zvonkov A.D. : Phys. St. Sol., B 86, 83 (1978).
115) Switendick A.C. : Z. Phys. Chem. Neue Folge, 117, S.89 (1979).
116) Peterman D.J., Harmon B.N. and Marchiando J. : Phys. Rev., B 19, 4867 (1979).
117) Peterman D.J. and Harmon B.N. : ibid., B 20, 5313 (1979).
118) Gupta M. : Solid State Commun., 29, 47 (1979).
119) Gupta M. and Burger J. : Phys. Rev., B 24, 7099 (1981).
120) Gupta M. : ibid., B 25, 1207 (1982).
121) Peterman D.J., Misemer D.K., Weaver J.H. and Peterson D.T. : ibid., B 27, 799 (1983).
122) Fujimori A. and Tsuda N. : Solid State Commun., 41, 491 (1982).
123) Sasaki T.A. : J. Surf. Sci. Soc. Jpn., 3, 182 (1982).
124) Weaver J.H., Peterson D.T. and Benbow R.L. : Phys. Rev., B 20, 5301 (1979).
125) Weaver J.H., Peterman D.J., Peterson D.T. and Franciosi A. : ibid., B 23, 1692 (1981).
126) Eastman D.E. : Solid State Commun., 10, 993 (1972).
127) Tapping R.L. : J. Nucl. Mater., 107, 151 (1982).
128) Cotterill P. : "The Hydrogen-Embrittlement of Metals, Progress in Materials Science", Vol.9, p.209, Pergamon Press, Oxford (1961).
129) Scargill D. : J. Nucl. Mater., 74, 62 (1978).
130) Brundle C.R. : J. Vac. Sci. Technol., 11, 212 (1974).
131) Schaumann G., Völkl J. and Alfeld G. : Phys. Status Solidi, 42, 401 (1970).
132) Centelli R., Mazzolai F.M. and Nuovo M. : J. Phys. Chem. Solids, 31, 1811 (1970).
133) Wasilewski R.J. and Kehl G.L. : Metallurgia, 50, 225 (1954).
134) Baba Y. and Sasaki T.A. : JAERI-M 84-005, Japan Atomic Energy Research Institute (1984).
135) Hüfner S., Wertheim G.K. and Buchanan D.N. : Chem. Phys. Lett., 24, 527 (1974).
136) Baba Y. and Sasaki T.A. : JAERI-M 84-071, Japan Atomic Energy Research Institute (1984).
137) Lundin C.E. and Blackledge J.P. : J. Electrochem. Soc., 109, 838 (1962).
138) Wagner C.D. and Biloen P. : Surf. Sci., 35, 82 (1973).
139) Schön G. : J. Electron Spectrosc. Relat. Phenom., 2, 75 (1973).
140) Schön G. : Surf. Sci., 35, 96 (1973).
141) Wagner C.D. : Anal. Chem., 47, 1201 (1975).
142) Wagner C.D. : J. Electron Spectrosc. Relat. Phenom., 10, 305 (1977).
143) Wagner C.D., Gale L.H. and Raymond R.H. : Anal. Chem., 51, 466 (1979).

144) Wagner C.D., Riggs W.N., Davis L.E., Moulder J.F. and Muilenberg G.E. : "Handbook of X-ray Photoelectron Spectroscopy", Perkin-Elmer Corporation, Eden Prairie, Minnesota (1979).
145) Wagner C.D., Passoja D.A., Hillery H.F., Kinsky T.G., Six H.A., Jansen W.T. and Taylor J.A. : J. Vac. Sci. Technol., 21, 933 (1982).
146) Wagner C.D., Zatko D.A. and Raymond R.H. : Anal. Chem., 52, 1445 (1980).
147) Sasaki T.A. and Baba Y. : Phys. Rev., B 31, 791 (1985).
148) Ley L., Kowalczyk S.P., McFeely F.R., Pollak R.A. and Shirley D.A. : Phys. Rev., B 8, 2392 (1973).
149) Weissmann R. and Muller K. : Surf. Sci. Rep., 105, 251 (1981).
150) Larkins F.P. : Atomic Data and Nuclear Data Tables, 20, 311 (1977).
151) Behrisch R. : Nucl. Fusion, 12, 695 (1972).
152) Cecchi J.L. : J. Nucl. Mater., 93/94, 28 (1980).
153) Roth J., Bohdansky J., Poschenrieder W. and Sinha M.K. : ibid., 63, 222 (1976).
154) Bohdansky J., Bay H.L. and Ottenberger W. : ibid., 76/77, 163 (1978).
155) Yamada R., Nakamura K. and Saidoh M. : ibid., 98, 167 (1981).
156) Mohri M., Watanabe K. and Yamashina T. : ibid., 75, 7 (1978).
157) Sone K., Saidoh M., Nakamura K., Yamada R., Murakami Y., Shikama T., Fukutomi M., Kitajima M. and Okada M. : ibid., 98, 270 (1981).
158) Fukuda S., Mohri M. and Yamashina T. : 9th International Vacuum Congress and 5th International Conference on Solid Surfaces, Madrid, 192 (1983).
159) Bohdansky J. and Roth J. : J. Nucl. Mater., 122/123, 1417 (1984).
160) Görlish E., Habel J., Stoch A. and Stoch J. : J. Solid State Chem., 33, 121 (1980).
161) Durrant P.J. and Durrant B. : "Introduction to Advanced Inorganic Chemistry", Williams Clowers and Sons, London (1970).
162) Lea A.C. : Trans. Brit. Ceramic Soc., 40, 98 (1940).
163) Roth J., Bohdansky J. and Ottenberger W. : IPP 9/26, Max Plank Institute für Plasmaphysik Report (1979).
164) for example see, Gmelins Handbuch der Anorganischen Chemie, Verlag Chemie, GMBH, Weinheim, Teil B, No.15 (1959).
165) Toth L.E. : "Transition Metal Carbides and Nitrides", Academic, New York, Vol.7 (1971).
166) Williams W.S. : "Progress in Solid State Chemistry", edited by Reiss H. and McCallan J.D., Pergamon, New York, Vol.6 (1971).
167) Braganza C.M., McCracken G.M. and Erents S.K. : "Plasma-Wall Interactions", Proc. Intern. Symp., Julich, 257 (1976).
168) Mullendore A.W., Whitley J.B. and Mattox D.M. : J. Nucl. Mater., 111/112, 744 (1982).
169) Kaminsky M., Nielson R. and Zschack P. : J. Vac. Sci. Technol., 20, 1304 (1982).
170) Yamada R., Nakamura K. and Saidoh M. : J. Nucl. Mater., 111/112, 744 (1982).
171) Varga P. and Taglauer E. : ibid., 111/112, 744 (1982).
172) Tanaka T., Saiki K., Otani S., Koma A. and Tanaka S. : ibid., 116, 317 (1983).
173) Sukenobu S. and Gomay Y. : J. Vac. Sci. Technol., A 1, 920 (1983).
174) Sukenobu S. and Gomay Y. : J. Nucl. Sci. Technol., 21, 366 (1984).
175) Fukuda S., Mohri M. and Yamashina T. : J. Vac. Sci. Technol., A 2, 50 (1984).
176) Ihara H., Kumashiro Y. and Ito A. : Phys. Rev., B 12, 5465 (1975).
177) Neckel A., Rastl P., Eibler P., Weinberger P. and Schwarz K. : J. Phys., C 9, 579 (1976).
178) Gubanov V.A., Kurmaev E.Z. and Ellis D.E. : ibid., 14, 5567 (1981).
179) Fujimori A., Minami F. and Tsuda N. : Surf. Sci., 121, 199 (1982).
180) Hoshino T. and Tsukada M. : J. Magnetism Magnetic Mater., 31-34, 901 (1983).
181) Neckel A. : Int. J. Quantum Chem., 23, 1317 (1983).
182) Blaha P. and Schwarz K. : ibid., 23, 1535 (1983).
183) Gutsev G.L., Shulga Yu.M. and Borodko Yu.G. : Phys. Stat. Sol., B 121, 595 (1984).
184) Johansson L.I., Callenas A., Stefan P.M., Christensen A.N. and Schwarz K. : Phys. Rev., B 24, 1883 (1981).
185) Haviland D., Yang X., Winzert K., Noffke and Eckard H. : J. Phys., C 18, 2859 (1985).
186) Hagström A.L., Johansson L.I., Johansson B.E. and Hagström S.B.M. : Solid State Commun., 19, 647 (1976).
187) Bradshaw A.M., van de Veen J.F., Himpsel F.J. and Eastman D.E. : ibid., 37, 37 (1980).
188) Johansson L.I., Stefan P.M., Shek M.L. and Christensen A.N. : Phys. Rev., B 22, 1032 (1980).
189) Weaver J.H., Bradshaw A.M., van de Veen J.F., Himpsel F.J., Eastman D.E. and Politis C. : ibid., B 22, 4921 (1980).
190) Oshima C., Aono M., Tanaka T., Kawai S., Zaima S. and Shibata Y. : Surf. Sci., 102, 312 (1981).
191) Hochst H., Bringans R.D., Steiner P. and Wolf Th. : Phys. Rev., B 25, 7183 (1982).

192) Bringans R.D. and Hochst H. : ibid., B 30, 5416 (1984).
193) Porte L., Roux L. and Hanus J. : ibid., B 28, 3214 (1983).
194) Scofield J.H. : J. Electron Spectrosc. Relat. Phenom., 8, 129 (1976).
195) Johansson L.I., Hagström A.L., Jacobson B.E. and Hagström S.B.M. : ibid., 10, 259 (1977).
196) for example see, Gmelines Handbuch der Anorganischen Chemie, Verlag Chemie, GMBH, Weinheim, No.41 (1951).
197) Ho P.S. : Surf. Sci., 72, 253 (1978).
198) Gries W.H. and Rüdenauer F.G. : Int. J. Mass Spectr. Ion Phys., 18, 111 (1975).
199) Sigmund P. : Phys. Rev., 184, 383 (1969).
200) Brice D.K., Doyle B.L., Wampler W.R., Picraux S.T. and Haggmark L.G. : J. Nucl. Mater., 114, 277 (1983).
201) Göpel W., Anderson J.A., Frankel D., Jaehning M., Phillips K., Schäfer J.A. and Rocker G. : Surf. Sci., 139, 333 (1984).
202) for example see, CRC Handbook of Chemistry and Physics, 65th edition, CRC Press, Inc. Boca Raton, Florida, D-50 (1984).